Remote Sensing Tools for Monitoring Grassland Plant Leaf Traits and Biodiversity

Hafiz Ali Imran

Doctoral Thesis

Department of Civil, Environmental and Mechanical Engineering

UNIVERSITY OF TRENTO-ITALY

Session: 2017/2020

UNIVERSITY OF TRENTO-ITALY

Department of Civil, Environmental and Mechanical Engineering

Doctoral School in Civil, Environmental and Mechanical Engineering

Cycle: XXXIII 2017/2020

Doctoral Thesis - February 2022

Remote Sensing Tools for Monitoring Grassland Plant Leaf Traits and Biodiversity

Name: Hafiz Ali Imran

Registration #: 198442

Supervisors

Prof. Dr. Duccio Rocchini - University of Trento/University of Bologna, Italy

Dr. Loris Vescovo - Fondazione Edmund Mach, San Michele all'Adige, Italy

Dr. Damiano Gianelle - Fondazione Edmund Mach, San Michele all'Adige, Italy

Table of Contents

List of figures

Figure 10. Global Sensitivity Analysis of the PROSAIL input parameters. The dimension of the sensitivity refers to the relative contribution (SI) of each input variable and the vertical bars represent the positions of the bands (solid lines, S-2; dotted lines, S-3) used to calculate the investigated SVIs. Input parameter ranges, full names of the variables and units are presented in **Table 3**.

Figure 11. Relationships between VIS-NIR indices and LAI for all eight scenarios for both temporal ((**A**,**E**) 1t; (**B**,**F**) 2t; (**C**,**G**) 3t; and (**D**,**H**) 4t) and spatial scale observations ((**A**,**E**) 1s; (**B**,**F**) 2s; (**C**,**G**) 3s; and (**D**,**H**) 4s). The horizontal dashed line represents the minimum value of LAI when PROSAIL was run using spatial observation LAI ranges as input parameter. In all panels, solid lines represent a linear fit to the data.

Figure 12. Relationships between RE indices and LAI for all eight scenarios for both temporal ((**A**,**E**,**I**) 1t; (**B**,**F**,**J**) 2t; (**C**,**G**,**K**) 3t; and (**D**,**H**,**L**) 4t) and spatial scale observations ((**A**,**E**,**I**) 1s; (**B**,**F**,**J**) 2s; (**C**,**G**,**K**) 3s; and (**D**,**H**,**L**) 4s). The horizontal dashed line represents the minimum value of LAI when PROSAIL was run using spatial observation LAI ranges as input parameter. In all panels, solid lines represent a linear fit to the data.

Figure 13. Relationships between NIR-shoulder indices and LAI for all eight scenarios for both temporal ((**A**,**E**) 1t; (**B**,**F**) 2t; (**C**,**G**) 3t; and (**D**,**H**) 4t) and spatial scale observations ((**A**,**E**) 1s; (**B**,**F**) 2s; (**C**,**G**) 3s; and (**D**,**H**) 4s). The horizontal dashed line represents the minimum value of LAI when PROSAIL was run using spatial observation LAI ranges as input parameter. In all panels, solid lines represent a linear fit to the data.

Figure 14. (**A**) Location of the sample plots in both study areas (IT-PD and IT-MBo). (**B**) The IT-PD plots (n = 9) are located at the experimental farm of the University of Padova (Legnaro, Italy). (**C**) IT-MBo plots (n = 25) are located in the natural grassland ecosystem in the Italian Alps (Monte Bondone, Trento, Italy). RGB images of selected plots of both study sites are shown on the right.

Figure 15. Flowchart representing the data processing approach used in this study. See **Section 2.4** for details on the different levels of processing.

Figure 16. Mean reflectance spectra of nine plots located at the IT-PD site: (**A**) Original reflectance; (**B**) Brightness normalized reflectance; (**C**) Brightness normalized and filtered reflectance; (**D**) Brightness normalized, filtered, and continuum removed spectra; (**E**) Coefficient of variation; (**F**) Standard deviation. In panels (A–F), a solid line represents the mean reflectance obtained from 0.25 × 0.25 m ROIs with a pixel size of 1 mm and a dashed line represents reflectance from 0.25 × 0.25 m ROIs with a pixel size of 1.5 mm.

Figure 17. Mean reflectance spectra of 25 plots located at the IT-MBo site obtained from 0.25 × 0.25 m ROIs: (**A**) Original reflectance; (**B**) Brightness normalized reflectance; (**C**) Brightness normalized and filtered reflectance; (**D**) Brightness normalized, filtered, and continuum removed spectra; (**E**) Coefficient of variation; (**F**) Standard deviation.

Figure 18. Correlation coefficient from the Pearson correlation analysis (R) between optical diversity expressed as CV and SD for each wavelength from 411 to 930 nm and species richness at the IT-PD site: (**A**): 1 mm pixel size; (**B**): 1.5 mm pixel size), considering different processing levels.

Figure 19. Correlation coefficient from the Pearson correlation analysis (R) between optical diversity expressed as CV and SD for each wavelength from 411 to 930 nm and biodiversity indices at the IT-MBo site: (**A**) species richness; (**B**) Shannon's index; (**C**) species evenness index; (**D**) Simpson's index, considering different processing levels.

Figure 20. Correlation coefficient from the Pearson correlation analysis (R) at the IT-PD site between optical diversity expressed as CV and SD for each wavelength from 411 to 930 nm at different spatial scales and species richness.

Figure 21. Correlation coefficient from the Pearson correlation analysis (R) between the optical diversity expressed as CV and SD for each wavelength from 411 to 930 nm at different spatial scales and biodiversity indices at the IT-MBo site: (**A**) species richness; (**B**) Shannon's index; (**C**) species evenness; (**D**) Simpson's index.

Figure 22. Correlation coefficient from the Pearson correlation analysis (R) between optical diversity expressed as CV and SD for each wavelength from 411 to 930 nm and species richness at the IT-PD site considering different numbers of pixels.

Figure 23. Correlation coefficient from the Pearson correlation analysis (R) between optical diversity expressed as CV and SD for each wavelength from 411 to 930 nm and biodiversity indices at the IT-MBo site: (**A**) species richness index; (**B**) Shannon's index; (**C**) species evenness; (**D**) Simpson's index, considering different number of pixels.

Figure 24. Links between spectral diversity, plant traits (PTs) diversity, and biodiversity

Figure 25. (A) Location of the sample plots in study area (IT-MBo). (B) The plots (n = 22) are located in the natural grassland ecosystem in the Italian Alps (Monte Bondone, Trento, Italy).

Figure 26. Species distribution (in %) within each plot.

Figure 27. Box plots of the biochemical (panel A) and biophysical (panel B) plant traits (PTs) standard deviation (SD) among the investigated plots measured from the 10 subsamples of PTs in each plot. The grey box represents the inter-quartile range, with a horizontal line showing the median. Each whisker extends to the highest value that is within 1.5 times the inter-quartile range. The black points indicate outliers values in the PTs measurement (Wickham, 2007). The abbreviations of the x axis labels are: chla (chlorophyll a); chlb (chlorophyll b); bcar (β-carotene); lut (lutein); neox (neoxanthin); violax (violaxanthin); anther (antheraxanthin); C (carbon); H (hydrogen); N (nitrogen); S (sulphur); O (oxygen); SLA (specific leaf area); LWC (leaf water content).

Figure 28. Mantel correlations between the biochemical PTs diversity (measured by Euclidean distance of various PTs) and species β-diversity (measured by Jaccard dissimilarity index).

Figure 29. Mantel correlations between the biophysical PTs diversity (measured by Euclidean distance of biophysical PTs) and species β-diversity (measured by Jaccard dissimilarity index).

Figure 30. Mantel correlations between the spectral diversity (measured by spectral angular mapper of average reflectance of each plot) and species β-diversity (measured by Jaccard dissimilarity index).

Figure 31. R^2 values based on linear regression between the normalized difference of all two-band combinations and LAI for both study sites (IT-MBo 2013 (**A**); IT-MBo 2014 (**B**); and AT-Neu 2018 (**C**)) considering the temporal scale hyperspectral observations. R^2 obtained using: (**A**–**C**) the hyperspectral data. Black circles refer to the position of the indices in the correlogram and arrows are indicating the name of the respective indices.

Figure 32. R^2 values based on linear regression between the normalized difference of all two-band combinations and LAI for IT-MBo 2017 considering the spatial scale observations. White circles refer to the position of the indices in the correlogram and arrows are indicating the name of the respective indices.

Figure S1. RGB images of the different plots at the IT-MBo study site used for spatial analysis.

Figure S2. RGB images of the plot at the AT-Neu study site used for temporal analysis.

Figure S3. The portable system used for spectral measurements at the IT-MBo for spatial scale observations.

Figure S4. RMSE values based on linear regression between the normalized difference of all two-band combinations and LAI for both study sites (IT-MBo 2013 **(a)**; IT-MBo 2014 **(b)**; and AT-Neu 2018 **(c)**) considering the temporal scale hyperspectral observations. RMSE obtained using: **(a–c)** the hyperspectral data; **(d–f)** S-2 simulated bands; **(g–i)** S-3 simulated bands. Black/white circles refer to the position of the indices in the correlogram and arrows are indicating the name of the respective indices.

Figure S5. RMSE values based on linear regression between the normalized difference of all two-band combinations and LAI for IT-MBo 2017 considering the spatial scale observations: **(a)** RMSE obtained using the hyperspectral data; and (b,c) RMSE obtained using S-2 and S-3 simulated bands, respectively. Black circles refer to the position of the indices in the correlogram and arrows are indicating the name of the respective indices.

Figure S6. RGB images of the different plots at the IT-PD and the IT-MBo study sites.

Figure A1. Correlation coefficient from the Pearson correlation analysis (R) between the species richness and optical diversity expressed as CV and SD, averaged across different spectral regions (black lines) and averaged across the spectrum (red lines) computed from the $Level_0$-processed data at the IT-PD site (panel (**A**): 1 mm pixel size; panel (**B**): 1.5 mm pixel size).

Figure A2. Correlation coefficient from the Pearson correlation analysis (R) between the optical diversity expressed as CV and SD, averaged across different spectral regions (black lines) and averaged across the spectrum (red lines) computed from the $Level_0$-processed data at the IT-MBo site (panel A–D: approximately 0.9 mm pixel size) and biodiversity indices: (**A**) species richness; (**B**) Shannon's index; (**C**) species evenness; (**D**) Simpson's index.

Figure B1. Families distribution (in %) within each plot.

Figure B2. Functional groups distribution (in %) within each plot.

List of tables

Table 11. Summary of Mantel correlations for α-diversity at higher taxonomy levels (Shannon's index) vs. biochemical and biophysical variability (measured as standard deviation). In the brackets the p-value is presented.

Table S1. Specifications of the multispectral instrument (MSI) and ocean and land color instrument (OLCI) on the S-2 and S-3 satellite system respectively, The NIR-shoulder bands investigated in this study shown in bold.

Table S2. Summary of the statistics (N: Number of observations; R^2: Coefficient of determination; Adj. R^2: adjusted coefficient of determination; RMSE: Root mean square error) of the second order polynomial regression between leaf area index (LAI, $m^2 \cdot m^{-2}$) estimated from fraction of absorbed photosynthetically active radiation (fAPAR) and the spectral vegetation indices (SVIs) calculated from measured spectra for IT-MBo 2013, IT-MBo 2014, AT-Neu 2018 at temporal scale observations and for IT-MBo 2017 at spatial scale observations. The three best-fitting models are highlighted in bold. Asterisk indicates significance of correlation: $^{***}\ p < 0.001$; $^{**}\ p < 0.01$; $^{*}\ p < 0.05$; n.s.:not significant (Pearson's correlation test).

Table S3. Species richness and composition of each plot investigated at the IT-PD study site.

Table S4. Species richness and composition of each of the 25 plots investigated at the IT-MBo study site.

Table S5. The highest Pearson correlation coefficient (R) and *p*-values (in brackets) for the relationship between species richness and two optical diversity metrics (CV and SD) for different processing levels at the IT-PD study site. The highest R values for each processing level are highlighted in bold.

Table S6. The highest Pearson correlation coefficient (R) and *p*-values (in brackets) for the relationship between biodiversity indices (species richness, Shannon's index, species evenness, and Simpson's index) and the two optical diversity metrics (CV and SD) for different processing levels at the IT-MBo study site. The highest R values for each processing level are highlighted in bold.

Table S7. The highest Pearson correlation coefficient (R) and *p*-values (in brackets) for the relationship between species richness and the two optical diversity metrics (CV and SD) calculated from $Level_3$ processed data at different spatial scales for the IT-PD study site. The highest R values for each spatial scale are highlighted in bold.

Table S8. The highest Pearson correlation coefficient (R) and *p*-values (in brackets) for the relationship between biodiversity indices (species richness, Shannon's index, species evenness, and Simpson's index) and two optical diversity metrics (CV and SD) calculated from $Level_3$ processed data at different spatial scales for the IT-MBo study site. The highest R values for each spatial scale are highlighted in bold.

Table S9. The highest Pearson correlation coefficient (R) and *p*-values (in brackets) for the relationship between species richness and the two optical diversity metrics (CV and SD) calculated from $Level_3$ processed data at different sample size for the IT-PD study site. The highest R values are highlighted in bold.

Table S10. The highest Pearson correlation coefficient (R) and *p*-values (in brackets) for the relationship between biodiversity indices (species richness, Shannon's index, species evenness, and

Simpson's) and the two optical diversity metrics (CV and SD) calculated from $Level_3$ processed data at different sample size for the IT-MBo study site. The highest R values are highlighted in bold.

Table S11. Descriptive statistics (Min: minimum, Max: maximum, SD: standard deviation) of the biochemical plant traits (chlorophyll, β-carotene, and xanthophyll pigments).

Table S12. Descriptive statistics (Min: minimum, Max: maximum, SD: standard deviation) of the biochemical plant traits (carbon, hydrogen, nitrogen, sulphur, and oxygen elements).

Table S13. Descriptive statistics (Min: minimum, Max: maximum, SD: standard deviation) of the biophysical plant traits (specific leaf area and leaf water content).

List of abbreviations

RE	Red-Edge
SVIs	Spectral Vegetation Indices
VIS	Visible
NIR	Near Infrared
LAI	Leaf Area Index
LAD	Leaf Angle Distribution
S-2	Sentinel-2
S-3	Sentinel-3
PTs	Plant Traits
AGB	Aboveground Biomass
SWIR	Shortwave Infrared
GF-5	Gaofen-5
RTMs	Radiative Transfer Models
RENDVI	RE-based Normalized Difference Vegetation Index
NIDI	Normalized Infrared Difference Index
NDIs	Normalized difference indices
EC	Eddy Covariance
SOC	Soil Organic Content
ARTMO	Automated Radiative Transfer Models Operator
GSA	Global Sensitivity Analysis
NWI	Normalized Water Index
MTCI	MERIS Terrestrial chlorophyll index
NSDI	Near-shoulder difference index
RMSE	Root Mean Square Error
R^2	Coefficient of determination
Adj. R^2	Adjusted coefficient of determination
CV	Coefficient of Variation
SD	Standard Deviation
SVH	Spectral Variability Hypothesis
NDVI	Normalized Difference Vegetation Index
CR	Continuum-Removed

nRMSE	Normalized Root Mean Square Error
HPLC	High-performance liquid chromatography
SAM	Spectral Angular Mapper
OTIs	Optical Traits Indicators
TOC	Top-of-Canopy
FLM	Fresh Leaf Mass
LA	Leaf Area
LDM	Leaf Dry Mass
SLA	Specific Leaf Area
LWC	Leaf Water Content

List of publications

The Ph.D. thesis comprised of three research articles:

Publication I: Imran, H. A., Gianelle, D., Rocchini, D., Dalponte, M., Martín, M. P., Sakowska, K., ... & Vescovo, L. (2020). VIS-NIR, red-edge and NIR-shoulder based normalized vegetation indices response to co-varying leaf and Canopy structural traits in heterogeneous grasslands. *Remote Sensing*, *12*(14), 2254.

Publication II: Imran, H. A., Gianelle, D., Scotton, M., Rocchini, D., Dalponte, M., Macolino, S., ... & Vescovo, L. (2021). Potential and Limitations of Grasslands α-Diversity Prediction Using Fine-Scale Hyperspectral Imagery. *Remote Sensing*, *13*(14), 2649.

Publication III: Imran, H. A., Sakowska, K., Gianelle, D., Rocchini, D., Dalponte, M., Scotton, M., & Vescovo, L. (20xx). On the importance of functional diversity links with α and β diversity for the applicability of the optical diversity approach in a subalpine grassland of the Italian Alps. In progress.

Acknowledgment

I am highly grateful to Allah and **Prophet Muhammad** (may Allah peace be upon him) who has granted me courage and strength for successfully completing this thoughtful and laborious work.

First of all, I am extremely grateful to my supervisors, Loris Vescovo, Duccio Rocchini, and Damiano Gianelle, for their invaluable advice, continuous support, and patience during my PhD. Their immense knowledge and plentiful experience have encouraged me in all the time of my academic research and daily life. Thank you for always having the door of your office open for me.

I would also like to thank Karolina Sakowska and again Loris Vescovo for their continuous supporting and motivating me in my research and supporting me whenever I needed it. Without their continuous support, this would not be possible. Thank you for your support not only in research activities but also your support of my early days in Italy. I am honestly thankful for your all gestures since I arrived in Italy. Thank you for always being friendly and always having time for a little break away from work, even when I was feeling low.

Thank you to Michele Dalponte for always helping and supporting me whenever I needed it. I would also like to thank all the group members: Roberto Zampedri, Mauro Cavagna, Lorenzo Frizzera, and Isaac Chini for your support, especially during the field campaigns. Thank you for always being supportive and helping in my research and daily life.

I would like to thank you to María Pilar Martín for hosting me as a guest researcher during my secondment at CSIC, Madrid, Spain. I would like to thank to José Ramón Melendo-Vega who provided his guidance to understand the radiative transfer models. I am very grateful to other colleagues as well for their hospitality and kind gestures during my secondment, I really enjoyed my time in Madrid and enjoyed your company in the office as well as during the field campaigns.

I am very thankful to DEDAGROUP for hosting me as an internee (secondment) and thank you Piergiorgio Cipriano for your guidance and support during my secondment.

I am thankful to all the co-authors who contributed to the studies presented, and the reviewers for their invaluable comments that led to improvements in my publications and therefore in my thesis.

A special thank you to all the friends and colleagues at FEM, UniTN, and members of the Trustee network for accompanying me to share happy and sad moments of life and make me feel at home, even I was far from family. I will always be grateful for the time we have spent together. You all have been part of a very important part of my life. Also, I am thankful to Elisabetta Perini and Riccarda Moser for their support during my stay at FEM.

Finally, I would like to express my gratitude to my parents. Without their tremendous understanding and encouragement throughout my educational career, it would be impossible for me to achieve my goals. I am obviously grateful to my loving wife Sidra Saeed for her motivation and encouragement, especially during my PhD. Thank you for your all-moral supports especially when sometimes I feel low. Of course, She always wanted and wish to see me glittering upon the skies of success.

Funding:

This project has received funding from the European Union's Horizon 2020 Research and Innovation Program under the Marie Skłodowska-Curie Grant No. 721995 (project Trustee).

Abstract

Grasslands are one of the most important ecosystems on Earth, covering approximately one-third of the Earth's surface. Grassland biodiversity is important as many services provided by such ecosystems are crucial for the human economy and well-being. Given the importance of grasslands ecosystems, in recent years research has been carried out on the potential to monitor them with novel remote sensing techniques. Improved detectors technology and novel sensors providing fine-scale hyperspectral imagery have been enabling new methods to monitor plant traits (PTs) and biodiversity.

The aims of the work were to study different approaches to monitor key grassland PTs such as Leaf Area Index (LAI) and biodiversity-related traits. The thesis consists of 3 parts: 1) Evaluating the performance of remote sensing methods to estimate LAI in grassland ecosystems, 2) Estimating plant biodiversity by using the optical diversity approach in grassland ecosystems, and 3) Investigating the relationship between PTs variability with alpha and beta diversity for the applicability of the optical diversity approach in a subalpine grassland of the Italian Alps

To evaluate the performance of remote sensing methods to estimate LAI, temporal and spatial observations of hyperspectral reflectance and LAI were analyzed at a grassland site in Monte Bondone, Italy (IT-MBo). In 2018, ground temporal observations of hyperspectral reflectance and LAI were carried out at a grassland site in Neustift, Austria (AT-NEU). To estimate biodiversity, in 2018 and 2019 a floristics survey was conducted to determine species composition and hyperspectral data were acquired at two grassland sites: IT-MBo and University of Padova's Experimental Farm, Legnaro, Padua, Italy (IT-PD) respectively. Furthermore, in 2018, biochemistry analysis of the biomass samples collected from the grassland site IT-MBo was carried out to determine the foliar biochemical PTs variability.

The results of the thesis demonstrated that the grassland spectral response across different spectral regions (Visible: VIS, red-edge: RE, Near-infrared: NIR) showed to be both site-specific and scale-dependent. In the first part of the thesis, the performance of spectral vegetation indices (SVIs) based on visible, red-edge (RE), and NIR bands alongside SVIs solely based or NIR-shoulder bands (wavelengths 750 - 900 nm) was evaluated. A strong correlation ($R^2 > 0.8$) was observed between grassland LAI and both RE and NIR-shoulder SVIs on a temporal basis, but not on a spatial basis. Using the PROSAIL Radiative Transfer Model (RTM), it was demonstrated that grassland structural heterogeneity strongly affects the ability to retrieve LAI, with high uncertainties due to structural and biochemical PTs co-variation.

In the second part, the applicability of the spectral variability hypothesis (SVH) was questioned and highlighted the challenges to use high-resolution hyperspectral images to estimate biodiversity in complex grassland ecosystems. It was reported that the relationship between biodiversity (Shannon, Richness, Simpson, and Evenness) and optical diversity metrics (Coefficient of variation (CV) and Standard deviation (SD)) is not consistent across plant communities. The results of the second part suggested that biodiversity in terms of species richness could be estimated by optical diversity metrics with an $R^2 = 0.4$ at the IT-PD site where the grassland plots were artificially established and are showing a lower structure and complexity from the natural grassland plant communities. On the other hand, in the natural ecosystems at IT-MBo, it was more difficult to estimate biodiversity indices, probably due to structural and biochemical PTs co-variation. The

effects of canopy non-vegetative elements (flowers and dead material), shadow pixels, and overexposed pixels on the relationship between optical diversity metrics and biodiversity indices were highlighted.

In the third part, we examined the relationship between PTs variability (at both local and community scales, measured by standard deviation and by the Euclidean distances of the biochemical and biophysical PTs respectively) and taxonomic diversity (both α-diversity and β-diversity, measured by Shannon's index and by Jaccard dissimilarity index of the species, families, and functional groups percent cover respectively) in Monte Bondone, Trentino province, Italy. The results of the study showed that the PTs variability metrics at alpha scale were not correlated with α-diversity. However, the results at the community scale (β-diversity) showed that some of the investigated biochemical and biophysical PTs variations metrics were associated with β-diversity. The SVH approach was also tested to estimate β-diversity and we found that spectral diversity calculated by spectral angular mapper (SAM) showed to be a better proxy of biodiversity in the same ecosystem where the spectral diversity failed to estimate alpha diversity, this leading to the conclusion that the link between functional and species diversity may be an indicator of the applicability of optical sampling methods to estimate biodiversity.

The findings of the thesis highlighted that grassland structural heterogeneity strongly affects the ability to retrieve both LAI and biodiversity, with high uncertainties due to structural and biochemical PTs co-variation at complex grassland ecosystems. In this context, the uncertainties of satellite-based products (e.g., LAI) in monitoring grassland canopies characterized by either spatially or temporally varying structure need to be carefully taken into account. The results of the study highlighted that the poor performance of optical diversity proxies in estimating biodiversity in structurally heterogeneous grasslands might be due to the complex relationships between functional diversity and biodiversity, rather than the impossibility to detect functional diversity with spectral proxies.

Keywords: grasslands; optical diversity metrics; plant traits (PTs); leaf area index (LAI); NIR-shoulder indices; radiative transfer models (RTM); spectral diversity hypothesis; biodiversity indices; α-diversity; β-diversity; biochemical and biophysical PTs variability; functional diversity; spectral distances.

Chapter 1

1.1. Introduction

1.1.1 Grassland Ecosystems

Grassland ecosystems are one of the most important ecosystems on earth's terrestrial surface, covering approximately one-third of the Earth's surface (Latham et al., 2014). Grasslands are considered the second largest terrestrial carbon sinks (Anderson, 1991; Derner and Schuman, 2007) and play an important role in agriculture and economy as well as provision of many ecosystem services crucial for the human economy and well-being. Grasslands on the Alps include ecosystems that are located both above and below the timberline (Lüth et al., 2011). While alpine grasslands are located above the timberline and are mainly used as summer pastures (Ellenberg, 2010), mountain grasslands were created and have been maintained as a result of hundreds of years of extensive agricultural activity, and they are among the most species-rich ecosystems outside the tropics. The most important function of grasslands is to provide fodder for domestic grazing animals, biodiversity, support erosion control on steep slopes as well as increase the nutrient absorption capacity and thus improving the water purification service (Philip Robertson *et al*., 2014). However, in the last decades, changes in human activities have modified the landscape in many different regions of the planet. In the Alps, for example, such modifications have accelerated biodiversity loss at unprecedented rates as in the last decades changes in society, tourism, and agricultural production have led to substantial land-use changes and a loss of landscape diversity, particularly for grassland ecosystems (Chemini and Rizzoli, 2014). Due to this continuous decline in landscape diversity and associated loss of biodiversity, the monitoring of grasslands is a need for developing sustainable management and conservation practices. To monitor complex and diverse ecosystems (e.g., Natural grasslands) by conventional field-based methods might not be possible due to high costs, challenges to access to some sampling sites (Marzialetti et al., 2021). In contrast to the field traditional field camping methods, in recent years research has been carried out on the potential to monitor them with novel hyperspectral remote sensing techniques. In recent years, improved detectors technology and novel sensors providing fine-scale hyperspectral imagery are enabling new methods to monitor and estimation of plant traits (PTs) and biodiversity across spatial scales from the leaf level to the canopy, ecosystem, and global scales.

1.1.2. Plant traits

PTs can be defined as morphological, physiological, biochemical, and phonological features (such as e.g., leaf area index (LAI), aboveground biomass (AGB), chlorophyll a and b (cab), carotenoids (car), leaf water content (LWC), Nitrogen (N) etc.) of plants and their organs, which are being commonly adopted in ecological, biogeochemical, and agricultural studies (Homolova et al., 2013; Kattge et al., 201). Such features are measurable at the individual plant or canopy level and can be used in various studies related to ecosystem functioning, community ecology, and assessment of ecosystem services (Homolova et al., 2013; Matheny et al., 2017; Reichstein et al., 2013). With the development of high spatial and spectral resolution imaging spectroradiometer facilitated the quantitative estimation of PTs related to both physiology and biochemistry. In herbaceous plants, LAI is a spatially- and temporally-dynamic key structural PT related to ecosystem functions (e.g., productivity and evapotranspiration), and remote sensing data have been

widely used to capture its variability at various scales. However, the structural and biochemistry variability among leaves, plants, and ecosystems, particularly in natural grasslands, characterized by extreme heterogeneity is strongly affecting the ability to link spectral variation and PTs (Imran et al., 2020). In the last decades, many studies have been carried out, which demonstrated the ability of spectral reflectance to estimate leaf and canopy structural traits with non-destructive methods (Adams and Arkin 1977; Aoki et al., 1986; Blackburn 1998; Curran et al. 1990; Datt, 1998; Gamon and Surfus 1999; Gitelson et al., 2003; Gitelson et al. 1996; Markwell et al. 1995; Peñuelas and Inoue, 1999; Richardson et al. 2002;). To estimate structural and biochemical traits non-destructively canopy structure is one of the main challenges when interpreting the whole canopy reflectance (Knyazikhin et al., 2013) and the impact of vegetation structural heterogeneity on the ability of different optical-based models to retrieve LAI has not been sufficiently described in the literature, and new knowledge is needed to quantify the uncertainties of such models and disentangle the impact of structural and biochemical heterogeneity on LAI estimations.

1.1.3. Biodiversity

Biodiversity refers to the variation of all forms of life at all levels of biological scale, from genes to ecosystems (Wilson, 1988). According to Whittaker, (1960), the biodiversity is distinguished mainly on three scales of species diversity local diversity (α-diversity), species turnover (β-diversity), and the combination of the two diversity metrics leading to an estimate of ecosystem diversity (gamma diversity). To assess biodiversity a large number of indices (Shannon's index (Shannon, 1948), species richness (Colwell, 2009), Simpson's index (Simpson, 1949), Pielou's index (Pielou, 1966), Berger-Parker' index (Berger and Parker, 1970), Mclntosh's index (Mclntosh, 1967), etc. have been developed and used to estimate α-diversity. The α-diversity is commonly measured by species richness (number of species in the sampling area) or can be quantified with other heterogeneity measures, such as e.g., Shannon's index, Simpson's index, and species evenness (calculated as Pielou's index), which measure the even abundance between species and dominance of the species.

β-diversity (species turnover) is usually assessed by using the information about the species compositional distance among sampling plots and measured as pairwise dissimilarity between the site pairs and the resulting matrix called the dissimilarity index (Gholizadeh et al., 2020). To assess the β-diversity several indices have been developed, for example, Jaccard index (Jaccard, 1912), Bray–Curtis index (Bray and Curtis, 1957), Sørensen index (Sørensen, 1948), Wilson and Shmida index (Wilson and Shmida, 1984), Colwell and Coddington index (Colwell and Coddington, 1994), and Lennon index (Lennon et al., 2001). Jaccard and Bray-Curtis are commonly used to measure the species turnover in population and community ecology (Baselga, 2013). Jaccard dissimilarity index is calculated using plant occurrence (presence/absence data), and it quantifies the pairwise dissimilarity between the vegetation in sampling units as the ratio between the common number of species and the unique number of species in each plot. The value of index ranges from 0 to 1 and 0 indicates total inequality among plots, while the value 1 indicates total equality is identified (Marzialetti et al., 2021). While the Bray–Curtis dissimilarity index is calculated using quantitative species cover data, and it is defined as a ratio between the difference of abundance values and the sum of abundance values for each species. The value of the index ranges from 0 to 1 and 0 refers to when the sampling units are completely different and value 1 indicates that the species composition of the two plots is identical (Marzialetti et al., 2021). Monitoring plant diversity in relatively large

areas has always been considered a challenging task because it requires extensive field surveys, which are limited in their ability to sample over large regions. In recent years, improved remote sensing technology and novel sensors providing fine-scale hyperspectral imagery have enabled new methods to monitor ecosystem biodiversity based on varying plant optical properties of different species or functional groups (Gamon et al., 2020; Ustin et al., 2020). This provides a powerful opportunity for ecologists to investigate the links between optical diversity and plant diversity across spatial scales from the leaf level to the canopy, ecosystem, and global scales (Rocchini et al., 2016).

1.1.4. Remote sensing

Remote sensing can provide fundamental spatial and temporal information and can be efficiently used in monitoring plant traits related to plant biochemistry, photosynthetic processes, and canopy structure. Such plant and canopy information can be obtained on both qualitative and quantitative basis, and during the last years, innovative remote sensing tools have been introduced to fill the measurements gaps at scales from centimeters to a few meters, to provide a more fundamental understanding of the complex processes which link vegetation characteristics and spectral responses at increasing pixel sizes (Homolova et al., 2013). The interaction between incoming solar radiation and the canopy elements are very complex and are based on three fundamental physical mechanisms: absorption, reflection, and transmittance. The variation in the visible (400 – 700 nm, VIS) part of the spectrum is mainly due to the variation in the leaf pigment and the nutrient content, while variation in the near-infrared (700 – 1300 nm, NIR) spectral region is due to leaf structure and the leaf water content (Aneece and Epstein 2015). The mechanisms behind the variation in the leaf spectra are well understood (Kumar et al., 2002), but the interpretation of the canopy level reflectance remains challenging due to multiple light interactions between canopy elements and background (Disney et al., 2006; Ross, 1981; Widlowski et al., 2004). The reflectance signal is not only affected by the leaf biochemical variations, but the spectral signal is also influenced by different photosynthetic (shaded and sunlit leaves) and not-photosynthetic elements (flowers, dead material) of the canopy. Further, the canopy level reflectance is also influencing due to the other leaf traits (e.g., ratio of the mesophyll cell surface to intercellular air spaces, leaf thickness) and canopy structural properties (e.g., leaves orientation in a canopy characterized by leaf angle distribution, leaves aggregation characterized by clumping index). Canopy structural organization describes the three-dimensional geometric distribution of the aboveground photosynthetic and non-photosynthetic vegetation components (Martens et al., 1991). Canopy structure is one of the main challenges when interpreting the whole canopy reflectance and novel approaches have been suggested to decouple structural and biochemical traits (Homolova et al., 2013; Knyazikhin et al., 2013) and to determine canopy structure and ecosystem function with greenness-independent methods (Delegido et al., 2015; Ollinger, 2011; Vescovo et al., 2012). For the estimation of PTs, mainly two approaches have been adopted: i) empirical relationships between variables and optical data or spectral vegetation indices (SVIs), and ii) inversion of canopy radiative transfer models (RTMs, Fang et al., 2003; Li et al., 2014; Meroni et al., 2004; Schlerf and Atzberger, 2006).

1.1.5. The empirical approach to estimate PTs

The empirical approach is based on the statistical relationship between PTs and spectral data and is used to quantify the strength of the relationship. SVIs are mathematical combinations of vegetation surface reflectance at two or more wavelengths (Jackson and Huete, 1991) and due to their ease of computation, SVIs-based empirical models are more widely used (Vińa et al., 2011). Over the last decades, the SVIs-based methods traditionally used combinations between VIS and NIR bands to estimate LAI. However, several authors demonstrated that SVIs (Figure 1) based on the NIR and red-edge (RE) spectral domains (from 690 to 740 nm; Curran et al., 1990) can significantly improve LAI estimations (Delegido et al., 2013; Kira et a., 2017; Nguy-Robertson et al., 2014). The RE spectral domain is located between the red and the NIR wavelengths (Figure 1), in a portion of the spectrum where reflectance strongly increases, being on the borderline between chlorophyll absorption (in the red wavelengths) and leaf and canopy scattering in the NIR wavelengths. Concurring variations in both the chlorophyll content and the leaf structure can be detected in this domain. Frampton et al. (2013) and Clevers et al. (2013, 2017) analyzed the performance of red-edge chlorophyll-related indices in estimating canopy traits. Band combinations investigated by these authors included at least one band < 740 nm, in an area of the spectrum which is still sensitive to chlorophyll absorption. On another hand, indices calculated with NIR band combinations (>740 nm) are expected to be mainly influenced, with greenness-independent mechanisms, by canopy structure (as demonstrated by Delegido et al., 2015) and not directly by chlorophyll content as suggested by Peng et al., (2017). The SVIs nomenclature regarding the RE and NIR spectral region is often not consistent, in some studies, S-2 bands 5, 6, and 7 (respectively, at 705, 740, and 783 nm) are considered to be part of the RE region (Cogato et al., 2019; Delegido et al., 2015) although band 7 is well beyond the threshold between RE and NIR and is in the NIR-shoulder region (750–900 nm, Filella et al., 1994; Horler et al., 1983; Xie et al., 2018). The definition of two bands RE and normalized difference indices used in this study is presented in Section 2.2.4.

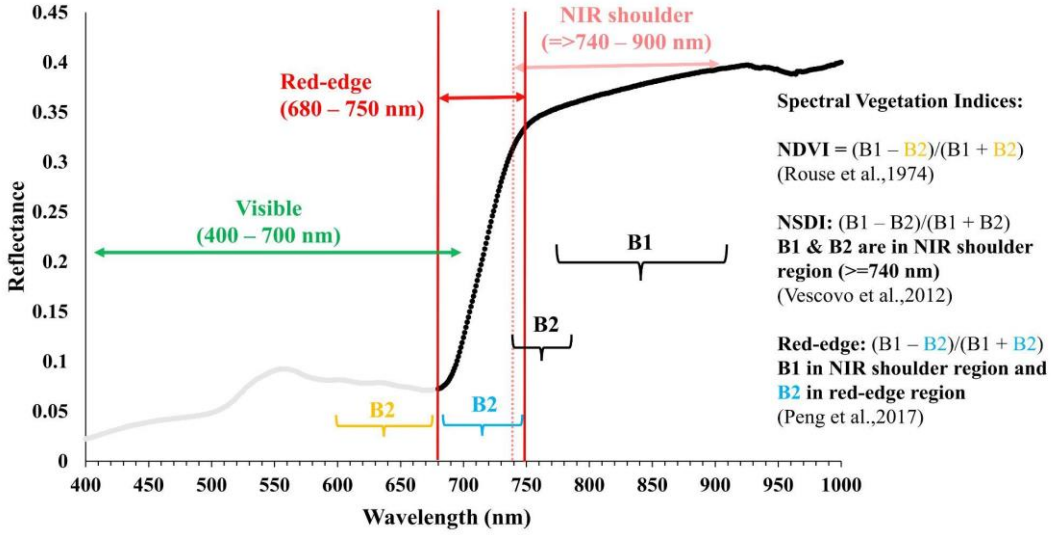

Figure 1. Vegetation spectrum and sentinel-2 bands in different parts of the spectrum (visible, red-edge, and Near-infrared shoulder) are highlighted. The formulas of the normalized difference spectral vegetation indices (SVIs) are added which are calculated using the highlighted bands.

1.1.6. Physical-based radiative transfer models

The Radiative Transfer Models (RTMs) based on physical principles are capable of simulating the interaction of light with vegetation at leaf and canopy levels and provide an explicit method for estimating the vegetation biophysical variables from canopy reflectance (Atzberger et al., 2013; Darvishzadeh et al., 2019; Houborg et al., 2007). To simulate the canopy reflectance RTM (e.g., PROSAIL) has been used in forward mode using different input parameters (Input parameter used in this study described in Table 3 in Section 2.2.6). The RTM models when used in forward mode when the aim is to examine the sensitivity of canopy reflectance to different factors, for instance, the effect of parameters on the RE and NIR slopes (Berger et al., 2018). Another approach to retrieve LAI is based on the inversion of RTM which simulates the interactions of radiation with vegetation elements and the soil (Atzberger et al., 2015). Such inversion approaches are demonstrated to be challenging when the model is not well-suited for the complex vegetation type (Atzberger et al., 2015) and when suitable ancillary data and regularization methods to optimize the inversions for an efficient parameterization are lacking (Verrelst et al., 2019). However, in some cases when in-situ data is impaired for example the large-scale regional and global studies, inversion of physical models is preferably used to estimate PTs. Regardless of the methods (statistical and RTM-based approaches) to estimate PTs, the selection of leaf structural and canopy architectural settings is key to achieve an accurate LAI retrieval and can be challenging when complex plant canopies are modeled (Van der Tol et al., 2020; Darvishzadeh et al., 2008a).

1.1.7. Spectral diversity hypothesis

The complex canopy structure can affect the patterns of when incoming solar radiation encounters in the canopy, capturing these complex patterns is quite challenging until a clear understanding of the interdependencies of PTs and canopy structure (Ollinger, 2011). Canopy structure is one of the main challenges when interpreting the whole canopy reflectance, canopy structural organization describes the three-dimensional geometric distribution of the aboveground photosynthetic and non-photosynthetic vegetation components (Martens et al., 1991). The measurements from the optical sensors are the result of the complex physical interaction between incoming solar radiation and canopy surfaces at different spectra regions that encodes essential information on vegetation states, function, and structure and is called “spectral signature” (Ma et al., 2020). The reflectance from the visible (VIS) to near-infrared (NIR) spectral region is related to the biophysical and biochemical properties of leaves and canopy structure (Homolova et al., 2013; Ma et al., 2020). The spectral variation (also called optical diversity) is “variation in remote sensing measurements, typically spectral reflectance, across sets of pixels and has been proposed to relate to conventional metrics of biodiversity” (Wang et al., 2018a; Rocchini et al., 2010). Each plant species has unique biochemical, structural, and functional properties which, at the canopy level, determine optical diversity (Heumann et al., 2015, Rocchini et al., 2004). Plant species are characterized by species-specific biochemical, structural, and functional properties which determine spectral diversity in the visible and NIR. Many studies (Ustin and Gamon, 2010; Clark et al., 2012; Wang et al., 2016) indicated the potential of high-resolution tools to analyze across-scale complex dynamics regulating ecosystem diversity and function. Using very high spatial and spectral resolution imagery spectrometers, it is possible to capture spectral information of single leaf or single individuals. When observations are carried out at the canopy level, imagery spectrometers data provide information to detect the spatial variation of ecosystem properties, and thus to characterize

ecosystem diversity patterns related to biochemistry, structure, and species populations. Using image spectrometers, spectral heterogeneity can be used as an indicator of relative diversity which incorporates species richness, biochemical properties, and canopy structure (Rocchini et al., 2010). Several studies (Gholizadeh et al., 2019; Sakowska et al., 2019; Wang et al., 2018a; Wang et al., 2018b; Wang et al., 2016) recently adopted a statistical approach to assess vegetation spectral variability and proposed an objective method to relate hyperspectral remote sensing (RS) and plant diversity. These authors demonstrated the correlation between ecosystem diversity (expressed with conventional biodiversity indices such as Shannon's index, species richness, species evenness, and Simpson's index) and "optical diversity", an optically-derived metric of biodiversity based on the coefficient of variation (CV) in spectral reflectance across space. The average coefficient of variation in spectral reflectance across space (CV) can be calculated as follows:

$$\mathrm{CV}_{\mathrm{image}} = \frac{\sum_{\lambda=411}^{930} \left(\frac{\mathrm{std}\,(\rho_\lambda)}{\mathrm{mean}\,(\rho_\lambda)} \right)}{\text{number of bands}} \quad (1)$$

where ρ_λ represents the reflectance value at wavelength λ and std (ρ_λ) and mean (ρ_λ) indicate the standard deviation and mean value of the reflectance at wavelength λ, respectively.

To access the species turnover diversity (β-diversity) among vegetation plots, many authors (Gholizadeh et al., 2020; Marzialetti et al., 2021; Rocchini et al., 2016) used the pairwise dissimilarity methods (i.e., dissimilarity between site pairs) and then analyzed the relationship between floristics β-diversity (Jaccard dissimilarities index, Bray–Curtis dissimilarities index) and Euclidean distances or other methods (i.e. spectral angular mapper - SAM, Kruse et al. (1993)) calculated from the spectral data. The SAM is actually the spectral classification which is measured by the angle between two spectral profiles and the spectra account as vectors. Similar spectra have low SAM values and high spectral diversity have high SAM values.

$$SAM = \cos^{-1}\left(\frac{\sum_{i=1}^{sb} t_i r_i}{\sqrt{\sum_{i=1}^{sb} t_i^2}\sqrt{\sum_{i=1}^{sb} r_i^2}}\right) \quad (2)$$

sb is the number of bands in Speclib. t_i and r_i are the reflectance of target and reference spectrum in band i, respectively.

1.1.8. Biochemical and biophysical plant traits variability

Plant species are characterized by species-specific biochemical, structural, and functional properties which determine spectral diversity in the visible and NIR. Each plant species has unique biochemical, structural, and functional properties which, at the canopy level, determine optical diversity. Many studies (Ustin and Gamon, 2010; Clark and Roberts, 2012; Wang et al., 2016) indicated the potential of high-resolution optical tools to analyze across-scale complex dynamics regulating ecosystem diversity and function. Using very high spatial and spectral resolution imagery spectrometers, it is possible to capture spectral information of single leaf or single individuals. When observations are carried out at the canopy level, imagery spectrometers data provide information to detect the spatial variation of ecosystem properties, and thus to characterize

ecosystem diversity patterns related to biochemistry, structure, and species populations. Using image spectrometers, spectral heterogeneity can be used as an indicator of relative diversity which incorporates species richness, biochemical properties, and canopy structure (Rocchini et al., 2010). Wang and Gamon (2019) highlighted the advantage of the PTs diversity approach to link with biodiversity as it focuses on capturing the range and variation in traits that can be linked with the diversity of species without identifying every single species in the sampling unit. Schweiger et al, (2017) used statistical methods like partial least squares regression (PLSR) to predict the plant functional types by linking the plant functional traits and the canopy spectral response and reported that biochemical and structural traits can be used as a proxy of plant functional diversity. In another study Asner and Martin, (2009) highlighted the importance of nutrient variation in tropical forest canopies and emphasized that biochemical diversity is tightly linked to species diversity. In this context, understanding biochemical diversity is crucial to understand the ecosystem's functional diversity. In recent years, improved remote sensing technology and novel sensors provide an opportunity to measure the reflectance in hundreds of narrow spectral bands, from which the spectral feature is associated with plant biochemical and biophysical PTs which further can be linked with plant diversity (Asner and Martin, 2009; Petchey and Gaston, 2006 Torresani et al., 2021). Until recent remote sensing applications focused on the relationships between spectral diversity and plant diversity; however, the link between foliar biochemical diversity and taxonomic diversity remains to be established (Schweiger et al., 2017).

1.2. Study aims

Given the importance of grasslands as they regulate many ecosystem services (for example, fodder for domestic grazing animals, biodiversity, maintenance of the soil fertility etc.) and the current decline in biodiversity, novel and efficient methods are required to monitor grassland ecosystems across spatial scales from the leaf level to the canopy, ecosystem, and global scales. The aim of the PhD was to explore the potential of different proximal sensing data for monitoring key grassland PTs such as Leaf Area Index (LAI) and biodiversity-related metrics (α-diversity and β-diversity). The thesis consists of three parts: 1) Evaluate the performance of remote sensing methods to estimate LAI in grassland ecosystems (publication 1), 2) Estimate species diversity by using optical diversity approach in grassland ecosystems (publication 2), and 3) Investigate the relationship between PTs variability with α and β diversity for the applicability of the optical diversity approach in a subalpine grassland of the Italian Alps (publication 3).

In the first part of the study, evaluating the performance of remote sensing methods to estimate LAI, temporal and spatial observations of hyperspectral reflectance and LAI were analyzed at two different grassland sites (contrasting structure) of the Italian and Austrian Alps (Monte Bondone, Italy - IT-MBo, and Neustift, Austria - NEU-AT), situated on the subalpine and montane vegetation belts respectively. Further, in order to study the impact of grassland structural and biochemical heterogeneity on LAI estimations by analyzing the spectral reflectance response to co-varying biochemical and structural leaf and canopy traits across the VIS-NIR spectral domain using an RTM approach.

In the second part, the focus was to use the spectral diversity hypothesis (SVH) approach to estimate plant diversity in artificially established plant communities (IT-PD) and in a semi-natural subalpine grassland ecosystem (IT-MBo). The effect of image post-processing techniques to fully

disentangle the optical diversity due to plant diversity from the optical diversity due to illumination artifacts, or due to the presence of pixels of non-photosynthetic material, such as dead material or flowers were also highlighted.

Finally, the third part investigated the relationship between PTs variability (which is an indicator of functional diversity and can be measured by standard deviation of the biochemical and biophysical PTs) and α-diversity (measured by Shannon's index) at different taxonomic ranks (species, families, and functional groups). The relationship between the PTs variability (measured by the Euclidean distances of the biochemical and biophysical PTs) and the β-diversity (measured by Jaccard dissimilarity index of the species, families, and functional groups percent cover) was also investigated. Finally, analyze the performance of spectral diversity proxies to estimate β-diversity using the measured pairwise distances.

More detailed information on the specific objectives of the individual publications can be found in the full text attached to the thesis.

1.3. Thesis outline

This PhD dissertation is structured as a collection of scientific papers which I published during my doctoral research. In the thesis document, each chapter is based on an article with its own introduction, material and methods, results, discussion, and conclusion. The PhD research project was mainly conducted by using the data collected from 3 different sites: Monte Bondone, Trentino, Italy (IT-MBo, Italy), Neustift, Tyrol, Austria (AT-Neu), and experimental farm of the University of Padova, Legnaro, Padua, Italy (IT-PD) and the information about each study site added in the respective articles.

In chapter 2, I present the different SVIs responses to co-varying the leaf and structural PTs in the heterogeneous grassland ecosystems (IT-MBo and AT-Neu). The potential of different SVIs based on different spectral regions (VIS, RE, and NIR-shoulder) was evaluated at temporal and spatial scales. The results highlighted the impact of grassland structural and biochemical heterogeneity on LAI estimations. The impact of grassland structural and biochemical heterogeneity on LAI estimations was demonstrated to be strong and no reliable field LAI estimation was possible at the spatial scale with any investigated SVI. The results of the empirical approach were compared with the physical-based RTM model and highlighted how the co-varying PTs affect the performance of SVIs to estimate LAI. Despite the use of SVIs methods to estimate PTs is very common but this approach is not straightforward especially when spatially heterogeneous canopy are focused. The reflectance measurement from structurally heterogeneous (high diversity) vegetation canopies are more complex compared to the homogenous canopies (low diversity). This leads to the spectral variability hypothesis (SVH): as the number of plant species increases for a given area, the spectral diversity observed from that area should also increase. In chapter 3 examine the SVH approach was adopted to check the potential of using high-resolution hyperspectral images to estimate α plant diversity in grassland ecosystems (IT-PD; artificially established grassland plots with species-poor mixture and IT-MBo; species-rich semi-natural grasslands). The result of the study highlighted the challenges to use high-resolution hyperspectral images to estimate plant diversity in complex grassland ecosystems. It was reported that the relationship between biodiversity (Shannon's index, species richness, species evenness, and Simpson's index) and optical

diversity metrics (Coefficient of variation (CV) and Standard deviation (SD)) is not consistent across plant communities. Despite the fact that we used several different processing techniques to enhance the optical diversity signal, for the subalpine grassland site of IT-MBo, we were not able to match the performance of optical-based methods to estimate the biodiversity reported in other studies. However, some evidence was reported predicting plant diversity when optical diversity metrics were calculated from post-processed hyperspectral images. The visible part of the spectrum (in particular the red domain), characterized by a strong absorbance, showed to be one of the key spectral areas for biodiversity detection. In chapter 4, I used the biochemical and biophysical PTs variability metrics to link with the taxonomic diversity at both α and β diversity scales and we observed that due to the complex nature of the plant communities in the investigated ecosystem we are not able to relate the PTs variability with taxonomic α-diversity. Conversely, we observed a moderate correlation reported between taxonomic β-diversity and Euclidean distances of the biochemical and PTs. Further, in this part, I also tested the correlation between spectral diversity measured as spectral angular mapper of the average reflectance from each plot and taxonomic β-diversity and the results gave evidence of estimating β-diversity with spectral diversity approach.

In chapter 5, concludes this thesis with the discussion and conclusions of the results of previous chapters. This chapter includes the main findings of this thesis and recommendations for future work are provided.

Chapter 2

VIS-NIR, Red-Edge and NIR-Shoulder Based Normalized Vegetation Indices Response to Co-Varying Leaf and Canopy Structural Traits in Heterogeneous Grasslands

Hafiz Ali Imran [1,2,*], Damiano Gianelle [1], Duccio Rocchini [3,4], Michele Dalponte [1], M. Pilar Martín [5], Karolina Sakowska [6,7,8], Georg Wohlfahrt [6] and Loris Vescovo [1]

[1] Sustainable Ecosystems and Bioresources Department, Research and Innovation Centre, Fondazione Edmund Mach, Via E. Mach 1, 38010 San Michele all'Adige (TN), Italy; damiano.gianelle@fmach.it (D.G.); michele.dalponte@fmach.it (M.D.); loris.vescovo@fmach.it (L.V.)

[2] Department of Civil, Environmental and Mechanical Engineering, University of Trento, Via Mesiano 77, 38123 Trento (TN), Italy

[3] Alma Mater Studiorum University of Bologna, Department of Biological, Geological and Environmental Sciences, Via Irnerio 42, 40126 Bologna, Italy; duccio.rocchini@unibo.it

[4] Czech University of Life Sciences Prague, Faculty of Environmental Sciences, Department of Applied Geoinformatics and Spatial Planning, Kamýcka 129, 16500 Prague-Suchdol, Czech Republic

[5] Environmental remote sensing and spectroscopy laboratory (SpecLab), Spanish National Research Council (CSIC), Albasanz 26-28, 28037 Madrid, Spain; mpilar.martin@cchs.csic.es

[6] Department of Ecology, University of Innsbruck, Sternwartestrasse 15, 6020 Innsbruck, Austria; karolina.sakowska@ibe.cnr.it (K.S.); Georg.Wohlfahrt@uibk.ac.at (G.W.)

[7] Institute of BioEconomy, National Research Council (IBE-CNR), Via Biasi 75, 38010 San Michele all'Adige (TN), Italy 8 Foxlab Joint CNR-FEM Initiative, Via E. Mach 1, 38010 San Michele all'Adige (TN), Italy

* Correspondence: hafiz.imran@fmach.it; Tel.: +39-389-8921-946

Received: 14 May 2020; Accepted: 9 July 2020; Published: 14 July 2020

Abstract

Red-edge (RE) spectral vegetation indices (SVIs)—combining bands on the sharp change region between near-infrared (NIR) and visible (VIS) bands—alongside with SVIs solely based on NIR-shoulder bands (wavelengths 750–900 nm) have been shown to perform well in estimating leaf area index (LAI) from proximal and remote sensors. In this work, we used RE and NIR-shoulder SVIs to assess the full potential of bands provided by Sentinel-2 (S-2) and Sentinel-3 (S-3) sensors at both temporal and spatial scales for grassland LAI estimations. Ground temporal and spatial observations of hyperspectral reflectance and LAI were carried out at two grassland sites (Monte Bondone, Italy, and Neustift, Austria). A strong correlation ($R^2 > 0.8$) was observed between grassland LAI and both RE and NIR-shoulder SVIs on a temporal basis, but not on a spatial basis. Using the PROSAIL Radiative Transfer Model (RTM), we demonstrated that grassland structural heterogeneity strongly affects the ability to retrieve LAI, with high uncertainties due to structural and biochemical PTs co-variation. The $RENDVI_{783.740}$ SVI was the least affected by traits co-variation, and more studies are needed to confirm its potential for heterogeneous grasslands leaf area index (LAI) monitoring using S-2, S-3, or Gaofen-5 (GF-5) and PRISMA bands.

Keywords: leaf area index; grassland; NIR-shoulder indices; Sentinel-2 and Sentinel-3 bands; radiative transfer models

2.1. Introduction

Canopy structural organization describes the three-dimensional geometric distribution of the aboveground photosynthetic and non-photosynthetic vegetation components (Martens et al., 1991).

Canopy structure is described by plant traits (PTs) such as leaf area index (LAI), aboveground biomass (AGB), and other canopy and leaf structural traits such as leaf angle distribution (LAD), gap fraction, leaf clumping, the proportion of photosynthetic and non-photosynthetic elements (Gianelle & Vescovo, 2007; Müller-Linow et al., 2015; Serrano et al., 2000) specific leaf area (SLA) and leaf dry matter, which can influence absorption and scattering light dynamics (Ollinger, 2011; Roelofsen et al., 2014).

Remote sensing can provide fundamental spatial and temporal information, which can be used in monitoring PTs related to plant biochemistry, photosynthetic processes and canopy structure. During the last years, the proximal sensing approach was used to fill the scaling gap between leaf and satellite measurements, linking vegetation characteristics and spectral responses from the leaf level to increasing pixel sizes (Homolová et al., 2013; Sakowska et al., 2019; Wang et al., 2018a). While the visible (VIS) and shortwave infrared (SWIR, 1100–2500 nm) parts of the reflectance spectrum are mainly determined by pigments and water content absorption, respectively, in the near-infrared (NIR, 750–1400), reflectance is high compared to the VIS domain because individual leaves and whole plant canopies strongly scatter NIR, and the degree of NIR scattering is driven by the internal leaf structure alongside with canopy structure and the ratio between green and non-photosynthetic components (Ollinger, 2011).

In herbaceous plants, LAI is a spatially- and temporally-dynamic key trait related to ecosystem functions (e.g., productivity and evapotranspiration), and remote sensing data have been widely used to capture its variability at various scales (Kumar & Mutanga, 2017; Vescovo & Gianelle, 2008). However, the structural and biochemistry variability among leaves, plants, and ecosystems—particularly in natural grasslands, characterized by extreme heterogeneity (Sakowska et al., 2019)—is strongly affecting our ability to link spectral variation and LAI. Simultaneously with LAI, factors such as leaf anatomy and LAD are also varying in space and time (e.g., across heterogeneous canopies or due to phenological changes), and this has a significant and often unpredictable impact on scattering across the spectrum. When more structural traits co-vary, LAI estimation based on spectral data may be challenging (Ollinger, 2011), as reflectance is sensitive to multiple leaf and canopy traits and disentangling LAI from structural and biochemical drivers is difficult (Zarco-Tejada et al., 2018). The impact of vegetation structural heterogeneity on the ability of different optical-based models to retrieve LAI has not been sufficiently described in the literature, and new knowledge is needed to quantify the uncertainties of such models and disentangle the impact of structural and biochemical heterogeneity on LAI estimations.

One of the main remote sensing approaches to estimate PTs focuses on empirical models, which are used to quantify relationships between PTs and canopy reflectance or spectral vegetation indices (SVIs) (Kira et al., 2017; Li et al., 2014). Over the last decades, the SVIs-based methods traditionally used combinations between NIR and VIS bands (Fava et al., 2009; Hansen & Schjoerring, 2003; Rouse et al., 1974) to estimate LAI. However, several authors demonstrated that SVIs based on the NIR, and red-edge (RE) spectral domains can significantly improve LAI estimations (Delegido et al., 2013; Kira et al., 2017; Nguy-Robertson et al., 2014). The RE is defined as the spectral region between 680 and 750 nm where a sharp change in the vegetation reflectance can be observed (Filella & Peñuelas, 1994; Horler et al., 1983; Xie et al., 2018). Such spectral domain is on the transition between chlorophyll absorption in the red wavelengths and leaf/canopy scattering in the NIR wavelengths (Frampton et al., 2013; Horler et al., 1983). The use

of narrow-band SVIs is becoming extremely important in the context of the recently launched satellite missions such as Sentinel-2 (S-2) and Sentinel-3 (S-3), as well as within the context of new hyperspectral missions such as Gaofen-5 (GF-5) and PRISMA.

The Radiative Transfer Models (RTMs) based on physical principles (Houborg, 2007) can simulate the interaction of light with vegetation at leaf and canopy levels and provide an explicit method for estimating the vegetation biophysical variables from canopy reflectance (Atzberger et al., 2013). Another approach to retrieve LAI is based on the inversion of RTM which simulate the interactions of radiation with vegetation elements and the soil (Atzberger et al., 2015). Such inversion approaches are demonstrated to be challenging when the model is not well-suited for the observed vegetation type (Atzberger et al., 2015) and when suitable ancillary data and regularization methods to optimize the inversions for an efficient parameterization are lacking (Verrelst et al., 2019). In addition, RTMs are mainly focused on chlorophyll and not on other pigments such as brown pigment content (polyphenols; Cbrown) which play an important role in shaping the spectral response of grasslands at varying phenological stages. This trait is rather poorly analyzed in the literature and the RTM parameter itself lacks a proper physically meaning, and it is thus not measurable with field observations (Danner et al., 2019).

2.1.1. Red-Edge and NIR-Shoulder SVIs

Considering the aforementioned RTM limitations and the fact that the new satellite missions are providing several bands across the RE and the NIR shoulder regions, further research is expected on the ability of SVIs based on such regions to retrieve LAI and on the spectral response mechanisms at the canopy level in different vegetation types (Rossi et al., 2019), which are not yet fully explored (Pettai et al., 2005; Zhen & van Iersel, 2017). RE SVIs (which make use of the RE spectral region) include the RE-based normalized difference vegetation index (RENDVI, Gitelson & Merzlyak, 1994) and the chlorophyll index (CIre, Gitelson et al., 2003). These SVIs were found to be very effective in estimating not only canopy chlorophyll content but also LAI (Delegido et al., 2013; Sakowska et al., 2015; Shang et al., 2015).

In recent years, a number of studies have used SVIs combining bands starting from around 750 nm and beyond (750–770 nm) with the NIR bands ("NIR-shoulder SVIs") for the estimation of LAI and phytomass (Liu et al., 2014; Vescovo et al., 2012). Vescovo et al. (2012) analyzed the performance of normalized infrared difference index (NIDI), calculated using simulated Chris Proba H25 and H18 bands, to estimate phytomass. H25, centered at 872 nm, is a NIR band, while the band H18, centered at 748 nm, lies on the borderline between the RE and the NIR shoulder (750 nm). The NIDI index (Vescovo et al., 2012) has been shown to perform well in determining phytomass even for a Mediterranean grassland characterized by a significant presence of brown canopy elements, which suggested a possible chlorophyll-independent nature of the phytomass-index relationship due to wavelength-dependent scattering dynamics. NIR-shoulder SVIs were also used by Liu et al. (2014), who demonstrated how the simple ratio of reflectance at 780 and 890 nm can be used for assessing leaf structure features, confirming the ability of NIR-based SVIs to detect the effect of leaf deterioration and senescence.

The SVIs nomenclature regarding the RE and NIR spectral region, unfortunately, is often not consistent. S-2 bands 5, 6, and 7 (respectively, at 705, 740, and 783 nm) are considered to be part of the RE region (Cogato et al., 2019; Delegido et al., 2011) although band 7 is well beyond the

threshold between RE and NIR and is in the NIR-shoulder region (750–900 nm (Filella & Peñuelas, 1994; Horler et al., 1983; Xie et al., 2018). In addition, a few authors (Fernández-Manso et al., 2016; Peng et al., 2017; Sakowska et al., 2019) using normalized difference indices (NDIs) based on S-2 bands 7 and 8 (or 8a) refer to such SVIs as RENDVI indices, although they only make use of NIR-shoulder bands. The definition of two bands NDIs used in this study is presented in Section 2.2.4.

2.1.2. SVIs and LAI Empirical Models: Does Trait-Covariation Matter?

SVIs combining NIR and RE bands have been used in the last years to estimate both structural and biochemistry-related traits. The impact of structural traits on reflectance in RE spectral regions and on RE SVIs, however, is arousing controversy. According to some authors, RE SVIs are able to reduce structure-related artifacts in retrieved biochemical-related traits, as the RE is thought to be sensitive to chlorophyll content and largely unaffected by structural properties (Zarco-Tejada et al., 2018). More recently, Peng et al. (2017) showed that SVIs based on NIR band and RE band of 740 nm (RE740) demonstrated to be good predictors of canopy chlorophyll in crop types with contrasting canopy structure. The authors concluded that using NIR and RE740 band combinations provided good chlorophyll estimation due to the "reduced sensitivity of the RE to hysteresis driven by different canopy and leaf structures". Conversely, many authors agree on the fact that both biochemistry and structure contribute in determining the spectral response also within the RE domain (Curran et al., 1990; Jacquemoud & Baret, 1990; Zarco-Tejada et al., 2001; Zarco-Tejada et al., 2018). At the same time, Ollinger (2011) pointed out that the variation in SVIs involving VIS and NIR bands is often driven to a greater extent by the variation in NIR reflectance than by variation in the VIS reflectance. In this context, the impact of canopy structure on SVIs still needs to be clarified.

The aforementioned controversies highlight that the response of structural traits, in combination with biochemical ones, on reflectance and on the SVIs models accuracy has not been fully characterized for different canopy types. To this regard, more efforts are needed to characterize the spectral response in the RE reflectance domain—in heterogeneous canopies—at varying biochemistry and structure, and more specifically to analyze the impact of canopy structural and leaf traits co-variation on SVIs-LAI relationships (Inoue et al., 2016) Such characterization is particularly important for multi-species natural grassland canopies, characterized by high spatial heterogeneity and temporal phenological changes, as presented in Section 2.3.4. Darvishzadeh et al. (2008a) concluded that LAI estimation in grasslands with mixed species and heterogeneous architecture is challenging and that detailed investigations are needed to assess the suitability of different remote sensing models when many combinations of several species are observed.

In this framework, the objectives of the present study were:

- To compare the ability of different SVIs including information from the RE and the NIR-shoulder spectral regions to estimate LAI at both temporal and spatial scales using ground hyperspectral data
- To analyze the potential of Sentinel band combinations across the RE and the NIR-shoulder spectral regions using S-2 and S-3 simulated bands to estimate LAI in two grassland ecosystems of the Alps with contrasting structures

- To determine the impact of grassland structural and biochemical heterogeneity on LAI estimations by analyzing the spectral reflectance response to co-varying biochemical and structural leaf and canopy traits across the RE and NIR-shoulder spectral domain using an RTM approach
- To identify the best performing S-2 and S-3 SVIs for monitoring grasslands with heterogeneous structure by describing the impact of co-varying leaf and canopy structural traits on the relationships between LAI and SVIs calculated from S-2 and S-3 bands, as well as comparing RTM and empirical approaches.

2.2. Materials and Methods

2.2.1. Study Sites

This study was conducted in two different grassland sites of the Italian and Austrian Alps (Figure 2), situated in the subalpine and montane vegetation belts, respectively, and characterized by contrasting management types.

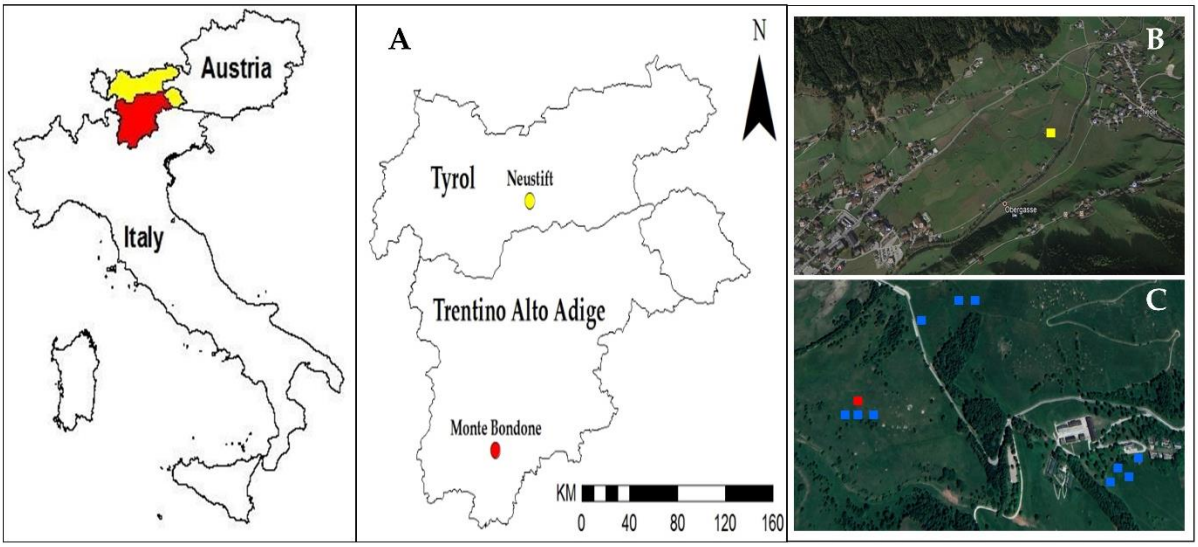

Figure 2. Location of the study sites (A); RGB Google Earth image of the AT-Neu site, where the yellow square represents the plot for temporal observations (B); and RGB Google Earth image of the IT-MBo site, where the red square represents the plot for temporal observations, while the blue squares represent the plots for spatial observations (C).

The first site is a permanent meadow at the Viote del Monte Bondone plateau (46.0147N–11.0458E, Italian Alps). The plateau meadow is managed mostly extensively, with low mineral fertilization and one cut annually around mid-July. In its central part, the meadow hosts a Fluxnet Eddy Covariance (EC) tower (IT-MBo, Italy). Due to its heterogeneous management and orography, the plateau is characterized by the presence of different grassland types characterized by extremely varying LAI and biomass (Sakowska et al., 2019). Such heterogeneous meadows include several different vegetation types (two most abundant associations, one of them including two variants (Sakowska et al., 2019)). The *Sieverso-Nardetum strictae* association (average aboveground biomass: 236 $g \cdot m^{-2}$ Sakowska et al., 2019) coves a high portion of the plateau, including the EC footprint, and is characterized by short canopies and not intensively managed.

The *Scorzonero Aristatae-Agrostidetum tenuis* (average aboveground biomass: 384 $g \cdot m^{-2}$) association is also very common on the plateau; it grows on calcareous soils and includes very productive species, which, although typical of much lower altitudes, can be frequent in some of the most fertile and well-exposed areas of the plateau (e.g., *Arrenatherum elatius* and *Dactylis glomerata*). The plateau, in its Eastern part, consists of small peatland associations of *Caricion fuscae* and *Caricion davallianae* characterized by very high productivity (Sakowska et al., 2019).

At the IT-MBo, several different ecosystems with extremely contrasting structures and productivity can be found within a few hundred of meters distance (Figure S1). The vegetation in sampling Plots 4 - 7 was very tall (maximum height reached 120 cm) and their structure was more erectophile, which is representative of the *Arrenatherion* alliance considered one of the most common vegetation types of Central Europe, at medium-lower altitudes. Vegetation in Plots 1–3 was very short with small dense *Nardus* tussocks and a limited number of scattered *Festuca* spikes (maximum height 50 cm). These plots represent, in their physiognomy, a typical grassland (meadow or pasture) on lime-deficient or acidified soils from the lower mountains of Europe, up to the lower alpine belt above the timberline. Vegetation in Plots 8–10 showed an intermediate height (maximum 90 cm) and was characterized by the presence of medium-productive grasses (such as *Agrostis Tenuis* and *Trisetum flavescens*) and forbs. This vegetation type is representative of a typical Centro-European species-rich mesophile grasslands at intermediate altitudes (between the *Arrenatherion* and *Nardus* types) of the montane and sub-alpine levels. The IT-MBo meadow soil can be classified as a Typic Hapludalfs, lyme loamy, mixed, mesic with the following characteristics in the 0–30 cm horizon: total soil organic content (SOC) = 9.4 ± 0.4 kg C m^{-2}; total N = 0.29 ± 0.02 kg N m^{-2}; and soil bulk density = 0.79 ± 0.29 g cm^{-3} (Papale et al., 2014).

The second site (AT-Neu, Fluxnet site) is a meadow located in Neustift (47.1162 N, 11.3204 E, Tyrol, Austria) classified as a *Pastinaco-Arrhenatheretum* (Wohlfahrt et al., 2008). The meadow shows very high productivity (with aboveground biomass values of up to 700 $g \cdot m^{-2}$ (Vescovo et al., 2012) and is intensively managed with three cuts in mid-June, at the beginning of August, and at the end of September. The vegetation type includes a few dominant graminoids (*Dactylis glomerata*, *Festuca pratensis*, *Phleum pratense* and *Trisetum flavescens*) and forbs which are abundant in terms of biomass and are characterized by wider leaves such as *Ranunculus acris*, *Taraxacum officinale*, *Trifolium repens*, *Trifolium pratense,* and *Carum carvi* (Figure S2, Wohlfahrt et al., 2008). The 1-m deep soil profile in AT-Neu meadow soil has been classified as a Fluvisol (FAO classification) with a very thin organic layer (up to 2 cm) and beyond which it is described as a sandy loam. The vegetation roots reach down to 50 cm, but 80% of them are concentrated in the upper 13 cm of the soil (Wohlfahrt et al., 2008).

2.2.2. Ground Biophysical Measurements

In the growing season of 2013, the fraction of absorbed photosynthetically active radiation (fAPAR) in IT-MBo was quantified at different vegetation development stages by periodic measurements (8 measurements in the period between May and July 2013) of incoming, reflected, and transmitted (2 repetitions) PAR using the SunScan Canopy Analysis System (Delta T Devices Ltd., Cambridge, UK). In 2014, the fAPAR in IT-MBo was estimated using continuous measurements in the period between June and July 2014 by means of the Li-COR PAR sensors (Li-COR Inc., Lincoln, Nebraska, USA). Two Li-190 Quantum sensors were installed above the canopy

level, measuring both incoming and reflected PAR, while the third sensor (Li-191 Line Quantum) was placed at the ground level, measuring PAR transmitted through the vegetation canopy.

The temporal patterns of fAPAR in AT-Neu in the growing season of 2018 were computed using continuous measurements in the period between April and May 2018 carried out with BF2H (Delta T Devices Ltd., Cambridge, UK) and QSO-Sun (Apogee Instruments, Inc., Logan, UT, USA) sensors measuring incoming and reflected PAR, respectively, and two SQ-316 Line Quantum sensors (Apogee Instruments, Inc., Logan, UT, USA) measuring transmitted PAR. In both ecosystems (IT-MBo, AT-Neu), the temporal scale measurements of transmitted PAR with line sensors were performed within the footprint of the ASD-WhiteRef hyperspectral system. All the PAR data were recorded by a data logger (CR3000 in IT-MBo 2014, CR1000 in AT-Neu 2018; Campbell Scientific Inc., Logan, Utah, USA) at 1-min intervals and averaged over solar noon (11:00–13:00 local solar time) to match the time period used for vegetation spectral properties calculations. The spatial patterns of fAPAR in the biomass peak season of 2017 in IT-MBo were quantified at 10 different grassland plots using the SunScan Canopy Analysis System (Delta T Devices Ltd., Cambridge, UK). Two fAPAR measurements were conducted along the transect of the sampling plots with the SunScan instruments, which consist of 64 PAR sensors embedded in a 1-m-long portable probe positioned underneath the grass canopy. In each plot, the probe was positioned along 2 diameter axes (one orthogonal to the other), thus providing 64 × 2 = 128 individual measurements, which were averaged prior to fAPAR calculation. Additionally, two measurements of reflected and incoming light were performed with the probe right above the canopy. The summary of biophysical measurements acquired in the study is presented in Table 1.

Table 1. Summary of spectral and biophysical measurements acquired in the study.

Study Site	Year	Observation Period	No. of Observations	Measurement Time Window	Observation Scale	Measurements
IT-MBo	2013	May 2013 - July 2013	8	Averaged over solar noon (11:00 - 13:00 of local solar time)	Temporal	Spectral fAPAR
	2014	June 2014 - July 2014	14	Averaged over solar noon (11:00 - 13:00 of local solar time)	Temporal	Spectral fAPAR
	2017	July 2017	10	Acquisition around solar noon (12:00 - 14:00 of local solar time)	Spatial	Spectral fAPAR
AT-Neu	2018	April 2018 - May 2018	49	Averaged over solar noon (11:00 - 13:00 of local solar time)	Temporal	Spectral fAPAR

The fAPAR was calculated as:

$$fAPAR = (PARi - PARr - PARt) \times PARi^{-1} \quad (3)$$

where PARi, PARr, and PARt are incident, reflected, and transmitted PAR, respectively.

LAI was estimated non-destructively by an indirect method based on canopy PAR transmission using PAR sensors data and a physical model of radiative transfer “INVERSION”

(Wohlfahrt et al., 2001). The model of radiative transfer considers the canopy as a turbid medium in which multiple scattering occurs due to elements of turbidity (phytoelements). The model uses four adjustable parameters: (1) phytoelement dispersion factor; (2) phytoelement reflection; (3) transmission coefficients; and (4) soil reflection. The LAD function for the investigated vegetation type was assumed as erectophile (Migliavacca et al., 2017), and it was used in "INVERSION" parameter settings. None of the other parameters (dispersion, reflectivity, transmissivity, and soil reflectivity) were determined for the investigated canopies, thus default values (Wohlfahrt et al., 2001) were used in the model to estimate the LAI.

2.2.3. Hyperspectral Reflectance Measurements

Hyperspectral reflectance data at both sites (in IT-MBo in the growing season of 2013 and 2014 and in AT-Neu in the growing season of 2018) were acquired (Table 1) on a continuous basis by means of the ASD-WhiteRef system (Sakowska et al., 2015), allowing measurements in the wavelength range between 350 and 2500 nm. The installation height (6 m in IT-MBo and 2.6 m in AT-Neu) and the system FOV (25 deg) resulted in an optical canopy footprint diameter of about 2.7 and 1.1 m in IT-MBo and AT-Neu, respectively. Both the ASD-WhiteRef narrow-band reflectance spectra were averaged over 2 h close to the solar noon (11:00–13:00 local solar time) to minimize the solar angle effects and then used for computing the SVIs.

In addition, in 2017, spectral observations were performed in the spatial domain in IT-MBo plateau by deploying the ASD FieldSpec Pro spectroradiometer (Analytical Spectral Devices, Inc., Boulder, CO, USA) equipped with a fiber optic with the field of view of 25 deg and a white reference panel on a custom-made aluminum portable system (of a height of 2 m and the resulting FOV of ca. 0.9 m, Figure S3) designed for periodic nadir observations. The portable system consisted of a vertical pole equipped with two horizontal arms (installed one above another; the upper one was fixed and served the fiber optic assembly; the second arm—placed 20 cm below—was rotatable and allowed the installation of the white reference panel) enabling alternating observations of the reference and the vegetation target and a ground structure ensuring system stability.

The spatial observations were carried out in July 2017 in 10 different grassland plots covering the aforementioned vegetation types and characterized by quite diverse canopy structure (Figure S1) and productivity (Sakowska et al., 2019). The canopy structure of the investigated grasslands was ranging from very short and dense canopies with Nardus Stricta (typical of high altitudes: V1–V3; Figure S1) to very productive grasslands with tall species such as *Dactylis Glomerata* and *Arrenatherum elatius* (V4–V7; Figure S1). For the spatial observations, the field campaign was conducted at the biomass peak to explore as many plots as possible within a short period (3 days) to avoid grass phenological changes (browning of the vegetation) and to ensure clear-sky conditions. The number of spatial scale observations was in general lower than that of temporal observations, as the latter were carried out on a more continuous basis.

2.2.4. Best Band Combination and Hyperspectral NDIs

To identify the band combinations most sensitive to LAI, the normalized difference index (NDI = (B1 − B2)/(B1 + B2), where B1 and B2 refer to reflectance values at specific ASD-WhiteRef bands) was calculated with all possible two-band combinations based on ASD ground

hyperspectral data within the VIS and NIR spectral range (350–1000 nm) at 1- nm resolution. The definition of the two-band NDIs used in this study is presented in Figure 3. The 2D correlograms for B1 (350–1000 nm) versus B2 (350–1000 nm) highlight the performance of SVIs in the different spectral regions: the VIS region (400–680 nm), the RE region (680–750 nm), and the NIR-shoulder region (750–900 nm). The correlograms were generated using the "Spectral Indices (SI) assessment toolbox" from a modular software package ARTMO (Automated Radiative Transfer Models Operator) (Verrelst et al., 2015a). The SI ARTMO toolbox facilitates the assessment of spectral-domain prediction efficiency based on the adopted SI formulation and generates the correlation (R^2) matrices with all possible two-band combinations between measured and estimated values for any biophysical parameter (Verrelst et al., 2015b). The 2D correlograms illustrate the performance of all two-bands normalized difference combinations in retrieving LAI.

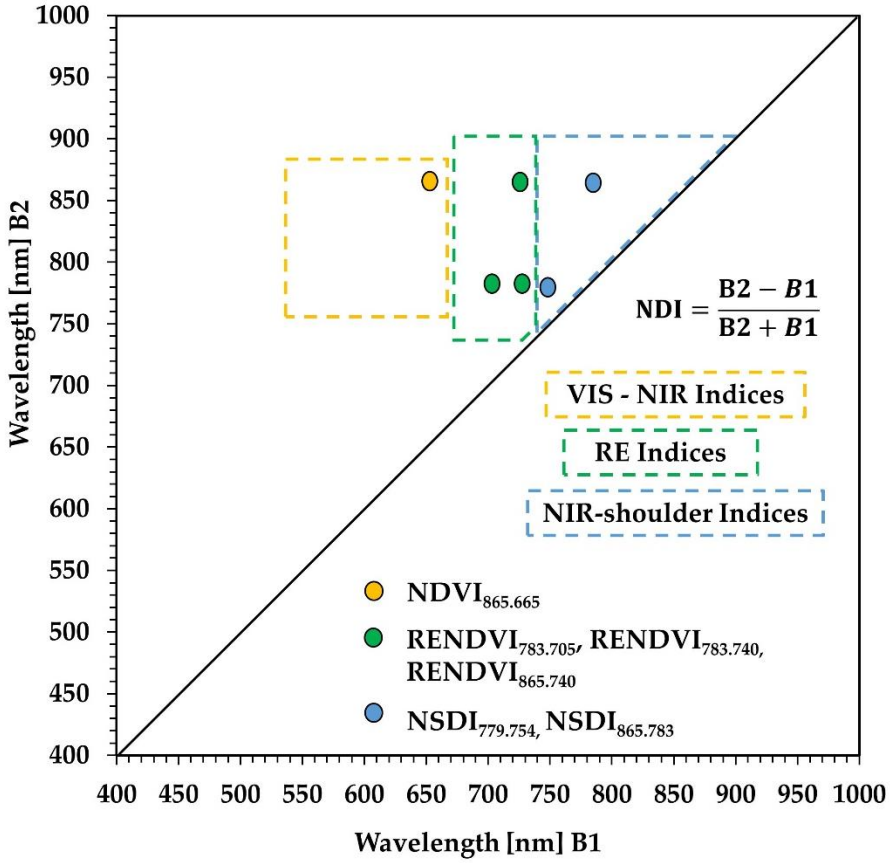

Figure 3. VIS-NIR, RE, and NIR-shoulder (yellow, green, and blue boxes, respectively) band combinations used to calculate normalized difference indices (NDIs). "NDI = (B1-B2)/(B1+B2)" represents the general formula for calculating NDIs, where B1 and B2 refer to reflectance at two different bands.

2.2.5. Multispectral Sentinel 2 and 3 SVIs

To obtain the reflectance values in the S-2 and S-3 bands, a simulation approach considering the average reflectance over the bandwidth of the respective S-2 and S-3 bands was adopted following Peng et al. (2017). SVIs based on S-2 and S-3 simulated bands (Table S1) in the VIS-NIR, RE, and NIR-shoulder spectral regions were calculated, and their potential for estimation of grasslands LAI was tested. Two SVIs ($NDVI_{865.665}$ and MTCI) were based on VIS and NIR reflectance (referred to as VIS-NIR SVIs), three SVIs ($RENDVI_{783.740}$, $RENDVI_{783.705}$, and

$RENDVI_{865.740}$) were based on RE and NIR reflectance (referred to as RE SVIs) and the other two SVIs ($NSDI_{779.754}$ and $NSDI_{865.783}$) were based on the NIR-shoulder reflectance (≥ 750 nm; referred to as NIR-shoulder SVIs). We chose to compare the performance of two VIS-NIR SVIs (as a reference), alongside the performance of three RE making use of a RE band and two NIR-shoulder indices (Table 2).

Table 2. SVIs based on S-2 and S-3 bands.

SVIs Group	SVIs	Other Names	Formula	References
VIS-NIR	$NDVI_{865.665}$		(8a−B4)/(8a+B4)	(Rouse et al., 1974)
	MTCI		(8a−B5)/(B5−B4)	(Sakowska et al., 2016)
Red-Edge	$RENDVI_{783.740}$		(B7−B6)/(B7+B6)	(Peng et al., 2017)
	$RENDVI_{783.705}$	NDre2	(B7−B5)/(B7+B5)	(Fernández-Manso et al., 2016; Peng et al., 2017)
	$RENDVI_{865.740}$	NDVIre2n	(8a−B6)/(8a+b6)	(Fernández-Manso et al., 2016; Sakowska et al., 2019)
NIR-Shoulder	$NSDI_{779.754}$[1]		(O16−O12)/(O12+O16)	Proposed in this study
	$NSDI_{865.783}$	NDVIre3n	(8a−B7)/(8a+B7)	(Fernández-Manso et al., 2016)

[1] S-3, simulated index. Fernández-Manso et al. (2016) referred to $RENDVI_{783.705}$ as Normalized Difference RE 2 (NDre2), $RENDVI_{865.740}$ as Normalized Difference Vegetation Index RE 2 narrow (NDVIre2n), and $NSDI_{865.783}$ as Normalized Difference Vegetation Index RE 3 narrow (NDVIre3n).

2.2.6. Global Sensitivity Analysis

Different factors (e.g., background soil and Solar-object-sensor geometry parameters) besides the biochemical and structural traits affect the canopy reflectance. To investigate the impact of structural PTs on reflectance, the ARTMO Global Sensitivity Analysis (GSA) toolbox was used (Inoue et al., 2016). The Variance-based GSA enables evaluating the relative importance of the spectral bands by identifying relative contribution (SI) of the key input variables that drive RTM spectral outputs (Wohlfahrt et al., 2001). The PROSAIL model input parameters used in this study for the GSA analysis are summarized in Table 3. The biochemical and structural input variables of the PROSAIL RTM model co-varied between the minimum and maximum value and for the geometrical parameters used the fixed averaged value.

Table 3. Input parameters used in the global sensitivity analysis (GSA). LAI was estimated from the canopy fAPAR measurements at IT-MBo. The ranges of other input parameters (N, Cab, Car, Cw, Cm, Cbrown, soil and LAD) were selected based on existing literature (Verrelst et al., 2016; Darvishzadeh et al., 2008a; Pasolli et al., 2015; Zhang et al., 2018; Melendo-Vega et al., 2018).

PROSAIL Parameters	Symbol	Unit	Minimum Value	Maximum Value	Avg/Fixed Value
Leaf structural parameter	N	-	1.5	1.9	1.7
Leaf chlorophyll content	Cab	µg cm^{-2}	40	70	55
Carotenoid content	Car	µg cm^{-2}	3.75	12.65	8.2
Brown pigment	Cbrown	-	0	0.2	0.1
Leaf water content	Cw	mg cm^{-2}	0.01	0.05	0.03
Leaf dry matter	Cm	mg cm^{-2}	0.005	0.01	0.007
[1] Leaf area index	LAI	$m^2 \cdot m^{-2}$	0.3	3.7	2
Leaf angle distribution	LAD	(deg)	0	90	45
Hotspot	H	-			0.01
Soil Reflectance	soil	-	0	1	0
Solar zenith angle	θ_S	(deg)			25
Observation zenith angle	θ_v	(deg)			0
Relative Azimuth Angle	φ	(deg)			0

[1] Estimated from fAPAR field measurements.

2.2.7. SVIs Performance Using Simulated Spectra Under Different Temporal and Spatial Scenarios

RTMs are used to understand light interception by plant canopies and for the interpretation of vegetation reflectance in terms of biophysical characteristics (Verrelst et al., 2016). In this study, the PROSAIL RTM (Verrelst et al., 2015a) was used to assess the influence of leaf and canopy PTs on the SVIs calculated based on VIS, RE and NIR-shoulder spectral regions. PROSAIL couples two separate models: (a) the PROSPECT leaf optical model; and (b) the SAIL canopy reflectance model (Danner et al., 2019). PROSAIL can simulate the canopy bidirectional reflectance in the spectral range between 400 and 2500 nm as a function of up to 16 input parameters. In this study, the input parameters were constrained according to the ranges of biophysical parameters measured in the field and literature-based values (Table 3). A look-up table (LUT) generated using the Latin hypercube sampling (LHS) method (Liu et al., 2015) was adopted to achieve a uniform distribution of the model inputs within the given boundaries for each scenario. The LHS method divides the cumulative density function into n bins of the same size from which data are randomly selected.

To investigate the impact of structural (LAI, LAD, leaf structural parameter (N) and leaf dry matter (Cm) and biochemical (leaf chlorophyll content (Cab), carotenoid content (Car), brown pigment content (Cbrown), and leaf water content (Cw)) input parameters of PROSAIL on canopy spectral reflectance, various scenarios were assumed.

Using co-variation between input variables to constrain the model, we adopted parameters ranges observed in the literature (Table 3). With this approach, we aimed at exploring the impact of traits co-variation at both the spatial scale (due to vegetation heterogeneity) and the temporal scale (due to grassland phenological changes). Hence, running PROSAIL with a 100-iteration step, we analyzed four scenarios (1t–4t) based on the LAI range observed at the temporal scale at IT-MBo (during the growing period), as follows:

(1t) LAI was set to vary between the minimum (at the beginning of the season) and the maximum value (at the biomass peak) and other PROSAIL parameters were kept constant (average value). This corresponds to a theoretical scenario where only grassland canopy LAI changes during the growth period, and no change is assumed in both other canopy structural parameters and biochemistry.

(2t) LAI and LAD values were co-varying between the minimum and the maximum value (Table 4) during the growth period and the rest of the PROSAIL parameters were kept constant (average value). This scenario can be considered representative of grasslands with slight canopy architectural and leaf structural dynamics at different growth stages.

Table 4. Different scenarios analyzed with the PROSAIL simulation at the temporal (1t–4t) and spatial (1s–4s) scales.

PROSAIL Simulation Scenarios	**1t/1s**	**2t/2s**	**3t/3s**	**4t/4s**
Scenarios at the Temporal Scale (1t–4t)	LAI varying between minimum and maximum values (temporal scale field observations)	LAI co-varying between minimum and maximum values (temporal scale field observations) LAD: 0–90	LAI co-varying between minimum and maximum values (temporal scale field observations) LAD: 0—90 N: 1.5—1.9 Cm: 0.005—0.01	All PROSAIL parameters co-varied.
Scenarios at the Spatial Scale (1s–4s)	LAI varying between minimum and maximum values (spatial scale field observations)	LAI co-varying between minimum and maximum values (spatial scale field observations) LAD: 0—90	LAI co-varying between minimum and maximum values (spatial scale field observations) LAD: 0—90 N: 1.5—1.9 Cm: 0.005—0.01	All PROSAIL parameters co-varied.

(3t) LAI, LAD, N and Cm values were co-varying between the minimum and the maximum value (Table 4) and the rest of the PROSAIL parameters (Table 3) were kept constant at the average value. This corresponds to a scenario where all canopy and leaf structural traits change during the growing season (due to, e.g., ecological factors such as temperature, soil moisture and light competition), but biochemical traits remain constant. This scenario can be associated with grasslands where phenology, species composition and management practices (e.g., architectural changes due to variation of species composition after mowing and leaf biochemical changes due to fertilization) are determining more evident both canopy architectural and leaf structural traits dynamics at the temporal scale.

(4t) All the PROSAIL input variables (Table 4) were allowed to co-vary from the minimum to the maximum value. This corresponds to a scenario where there is a relevant temporal co-variation of both canopy structural and biochemical traits. Such scenario can be considered representative of grasslands with more extreme phenology dynamics, due to: (i) stronger changes of ecological

factors related to climate dynamics and water availability (e.g., in Mediterranean grasslands with strong seasonal variations of leaf water content, leaf chlorophyll content, and proportion of brown dead leaves); or (ii) management practices (e.g., architectural changes due to variation of species composition after mowing and leaf biochemical changes due to fertilization).

The PROSAIL model was also run with a 100-iteration step for four scenarios (1s–4s) using the range of LAI measured during spatial observations (minimum and maximum values measured in the field at the biomass peak) as an input parameter (Table 4) as follows:

(1s) LAI was set to vary between the minimum (in the less productive grassland) and the maximum value (in the most productive grassland) and other PROSAIL parameters were kept constant at their average value. This corresponds to a theoretical scenario where the grassland is spatially homogeneous in terms of both structure and biochemistry.

(2s) LAI and LAD values were set to vary between the minimum and the maximum value and other PROSAIL parameters (Table 4) were kept constant (average value). This scenario can be considered representative of grasslands with slightly spatially-heterogeneous species composition and functional types.

(3s) LAI, LAD, N and, Cm values were co-varying between the minimum and the maximum value and, other biochemical parameters were kept constant. This scenario corresponds to a grassland with strong structural spatial heterogeneity, while biochemistry is homogeneous. It can be associated with grasslands with heterogeneous species composition and functional types, associated with spatial variation of ecological factors (e.g., soil moisture and pH, topographic aspect, etc.).

(4s) All the PROSAIL parameters were co-varying. This scenario corresponds to a grassland with strong structural and biochemistry spatial heterogeneity and can be considered representative of grasslands with extreme variations of species composition, plant functional types, ecological factors, and management regimes.

All PROSAIL simulations were performed using the MATLAB environment (The MathWorks Inc. 2019a).

2.2.8. Statistical Analysis

To compare the performance of the investigated NDIs in LAI estimation, the following linear and second-order polynomial regression statistics were computed: R^2, coefficient of determination; Adj. R^2, adjusted coefficient of determination; and RMSE, root mean square error. All statistical analyses were performed by means of the R software (version 3.6.0, https://www.r-project.org/).

2.3. Results

2.3.1. Relationship between the Measured Spectra and LAI

Temporal trends of LAI in IT-MBo (2013 and 2014) and in AT-Neu (2018) are shown in Figure 4A–C, respectively. Figure 4D presents LAI corresponding to spatial observations. For temporal scale observations, the values of LAI at IT-MBo ranged from 0.3 to 3.7, while, at AT-Neu, LAI ranged from 0.2 to 8.8 and showed a smoother LAI increase compared to IT-MBo. At the spatial scale in IT-MBo, as the measurements were carried out at the biomass peak, the variability was lower and the LAI ranged from 2.0 to 4.5.

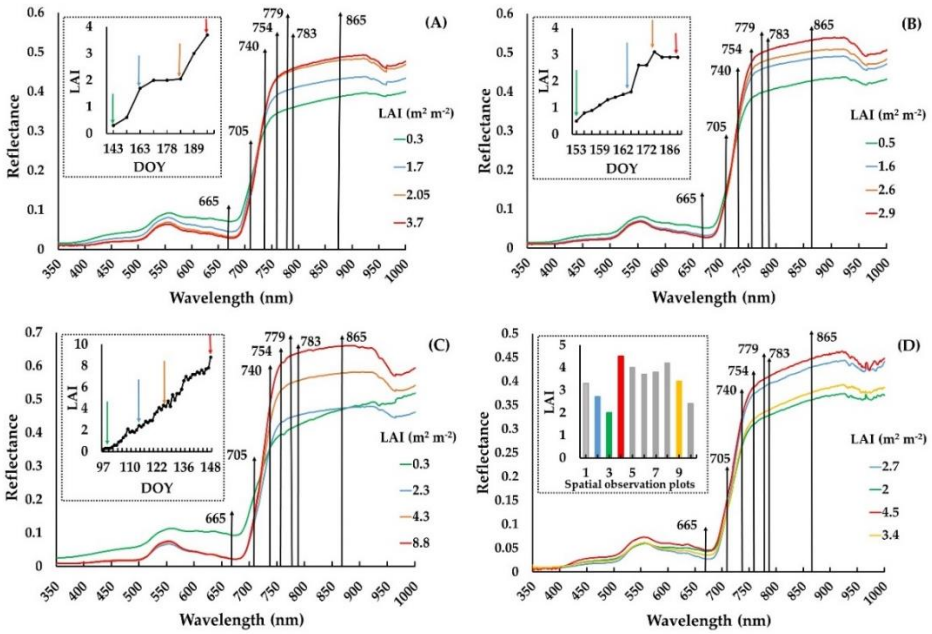

Figure 4. Reflectance spectra at different growth stages measured in the field at: IT-MBo 2013 (**A**); IT-MBo 2014 (**B**); and AT-Neu 2018 (**C**); and spectra from spatial observations at IT-MBo 2017 (**D**).

The canopy reflectance obtained from field measurements performed at different vegetation growth stages is plotted in Figure 4A–C (IT-MBo 2013, IT-MBo 2014 and AT-Neu 2018, respectively), while reflectance spectra obtained from spatial scale measurements (IT-MBo 2017) are displayed in Figure 4D. In the case of temporal observations, canopy reflectance showed a typical response to LAI increase, mostly characterized by a gradually decreasing reflectance in the VIS region, a gradually increasing reflectance in the NIR-shoulder region and increasing NIR-shoulder slope as observed by Vescovo et al. (2012). On the contrary, the reflectance values of spatial scale observations at IT-MBo 2017 showed a much more complex pattern (Figure 4D), where increasing values of LAI did not always result in higher NIR and lower visible reflectance. As an example, the grassland plot highlighted in yellow (with a relatively high LAI value of 3.4) had a very low NIR reflectance, while the grassland plot highlighted in red (LAI 4.5, corresponding to the highest LAI value) showed the highest reflectance in the visible wavelengths.

The reflectance values at 740 nm appeared to be relatively closer to the ones of the NIR shoulder plateau at AT-Neu 2018 compared to IT-MBo 2013, IT-MBo 2014 and IT-MBo 2017, suggesting a lower chlorophyll absorption at this wavelength in this ecosystem. The NIR-shoulder slope, between 760 and 900 nm, observed in AT-Neu 2018 was generally slightly less steep compared to the slope observed in IT-MBo in both temporal and spatial scale observations.

2.3.2. Best Band Combination and Hyperspectral NDIs

Figure 5 shows the R^2 resulting from the linear regression between LAI and two-band combinations of reflectance values from 350 to 1000 nm using hyperspectral data. The correlograms based on temporal observations from IT-MBo (2013 and 2014) and AT-Neu (2018) provided a clear overview of the optimal band combinations for retrieving LAI. In the case of IT-MBo temporal observations (Figure 5A,B), the R^2 values displayed very consistent patterns across VIS-NIR band combinations, but with slightly different R^2 ranges for both investigated years: the

maximum R^2 was around 0.8 for IT-MBo 2013 and 0.9 for IT-MBo 2014 and the minimum R^2 was slightly higher for IT-MBo 2013 compared to IT-MBo 2014. At the AT-Neu study site, generally lower R^2 values were observed compared to the IT-MBo temporal observations. In the VIS spectral region, a slightly different pattern of the R^2 values was observed for both study sites (Figure 5C). The R^2 patterns were more different across the RE and NIR-shoulder regions. In particular, an evident shift of the well-correlated areas towards the lower wavelengths (from around 750 nm to 740 nm) was observed for AT-Neu (Figure 5C) compared to IT-MBo temporal observations (Figure 5A,B).

All the two bands NDIs (Table 2) showed high R^2 values for temporal scale observations at IT-MBo ($R^2 > 0.75$, $NDVI_{865.665}$, $RENDVI_{783.740}$, $RENDVI_{783.705}$, $RENDVI_{865.740}$ and $NSDI_{779.754}$ in Figure 5A,B), except for the $NSDI_{865.783}$ index ($R^2 < 0.3$, Figure 5A,B). For AT-Neu, a slightly different pattern of R^2 values was observed, where $RENDVI_{865.740}$ and $NSDI_{779.754}$ showed very low correlations compared to IT-MBo ($R^2 > 0.2$, Figure 5C). The best correlations at the AT-Neu site were observed for the RENDVI NDIs ($RENDVI_{783.740}$ and $RENDVI_{783.705}$) with R^2 values exceeding 0.6 (Figure 5A–C). Therefore, the $RENDVI_{783.740}$, which is still not very commonly used in the literature, performed well at both sites. Although the NIR-shoulder $NSDI_{779.754}$ showed a significant correlation with high R^2 values ($R^2 > 0.85$ Figure 5A,B) at the IT-MBo site, much lower R^2 values were observed for the same band combinations at At-Neu ($R^2 < 0.2$, Figure 5C).

Other than the aforementioned SVIs, there is a wide range of band combinations that showed a strong correlation with LAI. For both sites, an area of high R^2 values ($R^2 > 0.7$) was observed for combinations within the NIR part of the spectrum (B2 around 950–970 nm and B1 of 900–950 nm: Figure 5A–C). Such band combinations are commonly used to calculate water band SVIs which are indicators of water status (Babar et al., 2006; Claudio et al., 2006; Gutierrez et al., 2010; Peñuelas et al., 1994; Prasad et al., 2007). On the other hand, water band SVIs demonstrated to be good proxies of structure-related parameters such as LAI and phytomass (Vescovo & Gianelle, 2008; Ustin et al., 2004). A strong correlation between Normalized Water Index (NWI; calculated with PRISMA bands B2 of 962 nm and B1 of 897 nm, Gutierrez et al., 2010; Peñuelas et al., 1994; Sims & Gamon, 2003) and LAI was observed (R^2 value for IT-MBo 2013 = 0.77, for IT-MBo 2014 = 0.83 and for AT-Neu 2018 = 0.85).

The correlogram based on S-2 (Figure 5D–F) and S-3 (Figure 5G–I) bands provides an overview of the performance of band combinations obtained with the average reflectance over the bandwidth of the respective S-2 and S-3 bands. For both study sites, the S-2 graph indicated that the RENDVI based on wavelength 740 and 783 nm is among the best correlated with LAI ($R^2 > 0.65$, Figure 5D–F). For S-3 simulated data, $NSDI_{779.754}$ showed very high correlations for IT-MBo ($R^2 > 0.75$, Figure 5G, H) but very low correlations at AT-Neu. Moreover, we also analyzed the correlograms of RMSE based on temporal observations (Figure S4), showing that the RMSE patterns were mostly similar but inverse, as high R^2 values corresponded with low RMSE values and vice versa.

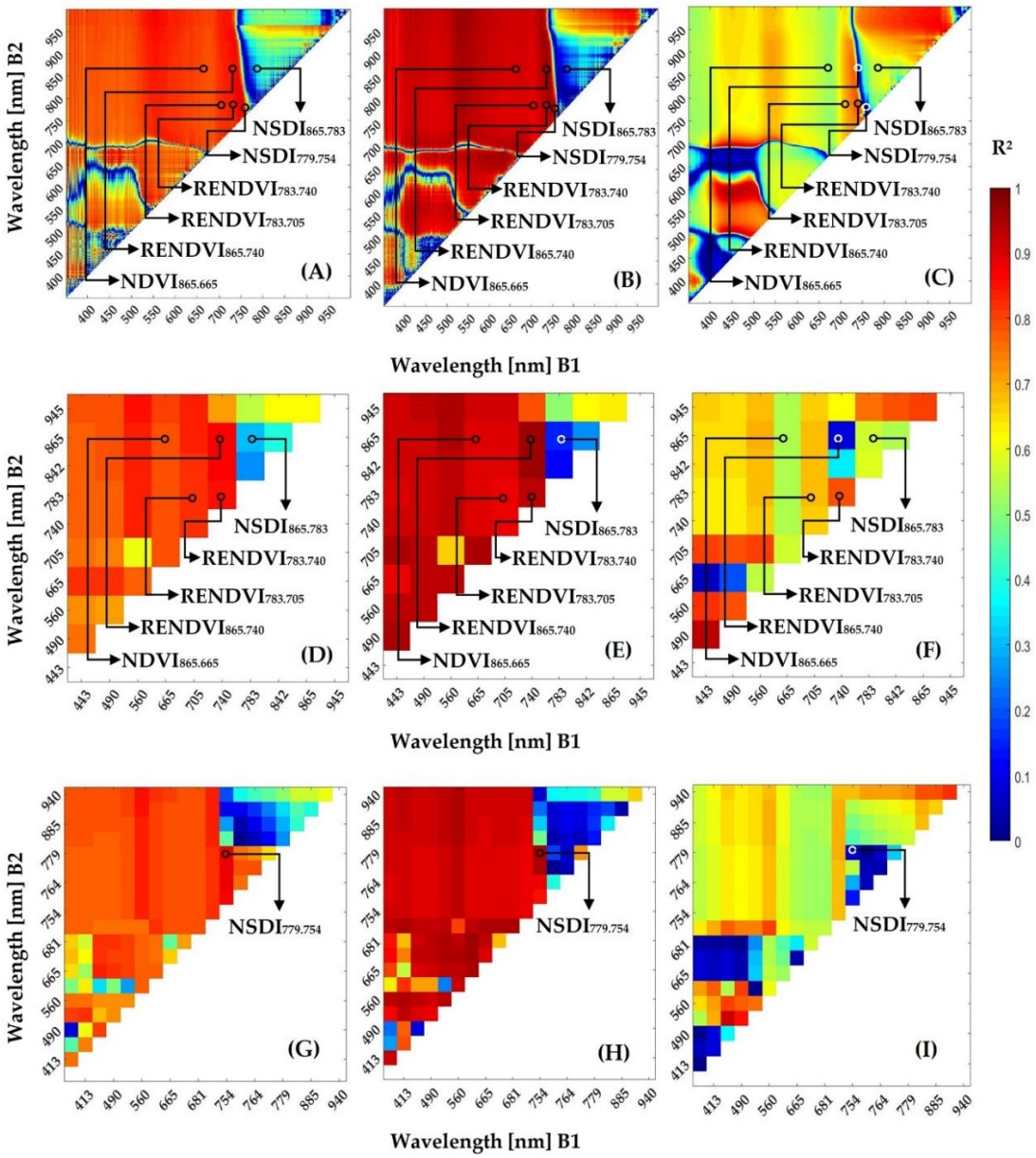

Figure 5. R^2 values based on linear regression between the normalized difference of all two-band combinations and LAI for both study sites (IT-MBo 2013 (**A**); IT-MBo 2014 (**B**); and AT-Neu 2018 (**C**)) considering the temporal scale hyperspectral observations. R^2 obtained using: (**A**–**C**) the hyperspectral data; (**D**–**F**) S-2 simulated bands; (**G**–**I**) S-3 simulated bands. Black/white circles refer to the position of the indices in the correlogram and arrows are indicating the name of the respective indices.

Results from the observations at the spatial scale at IT-MBo 2017 showed poorer correlations (Figure 6A) than those obtained with the multi temporal data. Only band combinations from the spectral range within 350–400 nm showed slightly higher R^2 values compared to the rest of the band combinations. The correlograms of RMSE based on spatial observations presented in Figure S5 showed overall high RMSE for most of the two band combinations.

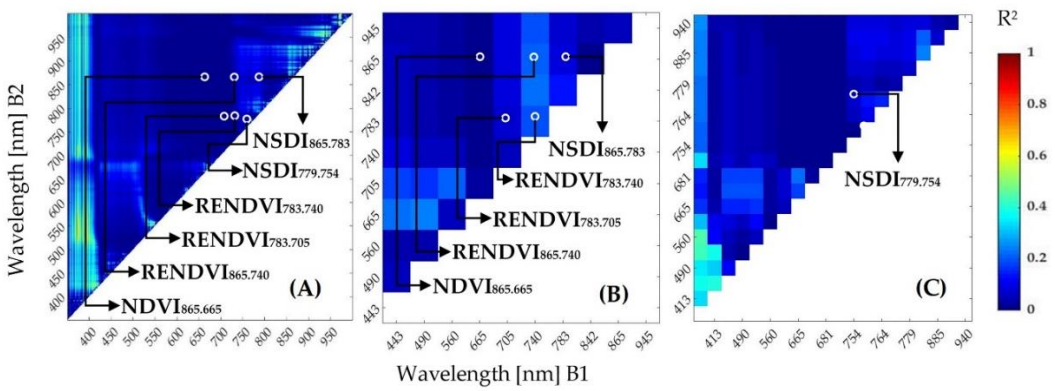

Figure 6. R^2 values based on linear regression between the normalized difference of all two-band combinations and LAI for IT-MBo 2017 considering the spatial scale observations: (**A**) R^2 obtained using the hyperspectral data; and (**B**,**C**) R^2 obtained using S-2 and S-3 simulated bands, respectively. White circles refer to the position of the indices in the correlogram and arrows are indicating the name of the respective indices.

2.3.3. The Performance of Multispectral Sentinel 2 and 3 SVIs

Scatterplots between VIS-NIR SVIs (calculated with data resampled to S-2 bands) and LAI for both sites are presented in Figure 7. Both investigated VIS-NIR SVIs ($NDVI_{865.665}$ and MTCI) showed a high correlation with an $R^2 > 0.75$ and RMSE < 0.5 $m^2 \cdot m^{-2}$ (Figure 7 A, B and Table 5) for observations on a temporal basis at IT-MBo. For the AT-Neu study site (which has very high productivity and LAI values up to 8.8), $NDVI_{865.665}$ showed a strong saturation effect (Figure 7A) compared to MTCI, resulting in a lower R^2 value (R^2 = 0.55 and R^2 = 0.81 for $NDVI_{865.665}$ and MTCI, respectively) and RMSE (RMSE = 1.71 $m^2 \cdot m^{-2}$ and RMSE = 1.11 $m^2 \cdot m^{-2}$, respectively). Conversely, when considering the observations at the spatial scale performed at IT-MBo, no significant correlation was found between the investigated VIS-NIR SVIs and LAI (Figure 7C,D and Table 5).

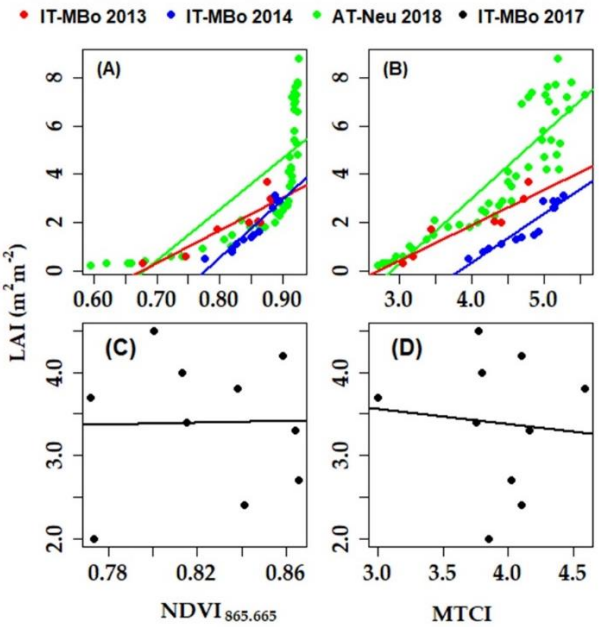

Figure 7. Relationship between VIS-NIR indices and LAI: for temporal observations at IT-MBo (2013 and 2014) and AT-Neu 2018 (**A**,**B**); and for spatial observations at IT-MBo 2017 (**C**,**D**). In all panels, solid lines represent a linear fit to the data.

Table 5. Summary of the statistics (N, Number of observations; R^2, coefficient of determination; Adj. R^2, adjusted coefficient of determination; RMSE, root mean square error) of the linear regression between leaf area index (LAI, $m^2 \cdot m^{-2}$) estimated from fraction of absorbed photosynthetically active radiation (fAPAR) and the spectral vegetation indices (SVIs) calculated from measured spectra for IT-MBo 2013, IT-MBo 2014 and AT-Neu 2018 at temporal scale observations and for IT-MBo 2017 at spatial scale observations. The three best-fitting models are highlighted in bold. Asterisk indicates significance of correlation: *** $p < 0.001$; ** $p < 0.01$; * $p < 0.05$. n.s., not significant (Pearson's correlation test).

SVIs	**Temporal Scale Observation**									**Spatial Scale Observations**		
	IT-MBo 2013 (N=8)			**IT-MBo 2014 (N=14)**			**AT-Neu 2018 (N=49)**			**IT-MBo 2017 (N=10)**		
	R^2	**Adj. R^2**	**RMSE ($m^2 \cdot m^{-2}$)**	**R^2**	**Adj. R^2**	**RMSE ($m^2 \cdot m^{-2}$)**	**R^2**	**Adj. R^2**	**RMSE ($m^2 \cdot m^{-2}$)**	**R^2**	**Adj. R^2**	**RMSE ($m^2 \cdot m^{-2}$)**
VIS-NIR												
$NDVI_{865.665}$	0.79**	0.76	0.48	0.90***	0.90	0.27	0.55***	0.54	1.71	$0.00^{n.s}$	-0.12	0.77
MTCI	0.83**	0.81	0.43	0.87***	0.86	0.32	**0.81*** **	**0.81**	**1.11**	$0.01^{n.s}$	-0.12	0.77
Red-Edge (RE)												
$RENDVI_{783.740}$	**0.85****	**0.83**	**0.40**	**0.93*****	**0.93**	**0.23**	**0.79*****	**0.78**	**1.18**	$0.03^{n.s}$	-0.09	0.76
$RENDVI_{783.705}$	0.82**	0.79	0.44	0.89***	0.88	0.30	**0.67*****	**0.66**	**1.47**	$0.00^{n.s}$	-0.12	0.77
$RENDVI_{865.740}$	**0.86****	**0.83**	**0.39**	**0.96*****	**0.96**	**0.17**	0.20**	0.18	2.28	$0.05^{n.s}$	-0.06	0.75
NIR-Shoulder												
$NSDI_{779.754}$	**0.88****	**0.86**	**0.37**	**0.95*****	**0.95**	**0.20**	0.09*	0.07	2.44	$0.04^{n.s}$	-0.08	0.75
$NSDI_{865.783}$	$0.28^{n.s}$	0.16	0.89	$0.15^{n.s}$	0.07	0.82	0.58***	0.57	1.66	$0.06^{n.s}$	-0.06	0.75

Scatterplots between RE-based SVIs (calculated with data resampled to S-2 bands) and LAI for both sites are presented in Figure 8. The R^2 values of the linear relationship between RE SVIs and LAI in IT-MBo were high with $R^2 > 0.8$ (up to 0.96 and RMSE < 0.45 $m^2 \cdot m^{-2}$) for the temporal observations at IT-MBo, but at the AT-Neu site the RE SVIs showed slightly lower R^2 (< 0.8 with RMSE > 1 $m^2 \cdot m^{-2}$) values, as a result of the saturation effect (Table 5). The saturation effect was particularly strong for $NDVI_{865.665}$ and for AT-Neu site, where a polynomial regression model showed to increase the R^2 from 0.55 to 0.71 and decrease RMSE from 1.71 to 1.37 $m^2 \cdot m^{-2}$. For all other SVIs, polynomial relationships showed only a slight increase of the performance of the model (Table S2). The RE SVIs including $RENDVI_{783.740}$ and $RENDVI_{783.705}$ from temporal scale observations showed a strong correlation with an $R^2 > 0.65$ for both study sites, but $RENDVI_{865.740}$ lost its predictive power at AT-Neu ($R^2 = 0.2$ and RMSE = 2.28 $m^2 \cdot m^{-2}$). As for VIS-NIR SVIs, the observations at the spatial scale showed very low R^2 (< 0.06) values.

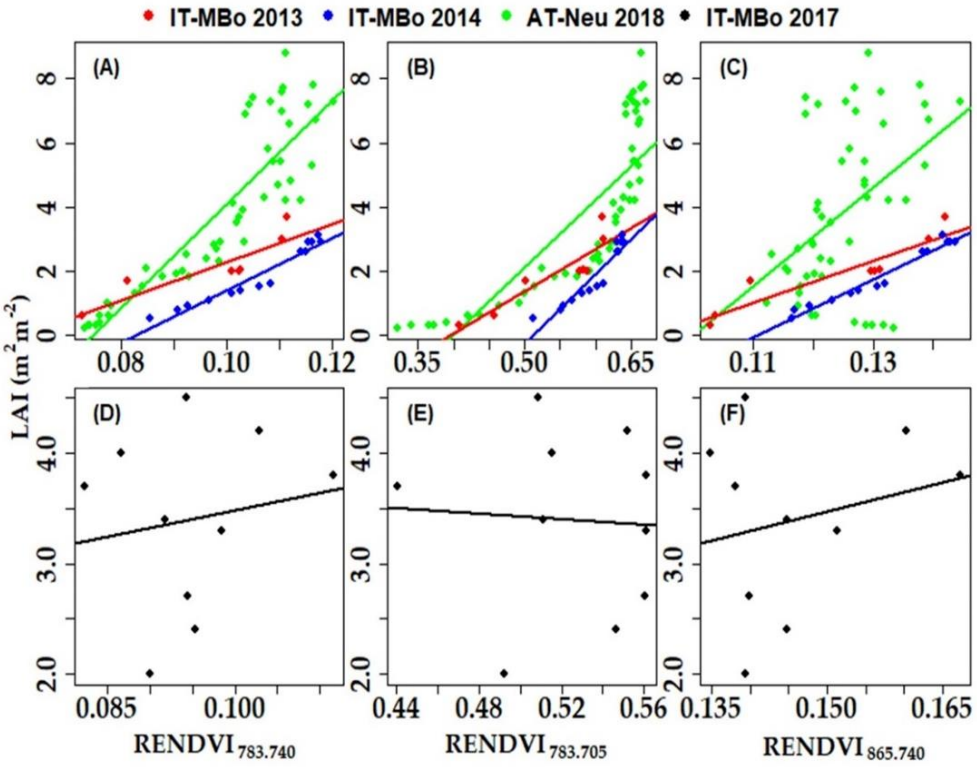

Figure 8. Relationship between RE indices and LAI: for temporal observations at IT-MBo (2013 and 2014) and AT-Neu 2018, respectively (**A**–**C**); and for spatial observations at IT-MBo 2017 (**D**–**F**). In all panels, solid lines represent a linear fit to the data.

Concerning the NIR shoulder SVIs, the $NSDI_{779.754}$ showed a strong positive correlation with an $R^2 > 0.8$ (up to 0.95 and RMSE < 0.40 $m^2 \cdot m^{-2}$) for the temporal observations at IT-MBo, but at the AT-Neu study site the correlation was much weaker ($R^2 < 0.1$, Figure 9A; RMSE = 2.44 $m^2 \cdot m^{-2}$, Table 5). The index based on 865 and 783 nm showed an inverse relationship with LAI for both ecosystems, with weaker correlation at IT-MBo ($R^2 < 0.3$) compared to AT-Neu (R^2 of 0.58, Figure 9B). No significant correlations were observed on the spatial basis (Figure 9C,D).

Considering all the VIS-NIR, RE and, NIR shoulder SVIs, $RENDVI_{783.740}$ was always among the three best-performing SVIs, for observations carried out at the temporal scale at the two

investigated sites (Table 5). The other SVIs with good performance at the temporal scale were RENDVI $_{865.740}$, MTCI, and NSDI$_{779.75}$.

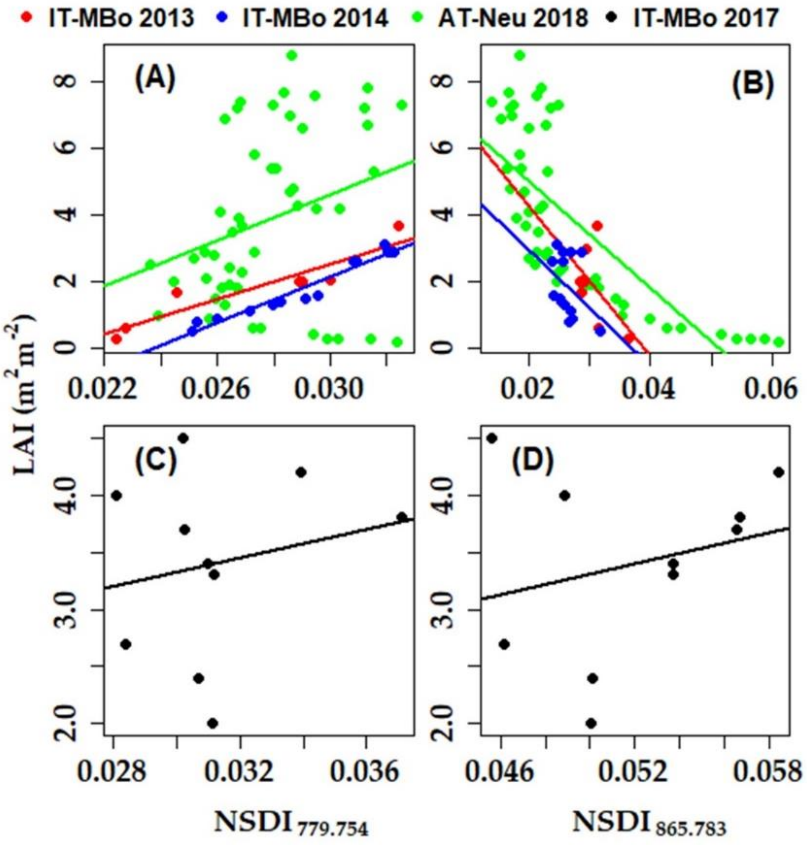

Figure 9. Relationship between NIR-shoulder indices and LAI: for temporal observations at IT-MBo (2013 and 2014) and AT-Neu 2018, respectively (**A**,**B**); and for spatial observations at IT-MBo 2017 (**C**,**D**). In all panels, solid lines represent a linear fit to the data.

2.3.4. Global Sensitivity Analysis of the Spectral Bands

The results concerning the impact of leaf and canopy parameters on the different spectral regions through the GSA are illustrated in Figure 10. Background (soil) demonstrated to have a rather homogeneous impact on canopy reflectance across all wavelengths. LAI and Cab demonstrated a major influence on reflectance in the VIS part of the spectrum and Cab showed two SI peaks (around 560 and 705 nm) and an impact on the reflectance response was observed up to 760 nm. Within the RE (680–750 nm) part of the spectrum, the influence of LAD was significantly increasing at longer wavelengths, with SI reaching about 40% at 740 nm, while at 705 nm the SI was less than 10%. For spectral bands in the RE region, a slight effect of Cbrown and Cm was also observed, while the impact of LAI was significantly increasing from RE to NIR-Shoulder spectral bands. LAI and LAD were the main drivers of reflectance also in the far RE region (740–750 nm) of the spectrum. Within the NIR-shoulder region (750–900 nm), reflectance showed to be driven mostly by LAI and LAD, while Cm showed an average SI value of less than 5%. In the spectral range 740–820 nm, Cbrown also showed SI values up to 5%. Leaf water content (Cw) response only started beyond 930 nm (Figure 10).

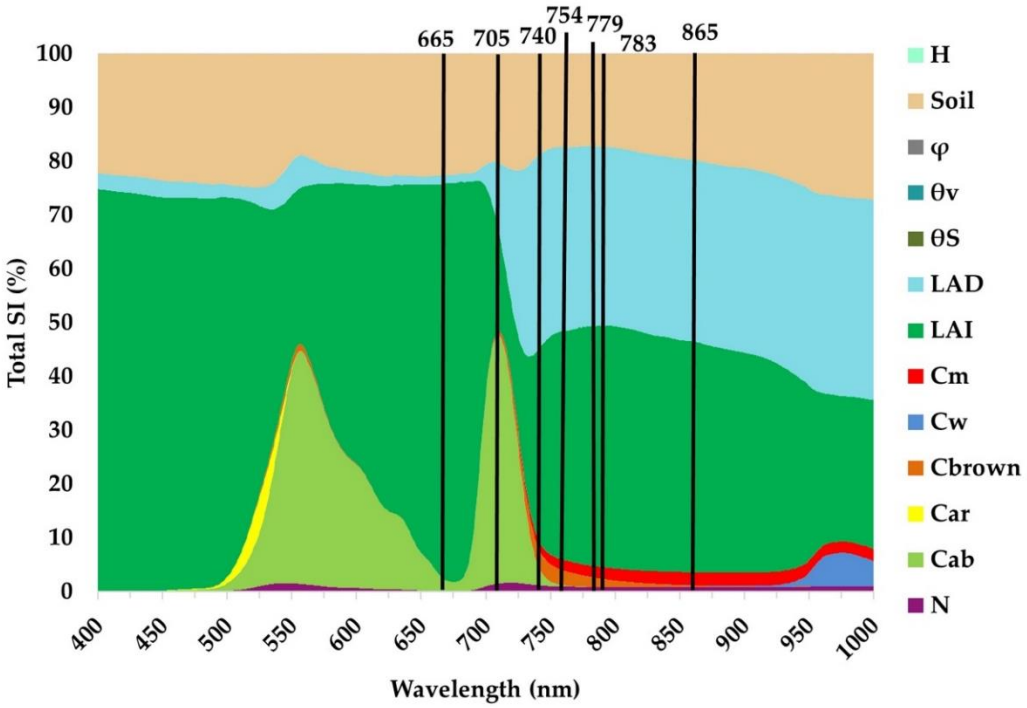

Figure 10. Global Sensitivity Analysis of the PROSAIL input parameters. The dimension of the sensitivity refers to the relative contribution (SI) of each input variable and the vertical bars represent the positions of the bands (solid lines, S-2; dotted lines, S-3) used to calculate the investigated SVIs. Input parameter ranges, full names of the variables and units are presented in **Table 3**.

2.3.5. SVIs Calculated from Modeled PROSAIL Reflectance Simulations vs. LAI

To analyze the impacts of co-variation of structural and biochemical traits for LAI monitoring using the PROSAIL modeled reflectance output, a series of scatterplots between the SVIs and LAI is presented in this section. The modeled reflectance was obtained from PROSAIL simulations constraining the input parameters according to the eight scenarios presented in Section 2.3.4.

For the investigated grasslands at IT-MBo, the LAI range observed at the temporal scale also included low LAI values (0.3), while the minimum LAI value for spatial scale observations was 2.0. In general, when LAI values were restricted to the spatial range, the lack of low LAI had a strong effect on the predictive power of VIS-NIR SVIs with a noticeable decrease in correlation coefficients when two or more traits were co-varying (Figure 11B–D F for $NDVI_{865.665}$ and Figure 11F–H for MTCI) and increase in RSME (Table 6 and Table 7).

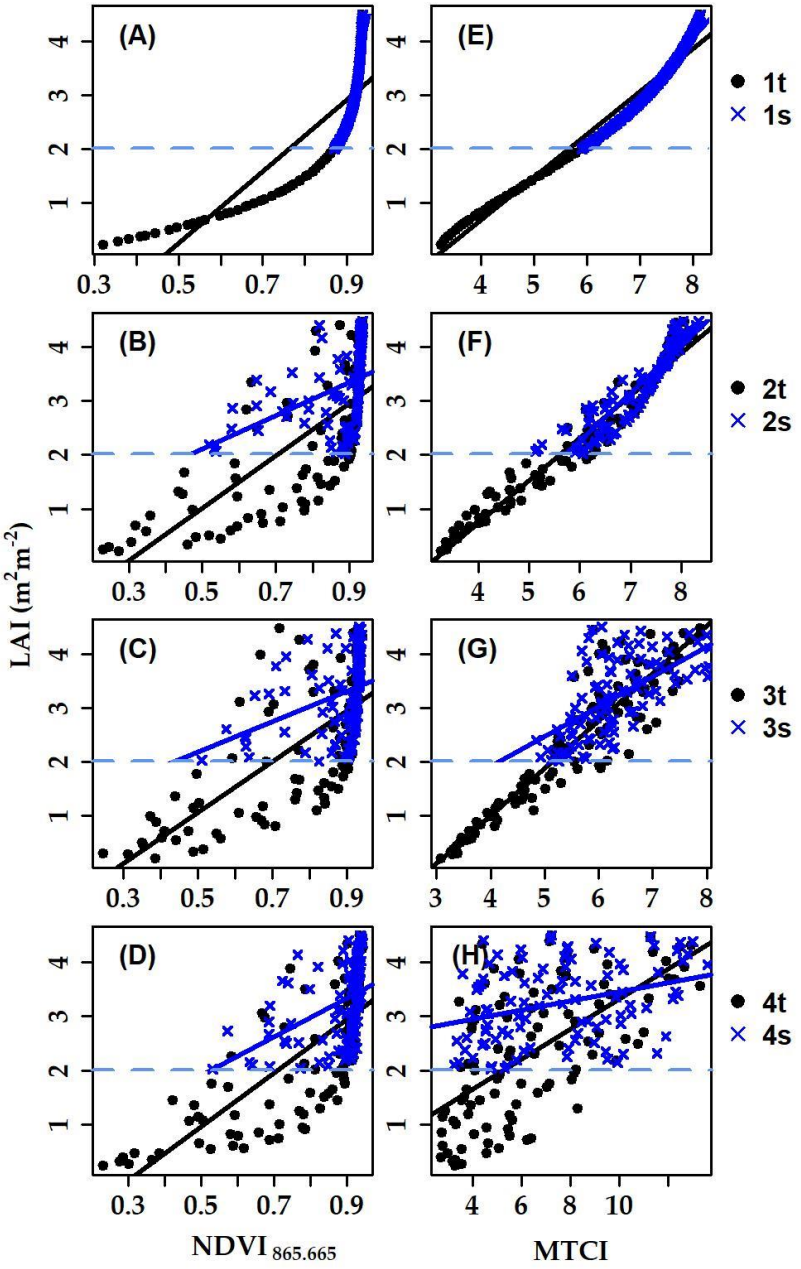

Figure 11. Relationships between VIS-NIR indices and LAI for all eight scenarios for both temporal ((**A**,**E**) 1t; (**B**,**F**) 2t; (**C**,**G**) 3t; and (**D**,**H**) 4t) and spatial scale observations ((**A**,**E**) 1s; (**B**,**F**) 2s; (**C**,**G**) 3s; and (**D**,**H**) 4s). The horizontal dashed line represents the minimum value of LAI when PROSAIL was run using spatial observation LAI ranges as input parameter. In all panels, solid lines represent a linear fit to the data.

Table 6. Summary of the statistics (N, number of observations; R^2, coefficient of determination; Adj. R^2, adjusted coefficient of determination; RMSE, root mean square error) of the linear regression between leaf area index (LAI, $m^2 \cdot m^{-2}$) of 100 iteration steps between minimum and maximum range of temporal scale measurements and the spectral vegetation indices (SVIs) calculated from PROSAIL simulated spectra by scenarios considering spatial scale LAI ranges (1t–4t) described in Section 2.3.4. The three best-fitting models are highlighted in bold. Asterisk indicates significance of correlation: *** $p < 0.001$; ** $p < 0.01$; * $p < 0.05$. n.s., not significant (Pearson's correlation test).

SVIs	**Scenario 1t, 2t, 3t, 4t**											
	1t (N=100)			**2t (N=100)**			**3t (N=100)**			**4t (N=100)**		
	R^2	**Adj. R^2**	**RMSE ($m^2 \cdot m^{-2}$)**	**R^2**	**Adj. R^2**	**RMSE ($m^2 \cdot m^{-2}$)**	**R^2**	**Adj. R^2**	**RMSE ($m^2 \cdot m^{-2}$)**	**R^2**	**Adj. R^2**	**RMSE ($m^2 \cdot m^{-2}$)**
VIS-NIR												
$NDVI_{865.665}$	0.73***	0.72	0.65	0.56***	0.56	0.82	0.52***	0.51	0.86	0.57***	0.57	0.81
MTCI	**0.98*** **	**0.97**	**0.20**	**0.95*** **	**0.95**	**0.26**	**0.85*** **	**0.84**	**0.49**	0.39***	0.38	0.97
Red-Edge (RE)												
$RENDVI_{783.740}$	0.95***	0.95	0.27	**0.93*** **	**0.93**	**0.34**	**0.90*** **	**0.90**	**0.40**	**0.64*** **	**0.63**	**0.75**
$RENDVI_{783.705}$	0.81***	0.81	0.54	0.65***	0.65	0.73	0.60***	0.60	0.78	**0.62*** **	**0.62**	**0.76**
$RENDVI_{865.740}$	**0.98*** **	**0.98**	**0.18**	0.87***	0.87	0.45	0.77***	0.77	0.59	0.44***	0.43	0.93
NIR-Shoulder												
$NSDI_{779.754}$	**0.99*** **	**0.99**	**0.15**	**0.93*** **	**0.93**	**0.32**	**0.86*** **	**0.86**	**0.46**	**0.56*** **	**0.55**	**0.83**
$NSDI_{865.783}$	0.79***	0.79	0.56	0.20***	0.19	1.11	0.10**	0.09	1.18	0.20***	0.19	1.11

Table 7. Summary of the statistics (N, number of observations; R^2, coefficient of determination; Adj. R^2, adjusted coefficient of determination; RMSE, root mean square error) of the linear regression between leaf area index (LAI, $m^2 \cdot m^{-2}$) of 100 iteration step between minimum and maximum range of temporal scale measurements and the spectral vegetation indices (SVIs) calculated from PROSAIL simulated spectra by scenarios considering spatial scale LAI ranges (1t–4t) described in Section 2.3.4. The three best-fitting models are highlighted in bold. Asterisk indicates significance of correlation: *** $p < 0.001$; ** $p < 0.01$; * $p < 0.05$. n.s., not significant (Pearson's correlation test).

SVIs	**Scenario 1s, 2s, 3s, 4s**											
	1s (N=100)			**2s (N=100)**			**3s (N=100)**			**4s (N=100)**		
	R^2	**Adj. R^2**	**RMSE ($m^2 \cdot m^{-2}$)**	**R^2**	**Adj. R^2**	**RMSE ($m^2 \cdot m^{-2}$)**	**R^2**	**Adj. R^2**	**RMSE ($m^2 \cdot m^{-2}$)**	**R^2**	**Adj. R^2**	**RMSE ($m^2 \cdot m^{-2}$)**
VIS-NIR												
$NDVI_{865.665}$	0.86***	0.86	0.27	0.18***	0.17	0.65	0.13***	0.12	0.67	**0.19*** **	**0.18**	**0.65**
MTCI	0.97***	0.97	0.12	**0.85*** **	**0.85**	**0.28**	**0.43*** **	**0.42**	**0.55**	0.11***	0.10	0.68
Red-Edge (RE)												
$RENDVI_{783.740}$	**0.98*** **	**0.98**	**0.09**	**0.82*** **	**0.82**	**0.31**	**0.62*** **	**0.61**	**0.45**	**0.22*** **	**0.21**	**0.64**
$RENDVI_{783.705}$	0.92***	0.92	0.21	0.27***	0.26	0.62	0.24***	0.23	0.63	**0.21*** **	**0.21**	**0.64**
$RENDVI_{865.740}$	**0.99*** **	**0.99**	**0.07**	0.38***	0.38	0.57	0.15***	0.14	0.67	0.10**	0.09	0.68
NIR-Shoulder												
$NSDI_{779.754}$	**0.99*** **	**0.99**	**0.06**	**0.65*** **	**0.65**	**0.42**	**0.33*** **	**0.32**	**0.59**	0.18***	0.17	0.65
$NSDI_{865.783}$	0.80***	0.80	0.32	0.08**	0.07	0.69	0.10**	0.09	0.69	0.05**	0.04	0.70

When only LAI was varying (Scenarios 1t and 1s; Figure 11A,E), a high correlation between LAI and VIS-NIR SVIs ($NDVI_{865.665}$ and MTCI) was observed; however, $NDVI_{865.665}$ (R^2 = 0.73 and R^2 = 0.86 for Scenarios 1t and 1s, respectively) showed a strong saturation effect compared to MTCI (R^2 = 0.98 and R^2 = 0.97 for Scenario 1t and 1s respectively). When it was assumed that LAI and LAD were co-varying, the R^2 values of both $NDVI_{865.665}$ and MTCI decreased, but at different rates. In case of $NDVI_{865.665}$, the R^2 decreased to 0.56 (Scenario 2t) and 0.18 (Scenario 2s), while for MTCI the R^2 dropped to 0.95 (Scenario 2t) and 0.85 (Scenario 2s). Similarly, in Scenario 3t, MTCI performed significantly better (Figure 11G, R^2 = 0.85, Table 6) than $NDVI_{865.665}$ (Figure 11C, R^2 = 0.52, Table 6); however, a noticeable decrease of R^2 was observed in the correspondent spatial scenario for MTCI (R^2 = 0.43, Table 7). Scenario 4t (all PROSAIL input parameters co-varied) resulted in a slight increase—compared to Scenario 3t—in R^2 values between $NDVI_{865.665}$ and LAI (Figure 11D, R^2 = 0.57, RSME = 0.81 $m^2 \cdot m^{-2}$ (Scenario 4t), Table 6; and R^2 = 0.19, RSME = 0.65 $m^2 \cdot m^{-2}$ (Scenario 4s), Table 7). On the other hand, MTCI showed very low R^2 values (Figure 11H, R^2 = 0.39, RMSE = 0.97 $m^2 \cdot m^{-2}$ (Scenario 4t), Table 6; and R^2 = 0.11, RSME = 0.68 $m^2 \cdot m^{-2}$ (Scenario 4s), Table 7).

In Figure 12, scatterplots between RE SVIs ($RENDVI_{783.740}$, $RENDVI_{783.705}$, and $RENDVI_{865.740}$) and LAI are presented. In general, RE SVIs showed a better performance compared to VIS-NIR SVIs for both temporal and spatial scenarios. In Scenarios, 1t and 1s, a high correlation between LAI and RE SVIs ($RENDVI_{783.740}$ and $RENDVI_{865.740}$) was observed (Figure 12A and 12I, $R^2 > 0.9$; RSME < 0.3 $m^2 \cdot m^{-2}$, Table 6 and Table 7). $RENDVI_{783.740}$ showed to be less sensitive to structural traits co-variation and showed a strong correlation (Figure 12C, R^2 = 0.90, RSME = 0.40 $m^2 \cdot m^{-2}$ and R^2 = 0.62, RSME = 0.45 $m^2 \cdot m^{-2}$ for Scenarios 3t and 3s, respectively). $RENDVI_{783.740}$ and $RENDVI_{783.705}$ SVIs showed the highest correlation with LAI in Scenario 4t (Figure 12D,H, R^2 = 0.64, RSME = 0.75 $m^2 \cdot m^{-2}$ and R^2 = 0.62, RSME = 0.76 $m^2 \cdot m^{-2}$, Table 6). However, even if they were among the best performing indices in Scenario 4t, they lost most of their predictive power in Scenario 4s (Figure 12D,H, R^2 = 0.22, RSME = 0.64 and R^2 = 0.21, RSME = 0.64, Table 7).

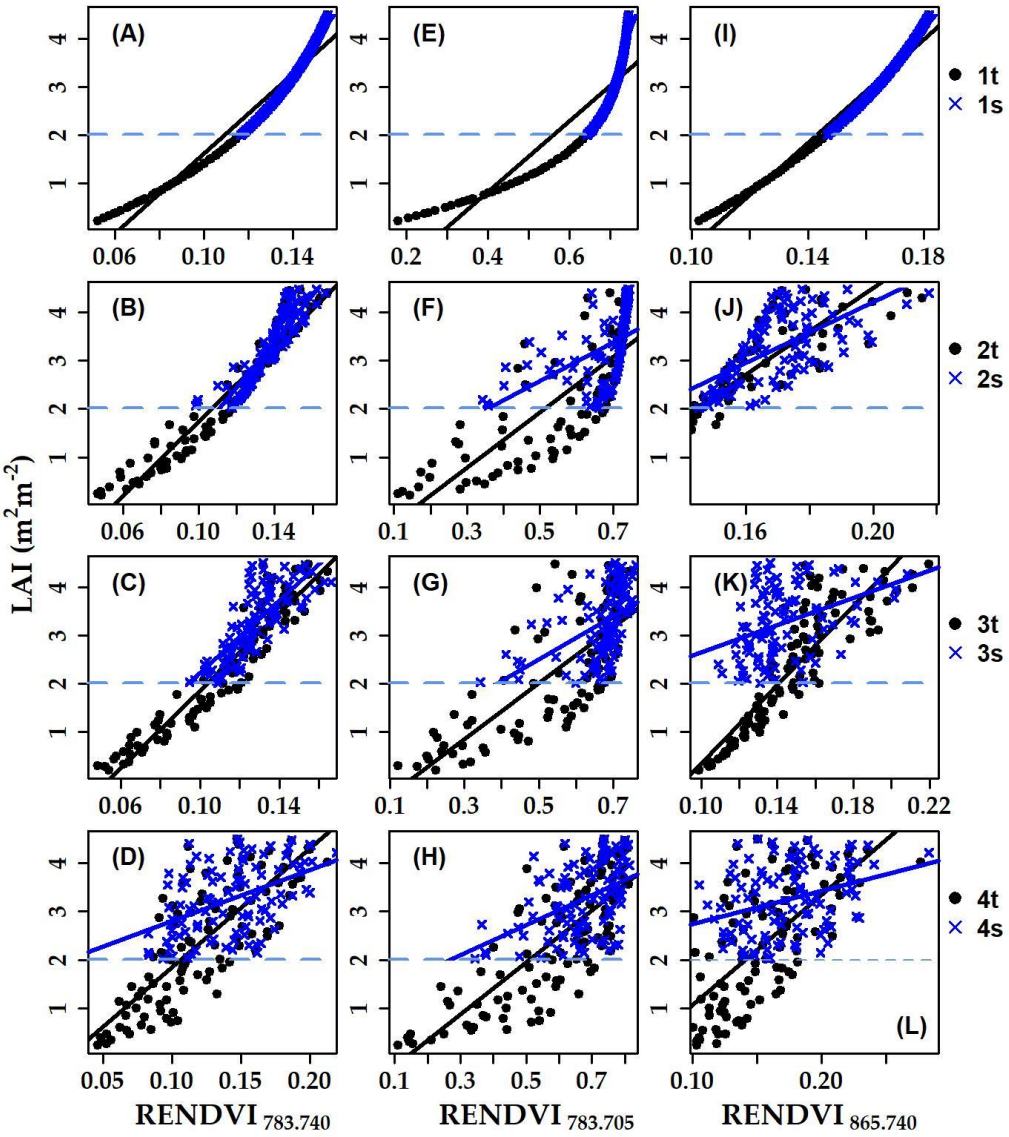

Figure 12. Relationships between RE indices and LAI for all eight scenarios for both temporal ((**A**,**E**,**I**) 1t; (**B**,**F**,**J**) 2t; (**C**,**G**,**K**) 3t; and (**D**,**H**,**L**) 4t) and spatial scale observations ((**A**,**E**,**I**) 1s; (**B**,**F**,**J**) 2s; (**C**,**G**,**K**) 3s; and (**D**,**H**,**L**) 4s). The horizontal dashed line represents the minimum value of LAI when PROSAIL was run using spatial observation LAI ranges as input parameter. In all panels, solid lines represent a linear fit to the data.

Similar to RE-based SVIs, the NIR-shoulder ($NSDI_{779.754}$) showed to mitigate the saturation effect for higher LAI values as observed in Figure 13A–D. In Scenarios 1t and 1s, $NSDI_{779.754}$ exhibited a strong correlation (R^2 = 0.99; Figure 13A) and RMSE < 0.2 $m^2 \cdot m^{-2}$ (Table 6 and Table 7). In Scenarios 2t and 3t, $NSDI_{779.754}$ showed a slight decrease in R^2 value (Figure 13B,C, R^2 = 0.93 and 0.86 for Scenarios 2t and 3t respectively) and a noticeable decrease for Scenarios 2s and 3s was observed (Figure 13B,C, R^2 = 0.65 (Scenario 2s) and R^2 = 0.33 (Scenario 2s)). The $NSDI_{865.783}$ showed an inverse relationship with LAI and showed a low R^2 = 0.2 and 0.05 (Figure 13H) for Scenarios 4t and 4s, respectively.

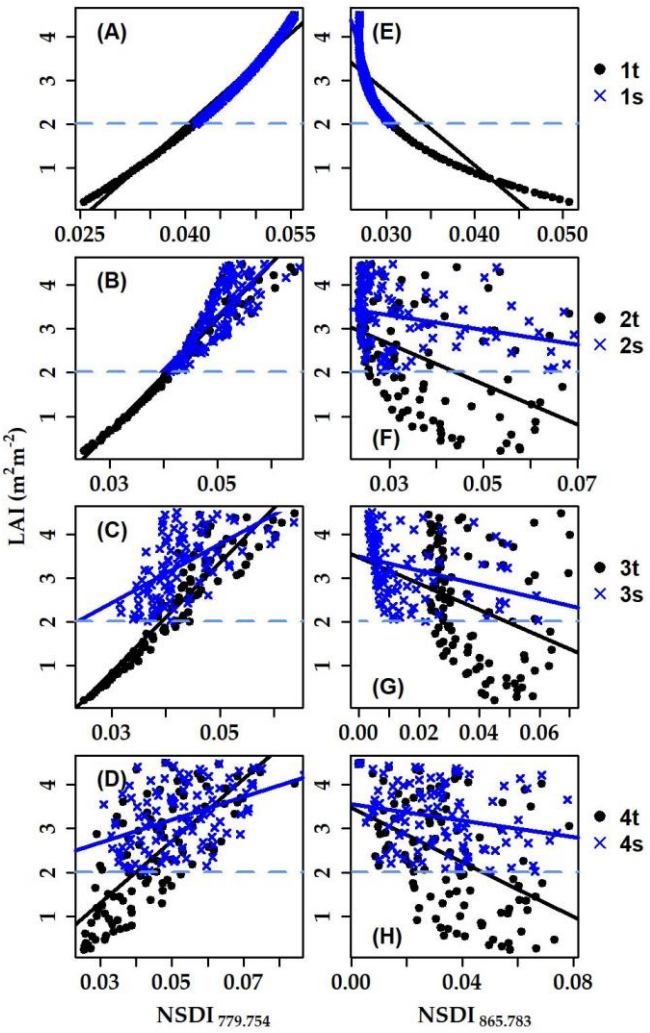

Figure 13. Relationships between NIR-shoulder indices and LAI for all eight scenarios for both temporal ((**A**,**E**) 1t; (**B**,**F**) 2t; (**C**,**G**) 3t; and (**D**,**H**) 4t) and spatial scale observations ((**A**,**E**) 1s; (**B**,**F**) 2s; (**C**,**G**) 3s; and (**D**,**H**) 4s). The horizontal dashed line represents the minimum value of LAI when PROSAIL was run using spatial observation LAI ranges as input parameter. In all panels, solid lines represent a linear fit to the data.

Across the temporal scenarios, $RENDVI_{783.740}$ was among the three best-performing SVIs when two or more traits were co-varying, while at the spatial scale scenarios, $RENDVI_{783.740}$ was always among the three best-performing SVIs (**Table 6** and **Table 7**, respectively). The other SVIs with good performance across temporal and spatial scenarios were $NSDI_{779.75}$ and MTCI.

2.4. Discussion

The grassland spectral response across different spectral regions (VIS, RE and NIR-shoulder) showed to be both site-specific and scale-dependent. The NIR-shoulder slope showed different trends at two sites confirming the results of Vescovo et al. (2012) on the site-specificity of NIR-shoulder indices. Moreover, the NIR-shoulder slope response at the spatial scale appeared to be more complex than the one at the temporal scale and did not strictly follow the typical temporal response at increasing LAI, characterized by an increase of NIR-shoulder slope corresponding to an increase of LAI.

The importance of using hyperspectral and superspectral sensors adopting SVIs with bands in the RE and NIR shoulder spectral region (Delegido et al., 2013; Vescovo et al., 2012) to estimate canopy structure was highlighted in this study for montane temperate grassland ecosystems, and novel band combinations were explored. RTM observations demonstrated that chlorophyll absorption can determine the spectral response well beyond 700 nm, and thus the optimal band combinations to estimate LAI often included far red bands (as shown also in Gitelson et al., 1993; Gitelson & Merzlyak, 1994; Gitelson et al., 2003). Ollinger's paradox (2011) stating that (as chlorophyll absorption range was assumed by this author to be 400–700 nm) "the physiological activity of vegetation is often more strongly related to reflectance at wavelengths that are not used in photosynthesis than to those that are" has been—at least partially—explained during the last years as many studies have been highlighting that photosynthetic pigments' absorption is active in the far-red domain. In our study, the RTM models indicate that chlorophyll absorption can be observed up to 760 nm (Figure 10), while in vivo observations previously indicated 740 nm as an upper limit (Gitelson et al., 1993). For both sites, high R^2 values were detected for band combinations used in water indices. Such result is opening interesting perspectives as these indices can be calculated using both PRISMA and GF-5 satellite data.

The GSA showed that the VIS part of the spectrum is mainly influenced by LAI and Cab, in the RE spectral region reflectance is determined by LAI, Cab, LAD, Cm and, Cbrown. In previous studies, the RE spectral region showed optimal performances in retrieving LAI and canopy chlorophyll content. The RE part of the spectrum is characterized by lower absorption by chlorophyll, but remains sensitive to changes in its content, reducing the saturation effect and enhancing the sensitivity of these SVIs to moderate-high vegetation densities reducing the typical SVI saturation effect (Gitelson & Merzlyak, 1994; Peng et al., 2017). The evident shift of the well-correlated areas towards the lower wavelengths at the AT-Neu site suggests that the performance of some of the RE SVIs is site-specific, probably partly due to different absorption thresholds (Rossi et al., 2019; Vescovo et al., 2012). It is interesting to notice that, despite such shift, the area corresponding to $RENDVI_{783.740}$ was well correlated at both sites, and for both the two years of observations at IT-MBo.

Very contrasting results were achieved at the temporal and spatial scales. At IT-MBo temporal scale strong correlations ($R^2 > 0.8$) were observed between LAI and both traditional RE and NIR-shoulder ($NSDI_{779.754}$) SVIs. Differently from previous studies (Liu et al., 2014; Vescovo et al., 2012; Xie et al., 2018), the performance of such indices at the spatial scale was particularly poor with an $R^2 < 0.1$. Such poor performance could be partially explained by the different LAI ranges at the temporal and spatial scales. At the spatial scale, saturation of some SVIs may be observed above certain LAI values, and this can constrain the ability to retrieve LAI when only full-canopy cover ecosystems are observed (Vescovo & Gianelle, 2008). The poor performance of the SVIs in retrieving LAI at the spatial scale observations is noteworthy and confirming the observations of Dong et al. (2019) on the strong response of canopy reflectance to canopy structural traits. Darvishzadeh et al. (2008b and 2008c) showed that LAI, in heterogeneous grasslands, could be estimated at the spatial scale using the SVIs approach with intermediate accuracy (R^2cv values from 0.49 to 0.69). Atzberger et al. (2013) evaluated the PROSAIL RTM suitability for grasslands and demonstrated that PROSAIL is well suited for LAI estimations. However, in their study, the PROSAIL-generated and the in-situ hyperspectral-derived correlation plots, across the RE and NIR-

shoulder ranges, demonstrated different R^2 patterns between observed and modeled LAI, indicating that RTM parameterization for LAI retrieval is challenging in these spectral domains. The selection of leaf structural and canopy architectural settings is key to achieve an accurate LAI retrieval, and can be complex when heterogeneous canopies are modeled. Following the indications of Darvishzadeh et al. (2008b) on the impact of grassland species composition and canopy architecture on remote sensing models, we hypothesized that the structural heterogeneity of the investigated montane temperate grasslands at the spatial scale might play a crucial role on LAI retrieval. Our results confirm that: (i) the co-variation of all structural traits (such as LAI, LAD, Cm and N, at the spatial scale) could explain the poor performance of most SVIs; and (ii) due the co-variation of both structural and biochemistry traits, no SVI is able to provide reliable LAI spatial estimations. In our study, we used the PROSAIL RTM in forward mode to study the impact of co-variation of PTs on LAI estimation. The PROSAIL results confirmed that trait-covariation resulting from extreme grassland heterogeneity has a strong impact on LAI estimation accuracy. Such findings agree with the observations of Ollinger (2011) on "the difficulty of assessing the relative importance of individual traits that co-vary with a suite of plant properties". For the investigated montane temperate grassland types—characterized by extreme spatial heterogeneity—structural and biochemical intraspecific drivers linked to heterogeneous canopy species composition seem to have a stronger impact on traits estimation than interspecific drivers related to phenology. In other ecosystem types (e.g., arid and Mediterranean grasslands characterized by strong seasonality and extreme phenology dynamics due to changes of ecological factors related to climate and water availability) observations at the temporal scale are more challenging and significant limitations for remote sensing analysis are posed. In such grasslands, senescence can take place at varying rates and periods, increasing the variability of surface biophysical and optical properties (Van der Tol et al., 2020).

$RENDVI_{783.740}$ showed a good performance and it is not very commonly used in the literature, as it was introduced relatively recently. Peng et al. (2017) demonstrated that $RENDVI_{783.740}$ was accurate in estimating canopy chlorophyll in crops with contrasting architectures (maize and soybean). Our results show how $RENDVI_{783.740}$ can be used to monitor grassland LAI. $RENDVI_{783.740}$ demonstrated to be the most insensitive to grassland structural traits co-variation. For this reason, considering the increasing availability of hyperspectral and superspectral sensors such as S-2, GF-5 and PRISMA, more studies are needed to investigate its full potential for monitoring grasslands and other spatially-heterogeneous ecosystems.

The impact of structural PTs on the relationships between SVIs and LAI, although is well known in the literature, should be taken more carefully into account (Darvishzadeh et al., 2008b). Structural traits directly determine the interactions between light and both leaf and canopy elements. In particular, LAD (which is a key canopy trait whose effect has usually not been considered when applying common vegetation SVIs for mapping LAI) showed to have a strong influence for wavelengths > 705 nm. The impact of LAD has been determined for crops (Zou & Mõttus, 2017), but limited research was carried out for grasslands (Vescovo et al., 2012).

Grassland canopy structure heterogeneity may impact the applicability of algorithms to detect vegetation changes due to phenology also at the temporal scale (Balzarolo et al., 2019; Zhao et al., 2012), and this could be the case of temperate grasslands where species composition and coverage is varying due to, e.g., light competition dynamics. As the co-variation of biochemical traits was

included in the PROSAIL RTM simulations, a significant impact on the models accuracy was observed, indicating that both structural and biochemical factors play a major role in models' performance. Biochemical heterogeneity can be determined not only by different vegetation types at the spatial scale, but also by phenological changes. In Mediterranean grasslands, where severe droughts and grassland curing are taking place during the summer months, both biochemical and structural changes are expected (Aldakheel & Danson, 1997; Wen-long et al., 2013).

Using a combination of two NIR bands (both beyond 750 nm), the NIR-shoulder SVI $NSDI_{779.75}$ (calculated from S-3 simulated bands) performed very well at IT-MBo, but not at the AT-Neu. This is probably due to the fact that chlorophyll absorption threshold is different at the two grassland ecosystems, and absorption is still present at 754 nm only in the IT-MBo grassland. This result is defining the green-dependency of NIR shoulder SVIs investigated in Vescovo et al. (2012), which were thought to be related to scattering mechanisms and not chlorophyll absorption. Our study highlighted that this spectral region, which has been poorly investigated in the literature, is largely affected, in addition to chlorophyll until 760 nm, by LAI, LAD, Cbrown and Cw.

The suitability of well-known and widely adopted SVIs for retrieving LAI in grasslands with heterogeneous structure was also questioned in this paper. Many widely-adopted SVIs, e.g., $NDVI_{865.665}$ and MTCI, exhibited a strong correlation with LAI when only a few traits were co-varying, while a much weaker correlation was observed when more traits were co-varied. This agrees with the findings of Peng et al. (2017) and Horler et al. (1983) and advises to carefully evaluate potential uncertainties of satellite-based vegetation products such as LAI, fAPAR in spatially-heterogeneous canopies. In our work, we demonstrated that SVIs such as $RENDVI_{783.740}$ seem to be less influenced by canopy architecture, leaf structure and biochemical traits co-variation, and need further testing.

In this work, some constraints were highlighted on the use of statistical approaches based on SVIs. However, strong limitations of RTM inversion are also implied, and a reliable LAI spatialization in heterogeneous canopies needs to be based, in the future, on more detailed parameterization of the traits which are co-varying with LAI. RTM models show evident intrinsic limitations in their capacity to simulate heterogeneous canopies (Casas et al., 2014; Miraglio et al., 2020), and do not take fully into account some parameters, e.g., the presence of non-photosynthetic material in the canopy (Melendo-Vega et al., 2018). Furthermore, the GSA showed the impact of many different input parameters on LAI retrieval, and only very preliminary information on the spectral impact of some RTM parameters (e.g., canopy brown pigments and anthocyanins) is available in the literature (Casas et al., 2014; Gitelson et al., 2009).

2.5. Conclusions

The potential of Sentinel bands combinations across the RE and the NIR-shoulder spectral region such as $RENDVI_{783.740}$ and $NSDI_{779.754}$ (which are novel or not commonly used in the literature) was highlighted. Such SVIs are worth more attention to ascertain their performance on other canopy types. Moreover, the hyperspectral analysis highlighted the suitability of the spectral regions related to water absorption features for LAI estimations (Ustin et al., 2004; Vescovo & Gianelle, 2008).

The impact of grassland structural and biochemical heterogeneity on LAI estimations was demonstrated to be strong and, for this reason, no reliable field LAI estimation was possible at the spatial scale with any SVI. The results of the empirical approach were confirmed by the simulations performed with the RTM PROSAIL, when both structural and biochemical traits were co-varied. In this context, the uncertainties of satellite-based LAI products (in grassland canopies with either spatially or temporally-heterogeneous structure) need to be carefully taken into account adopting a modeling approach which is minimizing the impact of canopy structural heterogeneity. Despite the fact that the sensitivity analysis demonstrated that LAD impact is quite strong starting from 705 nm, $RENDVI_{783.740}$ proved to be the best performing S-2-based SVIs for monitoring grasslands with heterogeneous structure. Given the fact that our study was carried out in two sites in the Alps, and that spatial observations were carried out only in a limited number of plots, more studies are needed in other grassland ecosystems and/or in other geographic areas to confirm the potential of SVIs using this spectral domain (alongside with the water absorption features) for vegetation monitoring, in the context of the Sentinel, GF-5 and PRISMA missions.

2.6. Supplementary Materials

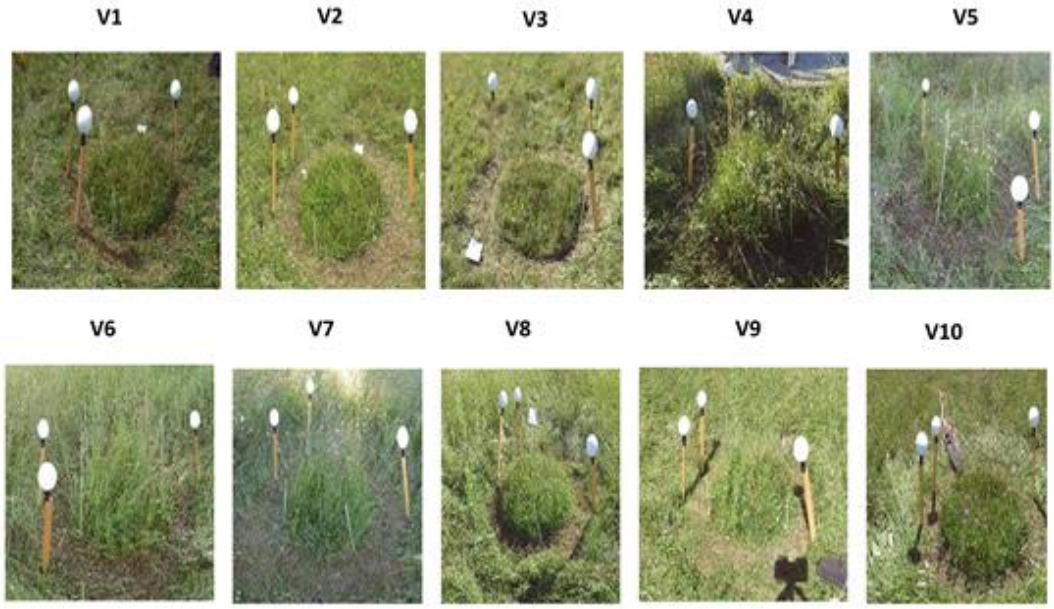

Figure S1. RGB images of the different plots at the IT-MBo study site used for spatial analysis.

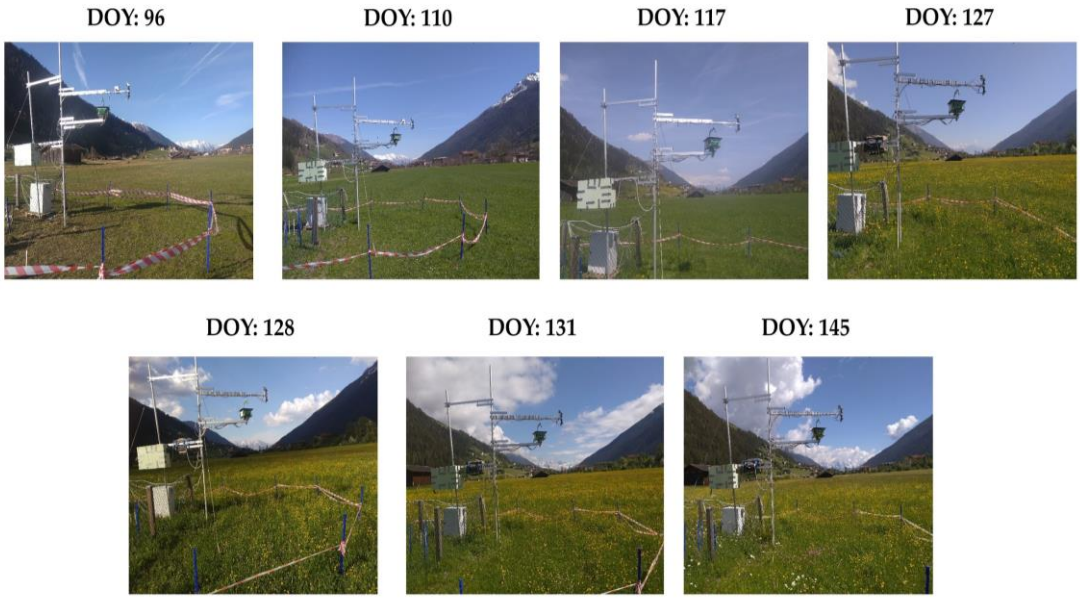

Figure S2. RGB images of the plot at the AT-Neu study site used for temporal analysis.

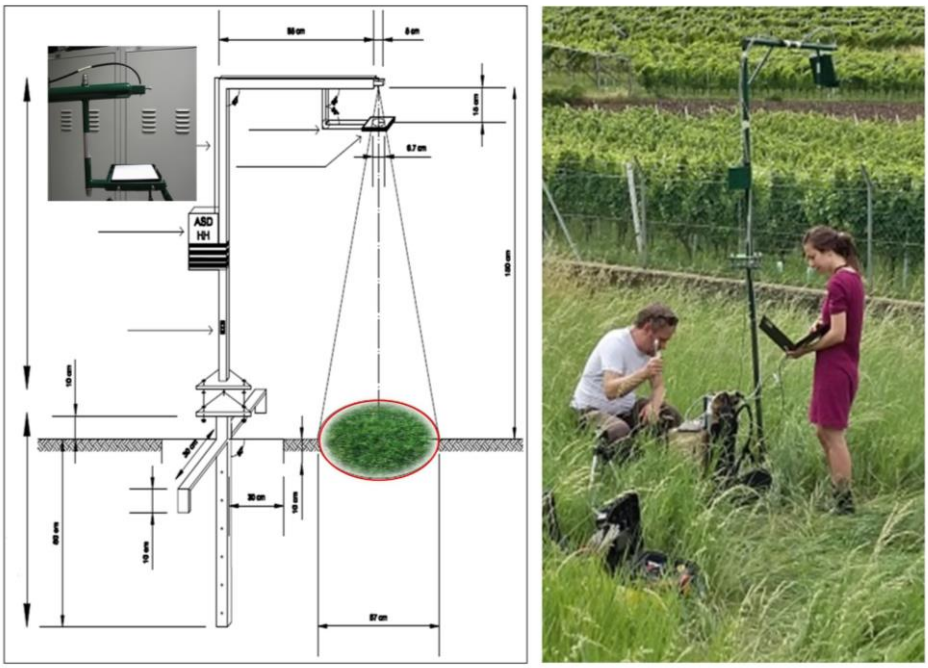

Figure S3. The portable system used for spectral measurements at the IT-MBo for spatial scale observations.

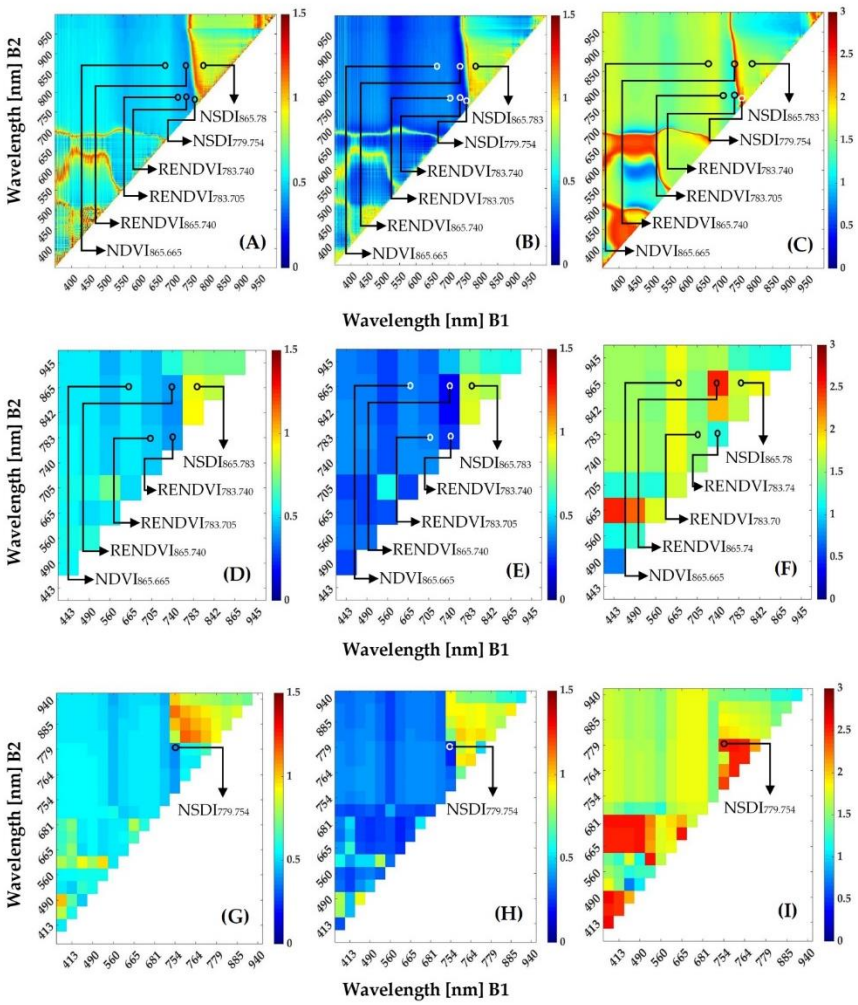

Figure S4. RMSE values based on linear regression between the normalized difference of all two-band combinations and LAI for both study sites (IT-MBo 2013 **(a)**; IT-MBo 2014 **(b)**; and AT-Neu 2018 **(c)**) considering the temporal scale hyperspectral observations. RMSE obtained using: **(a–c)** the hyperspectral data; **(d–f)** S-2 simulated bands; **(g–i)** S-3 simulated bands. Black/white circles refer to the position of the indices in the correlogram and arrows are indicating the name of the respective indices.

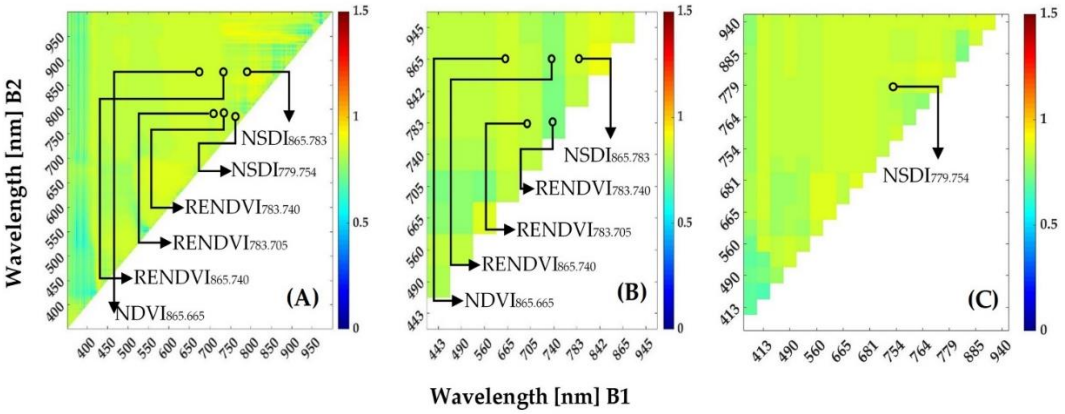

Figure S5. RMSE values based on linear regression between the normalized difference of all two-band combinations and LAI for IT-MBo 2017 considering the spatial scale observations: **(a)** RMSE obtained using the hyperspectral data; and (b,c) RMSE obtained using S-2 and S-3 simulated bands, respectively. Black circles refer to the position of the indices in the correlogram and arrows are indicating the name of the respective indices.

Table S1. Specifications of the multispectral instrument (MSI) and ocean and land color instrument (OLCI) on the S-2 and S-3 satellite system respectively, The NIR-shoulder bands investigated in this study shown in bold.

S-2 Spectral Bands	Central wavelength (nm)	Spectral region	S-3 Spectral Bands	Central wavelength (nm)	Spectral region
B1	443	Blue-1	O1	400	
B2	490	Blue-2	O2	412.5	
B3	560	Green	O3	443	
B4	665	Red	O4	490	
B5	705	RE-1	O5	510	
B6	740	RE-2	O6	560	
B7	**783**	**NIR-shoulder**	O7	620	
B8	842	NIR-shoulder	O8	665	
B8a	**865**	**NIR-shoulder**	O9	673.75	
B9	945	NIR	O10	681	
B10	1375	SWIR-1	O11	709	
B11	1610	SWIR-2	**O12**	**754**	**NIR-shoulder**
B12	2190	SWIR-3	O13	761	
			O14	764.375	
			O15	767.5	
			O16	**779**	**NIR-shoulder**
			O17	865	
			O18	885	
			O19	900	
			O20	940	
			O21	1020	

Table S2. Summary of the statistics (N: Number of observations; R^2: Coefficient of determination; Adj. R^2: adjusted coefficient of determination; RMSE: Root mean square error) of the second order polynomial regression between leaf area index (LAI, $m^2 \cdot m^{-2}$) estimated from fraction of absorbed photosynthetically active radiation (fAPAR) and the spectral vegetation indices (SVIs) calculated from measured spectra for IT-MBo 2013, IT-MBo 2014, AT-Neu 2018 at temporal scale observations and for IT-MBo 2017 at spatial scale observations. The three best-fitting models are highlighted in bold. Asterisk indicates significance of correlation: *** $p < 0.001$; ** $p < 0.01$; * $p < 0.05$; n.s.:not significant (Pearson's correlation test).

SVIs	**Temporal scale observation**									**Spatial scale observations**		
	IT-MBo 2013 (N=8)			**IT-MBo 2014 (N=14)**			**AT-Neu 2018 (N=49)**			**IT-MBo 2017 (N=10)**		
	R^2	**Adj. R^2**	**RMSE ($m^2 \cdot m^{-2}$)**	**R^2**	**Adj. R^2**	**RMSE ($m^2 \cdot m^{-2}$)**	**R^2**	**Adj. R^2**	**RMSE ($m^2 \cdot m^{-2}$)**	**R^2**	**Adj. R^2**	**RMSE ($m^2 \cdot m^{-2}$)**
VIS-NIR												
$NDVI_{865.665}$	0.83*	0.77	0.43	0.97 ***	0.97	0.14	0.71***	0.70	1.37	0.15 $^{n.s}$	-0.10	0.71
MTCI	0.86**	0.80	0.40	0.91***	0.90	0.26	**0.84*** **	**0.83**	**1.03**	0.05$^{n.s}$	-0.23	0.75
Red-edge (RE)												
$RENDVI_{783.740}$	**0.87****	**0.82**	**0.37**	**0.98*****	**0.97**	**0.13**	**0.80*****	**0.79**	**1.15**	0.11$^{n.s}$	-0.15	0.73
$RENDVI_{783.705}$	0.84**	0.78	0.41	0.96***	0.96	0.17	**0.82*****	**0.81**	**1.08**	0.00 $^{n.s}$	-0.28	0.77
$RENDVI_{865.740}$	**0.88****	**0.84**	**0.36**	**0.98*****	**0.97**	**0.14**	0.20**	0.16	2.28	0.16 $^{n.s}$	-0.07	0.70
NIR-shoulder												
$NSDI_{779.754}$	**0.89****	**0.85**	**0.35**	**0.97*****	**0.97**	**0.15**	0.13**	0.09	2.38	0.07 $^{n.s}$	-0.19	0.74
$NSDI_{865.783}$	0.37 $^{n.s}$	0.12	0.83	0.15 $^{n.s}$	0.00	0.82	0.67***	0.66	1.47	0.39$^{n.s}$	0.22	0.60

Chapter 3

Potential and Limitations of Grasslands α-Diversity Prediction Using Fine-Scale Hyperspectral Imagery

Hafiz Ali Imran [1,2,*], Damiano Gianelle [1], Michele Scotton [3], Duccio Rocchini [4,5], Michele Dalponte [1], Stefano Macolino [3], Karolina Sakowska [6,7], Cristina Pornaro [3] and Loris Vescovo [1]

[1] Sustainable Ecosystems and Bioresources Department, Research and Innovation Centre, Fondazione Edmund Mach, Via E. Mach 1, 38098 San Michele all'Adige, TN, Italy; damiano.gianelle@fmach.it (D.G.); michele.dalponte@fmach.it (M.D.); loris.vescovo@fmach.it (L.V.)

[2] Department of Civil, Environmental and Mechanical Engineering, University of Trento, Via Mesiano 77, 38123 Trento, TN, Italy

[3] Department of Agronomy, Food, Natural Resources, Animals, and Environment (DAFNAE), Viale dell'Università 16, 35020 Legnaro, PD, Italy; michele.scotton@unipd.it (M.S.); stefano.macolino@unipd.it (S.M.); cristina.pornaro@unipd.it (C.P.)

[4] BIOME Lab, Department of Biological, Geological and Environmental Sciences, Alma Mater Studiorum, University of Bologna, Via Irnerio 42, 40126 Bologna, BO, Italy; duccio.rocchini@unibo.it (D.R.)

[5] Department of Spatial Sciences, Faculty of Environmental Sciences, Czech University of Life Sciences Prague, Kamýcka 129, 16500 Prague-Suchdol, Czech Republic

[6] Institute of BioEconomy, National Research Council (IBE-CNR), Via Biasi 75, 38098 San Michele all'Adige, TN, Italy; karolina.sakowska@ibe.cnr.it (K.S.)

[7] Foxlab Joint CNR-FEM Initiative, Via E. Mach 1, 38098 San Michele all'Adige, TN, Italy

***** Correspondence: hafizali.imran@unitn.it

Abstract

Plant biodiversity is an important feature of grassland ecosystems, as it is related to the provision of many ecosystem services crucial for the human economy and well-being. Given the importance of grasslands, research has been carried out in recent years on the potential to monitor them with novel remote sensing techniques. In this study, the optical diversity (also called spectral diversity) approach was adopted to check the potential of using high-resolution hyperspectral images to estimate α-diversity in grassland ecosystems. In 2018 and 2019, grassland species composition was surveyed, and canopy hyperspectral data were acquired at two grassland sites: Monte Bondone (IT-MBo; species-rich semi-natural grasslands) and an experimental farm of the University of Padova, Legnaro, Padua, Italy (IT-PD; artificially established grassland plots with a species-poor mixture). The relationship between biodiversity (species richness, Shannon's, species evenness, and Simpson's indices) and optical diversity metrics (coefficient of variation-CV and standard deviation-SD) was not consistent across the investigated grassland plant communities. Species richness could be estimated by optical diversity metrics with an R = 0.87 at the IT-PD species-poor site. In the more complex and species-rich grasslands at IT-MBo, the estimation of biodiversity indices was more difficult and the optical diversity metrics failed to estimate biodiversity as accurately as in IT-PD probably due to the higher number of species and the strong canopy spatial heterogeneity. Therefore, the results of the study confirmed the ability of spectral proxies to detect grassland α-diversity in man-made grassland ecosystems but highlighted the limitations of the spectral diversity approach to estimate biodiversity when natural grasslands are observed. Nevertheless, at IT-MBo, the optical diversity metric SD calculated from post-processed hyperspectral images and transformed spectra showed, in the red part of the spectrum, a significant

correlation (up to R = 0.56, p = 0.004) with biodiversity indices. Spatial resampling highlighted that for the IT-PD sward the optimal optical pixel size was 1 cm, while for the IT-MBo natural grassland it was 1 mm. The random pixel extraction did not improve the performance of the optical diversity metrics at both study sites. Further research is needed to fully understand the links between α-diversity and spectral and biochemical heterogeneity in complex heterogeneous ecosystems, and to assess whether the optical diversity approach can be adopted at the spatial scale to detect β-diversity. Such insights will provide more robust information on the mechanisms linking grassland diversity and optical heterogeneity.

Keywords: biodiversity indices; coefficient of variation (CV); man-made grasslands; natural grasslands; optical diversity; standard deviation (SD)

3.1. Introduction

Biodiversity and ecosystem functions are crucial in many different ways and provide several ecosystem services related to human well-being (Cavender-Bares et al., 2020; Naeem et al., 2016). A minimum level of biodiversity is needed for sustainable preservation to maintain ecosystem functions (Laurila-Pant et al., 2015). However, in the last decades, changes in human activities have modified the landscape in many different regions of the planet. In the Alps, for example, such modifications have accelerated biodiversity loss at unprecedented rates as in the last decades modifications in society, tourism, and agricultural production have led to substantial land use changes and a loss of landscape diversity, particularly for grassland ecosystems (Chemini and Rizzoli, 2014). In this context, to address the current decline in biodiversity, novel and efficient methods and tools are required to monitor biodiversity across spatial scales from the leaf level to the canopy, ecosystem, and global scales (Gamon et al., 2020; Schrodt et al., 2020; Schweiger, 2020).

In recent years, improved detector technology and novel sensors providing fine-scale hyperspectral imagery have enabled new methods to monitor ecosystem biodiversity based on varying plant optical properties of different species or functional groups (Bolch et al., 2020; Gamon et al., 2020; Ustin et al., 2020). Novel imaging sensors for *in-situ* observations that are now commercially available (Behmann et al., 2018) have spectral and spatial resolution sufficient to identify plant species from their leaf spectra (Pornaro et al., 2019; Wang et al., 2020). Such sensors can also be used to investigate the links between optical diversity and plant diversity across a range of different grassland ecosystems, from artificial to natural. Optical diversity (also called spectral diversity) refers to the "variation in remote sensing measurements, typically spectral reflectance, across sets of pixels and has been proposed to relate to conventional metrics of biodiversity" (Wang & Gamon, 2018). Different plant species respond in their own way to incoming solar radiation according to their pigment, water, and biochemical content, as well as leaf and canopy structure. Thus, the variability in the remotely sensed spectra might enable detection of plant species diversity (Wang & Gamon, 2018; Peng et al., 2019; Rocchini et al., 2010; Schweiger et al., 2018; Serbin and Townsend, 2020). This concept represents the basis of the spectral variability hypothesis (SVH): as the number of plant species increases for a given area, the spectral diversity observed from that area should also increase (Heumann et al., 2015; Rocchini et al., 2004). In the literature, there are different methods developed by the remote sensing community to quantify the spectral diversity and

to relate it to α-diversity. α-diversity is commonly measured by species richness (number of species in the sampling area) or can be quantified with other heterogeneity measures, such as e.g., the Shannon's index (Shannon, 1948), Simpson's index (Simpson, 1949), and species evenness (Pielou, 1966), which measure the even abundance between species and dominance of the species.

Several studies have tested the SVH in various ecosystems and at various spatial scales (grasslands: (Aneece et al., 2017; Möckel, 2016; Wang et al., 2016; Wang & Gamon, 2018); forests: (Schäfer et al., 2016; Torresani et al., 2019); wetlands: (Heumann et al., 2015) and reported that spectral diversity metrics can be used as a proxy of α-diversity. Spectral diversity metrics include the coefficient of variation (CV) (Gholizadeh et al., 2018; Gholizadeh et al., 2019; Wang & Gamon, 2018) and the standard deviation (SD) across the wavelengths (Aneece et al., 2017), the mean distance of pixels from the spectral centroid (Rocchini et al., 2010), the convex hull area of pixels in spectral feature space (Gholizadeh et al., 2018) and the spectral variance (Laliberté et al., 2020). Schweiger et al. (2018) used spectral diversity based on the dissimilarity of 1000 randomly extracted vegetation pixels per plant community from high-resolution proximal data to test the relationship between spectral diversity and productivity. Many studies, however, were mostly focused on artificially established (sown) plant communities with relatively low diversity, which are very different in terms of structure from natural plant communities. Man-made ecosystems cannot be considered as fully representative of the complexity of natural field ecological conditions (Schweiger et al., 2018). A review of the results achieved in previous studies with respect to herbaceous canopies and grassland types is summarized in Table 8. These studies reported a positive correlation (up to $R^2 = 0.58$) between spectral diversity metrics and α-diversity in grassland ecosystems (Aneece et al., 2017; Peng et al., 2019; Wang & Gamon, 2018). Aneece et al. (2017) related spectral diversity (expressed as SD) with species diversity (Shannon–Weiner index) and evaluated correlations ($R^2 = 0.43$) across different spectral regions from visible (VIS) and near-infrared (NIR). In another study, Wang et al. (2018) used the average CV of spectral reflectance calculated over the 430–925 nm wavelength as an indicator of optical diversity and then compared the CV values obtained at different spatial scales ranging from 1 mm to 1 m with α-diversity metrics. Peng et al. (2019) investigated a natural temperate grassland (with a maximum species richness of 12 in a 0.8 m diameter plot) and reported that the maximum R^2 value of the correlation between optical diversity and α-diversity was 0.40.

Table 8. Summary of some of the previous studies using the optical diversity approach to estimate biodiversity.

Study	Type of grasslands	Range of species per Plot	Plot size	Sensor used	Optical diversity metrics	Biodiversity indices	Correlation between optical diversity and biodiversity metrics
Aneece et al., 2017	Abandoned areas, early successional stages with exotic species (US)	1 to 5	1 m^2 (Footprint diameter 1.15 m)	ASD Field spectrometer	SD[1] of reflectance (average across590 to 674 nm)	Shannon's	R^2 (0.37)
					SD of CR[1] (average across590 to 674 nm)	Shannon's	R^2 (0.43)
					SDof FD[1] of original reflectance (average across925 to 1025 nm)	Shannon's	R^2 (0.43)
Wang et al., 2018a	Artificial grassland with native species planted in Prairie Ecosystem (US)	1 to 16	1 m^2	Imaging spectrometer (mounted on a tram)	CV[1] (average across430 to 925nm)	species richness	R^2 (0.47)
						Shannon's	R^2 (0.43)
						Simpson's	R^2 (0.58)
						species evenness	R^2 (0.42)
						PSV[1]	R^2 (0.00)
						PSE[1]	R^2 (0.27)
Peng et al., 2017	Natural temperate grasslands (China)	1 to 12	0.5 m^2 (Footprint diameter 0.8 m)	ASD FieldSpec2 spectrometer	SVIs[1](FD_{583})	species richness	R^2 (0.40)
Present study	Experimental golf turf grassland plots	1 to 9	0.0625 m^2 0.25 m^2	Imaging spectrometer (mounted on a tripod)	CV, SD (average at different spectral regions, across the spectrum, and at each spectral band)	species richness	In discussion
Present study	Subalpine grasslands	2 to 17	0.0625 m^2	Imaging spectrometer (mounted on a tripod)	CV, SD (average at different spectral regions, across the spectrum, and at each spectral band)	species richness, Shannon's, species evenness, Simpson's	In discussion

[1] SD: standard deviation, CR: continuum removed, FD: first derivative, CV: coefficient of variation, PSV: phylogenetic species variability, PSE: phylogenetic species evenness, SVIs: spectral vegetation indices.

The relationship between spectral diversity and biodiversity demonstrated to be not consistent across plant communities. For example, Lucas and Carter (2008) investigated the link between spectral diversity metrics (expressed in terms of CV) and species richness and revealed contradictory relationships between spectral α-diversity and species richness in meadows of Horn Island (Mississippi, USA). The accuracy of the species diversity estimation varied with the spectral data acquisition and with the level of complexity of the community. Spatially heterogeneous canopy structure has a greater possibility to create heterogeneous shadow patterns. Heterogeneous canopy shadow patterns modify optical diversity patterns, which are influenced not only by plant diversity but also by shadow rates. Additionally, phenology status shifts among different species may lead to major structural differences in terms of different rates and different spatial distribution of non-photosynthetic elements (e.g., flowers, dead material, Hall et al., 2012; Vrieling et al., 2018). This heterogeneity may create a further shift between optical diversity metrics and the measured biodiversity metrics; as a result, the accuracy of the estimation of biodiversity metrics can be reduced (Peng et al., 2019).

Uncertainties in the remote estimation of canopy biodiversity also exists because species richness is an aggregated measure of diversity that does not take explicitly into account either canopy structure or composition, the two main vegetation properties that are more easily captured by remotely sensed data (Nagendra, 2001). With the advancement of proximal sensors technology and the use of very-high spatial resolution (up to 1 mm) imagery (Behmann et al., 2018), new opportunities arise, although some new challenges need to be considered. Ideally, the pixel size should be smaller than the sampling unit, especially when estimating α-diversity by using the spectral diversity approach (Rocchini et al., 2016). However, at the same time, a few authors highlighted the drawback of very-high spatial resolution imagery and state that a finer scale increases the spectral variability caused by canopy non-photosynthetic elements (flowers and dead material), shadowed pixels, and overexposed pixels, which often hamper the separability of the individual plant species in pixel-based studies (Gholizadeh et al., 2018; Lopatin et al., 2017; Wang & Gamon, 2018). Similarly, Nagendra (2001) stressed the downside of very-high spatial resolution, which can be excessive in respect to the objects being represented, contributing to the variability in optical patterns, and a reduction in the accuracy in classification studies (Rocchini, 2007). In the optical diversity context, Rocchini et al. (2016) stated that when very-high spatial resolution is used to monitor the species diversity, the shadowed pixels may create a higher spatial heterogeneity among the spectra, which leads to noise rather than enhancing the information content.

The aforementioned studies on grasslands (Aneece et al., 2017; Peng et al., 2019; Wang & Gamon, 2018) were focused on relatively low-diversity or artificially established plant communities which are very different in terms of structure and complexity from the natural grassland plant communities. The studies on grassland biodiversity are often carried out at small scale using a "within-site" approach to keep environmental conditions among treatments as much constant as possible (Roscher et al., 2005) and are often based on manipulation of species richness. In this regard, Grace et al. (2007) highlighted the limits of manipulation experiments in ecological studies and the need for more analyses focused on mature natural ecosystems.

The present study examined the possibility to use variability in vegetation optical properties to assess species diversity in grassland ecosystems using very high spatial resolution hyperspectral data. Spectral diversity has been quantified through the analysis of the CV (Wang et al., 2016;

Wang & Gamon, 2018; Wang et al., 2018a) and the SD (Aneece et al., 2017; Blanco-Sacristán et al., 2019; Peng et al., 2019) of the original and transformed hyperspectral reflectance. We conducted two sets of experiments in two different grasslands with different origin and different diversity levels. The first ecosystem was a turfgrass established artificially by seeding a limited number of species (1–9 species in 2 × 2 m plots), while the second was a subalpine semi-natural grassland characterized by high diversity (up to 17 species in a 0.25 × 0.25 m plot).

Specific field campaigns were carried out to test the following research questions:

(1) Is there a relationship between plant α-diversity and spectral diversity proxies obtained using high spatial and spectral resolution imagery? Can this relationship be observed both in the species-poor turf grassland and in the subalpine semi-natural grassland characterized by high biodiversity and heterogeneous canopy structure?

(2) What is the impact of processing methods, such as filtering and spectral transformations, on the correlations between grassland spectral diversity and biodiversity metrics?

(3) What is the impact of the spatial sampling scale and random pixel extraction on the relationship between grassland optical diversity and biodiversity metrics?

3.2. Materials and Methods

3.2.1. Study Area

The dataset used in this study was collected at two grassland sites characterized by different structure, species composition, and origin (Supplementary Materials, Figure S6). The first site was a turf grassland (Figure 14) located on the Experimental Farm of the University of Padova, in Legnaro, Italy (45°21′ N, 11°58′ E; 6 m a.s.al., IT-PD), where plots of varying species richness (ranging from 1 to 9) were established in September 2018 by seeding. The established plots were arranged in a square (2 × 2 m) design and were managed by removing weeds and mowed with a rotary mower machine at approximately 4.7 mm every other week. Subplots with dimensions of 0.25 × 0.25 m and 0.5 × 0.5 m were chosen within the 2 × 2 m square plots for the spectral and biodiversity analysis. The species composition of the investigated plots at IT-PD is summarized in Table S3 in Supplementary Materials.

The second site was a permanent semi-natural grassland (Figure 14) situated in the Italian subalpine vegetation belt at Viote del Monte Bondone, Trentino province, Italy (46°00′ N, 11°01′ E; 1480–1550 m a.s.al., IT-MBo). The grassland area lies on a plateau, and it is managed extensively as a meadow with low mineral fertilization. It is cut once a year around mid-July at the green biomass peak time, and it is characterized by very high plant diversity (Donita et al., 2003). Several different vegetation types can be found in the area with extremely varying canopy structure and biomass (Sakowska et al., 2019; Imran et al., 2020). The *Sieverso-Nardetum strictae* association covers a high portion of the plateau characterized by short canopies. The *Scorzonero Aristatae-Agrostidetum tenuis* association canopy is generally taller, and it grows on calcareous soils. The latter association includes more productive species, and it can be found in the most fertile and well-exposed areas of the plateau (Sakowska et al., 2019). The species composition of the 25 investigated plots (0.25 × 0.25 m) of the IT-MBo plateau is summarized in Table S4 in Supplementary Materials.

Figure 14. (**A**) Location of the sample plots in both study areas (IT-PD and IT-MBo). (**B**) The IT-PD plots (*n* = 9) are located at the experimental farm of the University of Padova (Legnaro, Italy). (**C**) IT-MBo plots (*n* = 25) are located in the natural grassland ecosystem in the Italian Alps (Monte Bondone, Trento, Italy). RGB images of selected plots of both study sites are shown on the right.

The methodological flowchart of the study is shown in Figure 15. In the following sections, each step is described in detail.

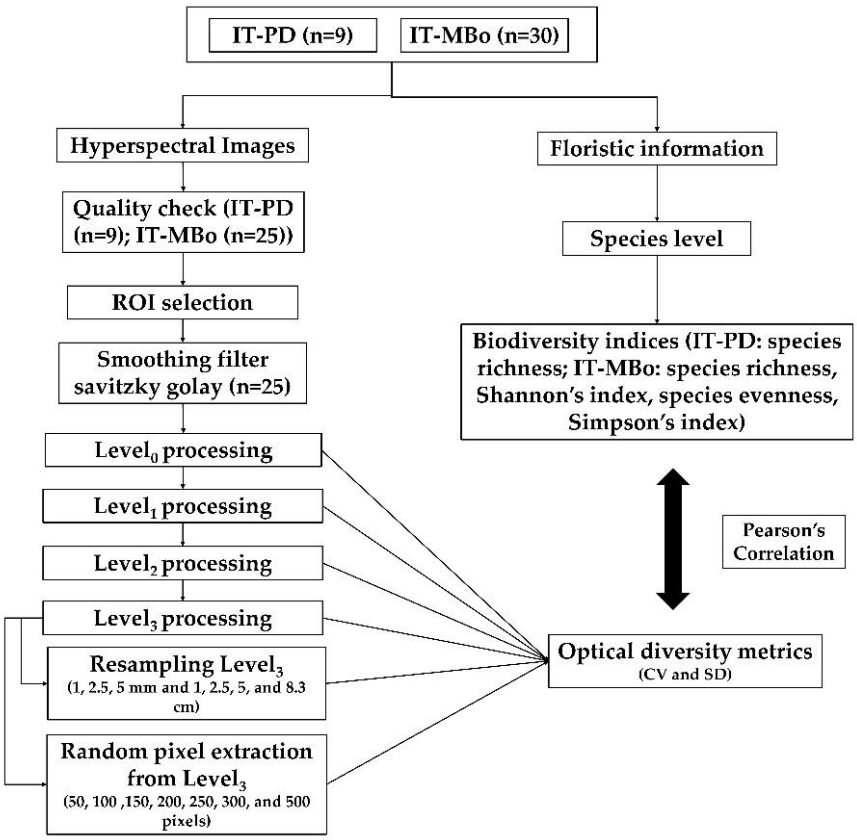

Figure 15. Flowchart representing the data processing approach used in this study. See **Section 2.4** for details on the different levels of processing.

3.2.2. Biodiversity

To collect the floristic information, vegetation surveys were carried out by a trained person within the study areas. At the IT-PD site, the species number was counted after identification of all species within the ROI (0.25 × 0.25 m and 0.5 × 0.5 m). At the IT-MBo site, the species composition was determined by listing all plant species within the ROI (0.25 × 0.25 m) and visually estimating their percent cover (Kent & Coker, 1992). Species percent cover information was used to calculate the following biodiversity indices: species richness (S), Shannon's index (H'), Simpson's index (D), and species evenness (J, calculated as Pielou's index). The details regarding the biodiversity indices are reported in Table 9. All biodiversity indices were calculated using the 'vegan' R package (Oksanen et al., 2020).

Table 9. Biodiversity metrics used in this study. p_i is the proportion of the species i.

Biodiversity Metrics	Formula	Reference
species richness (S)	$S = \text{number of species}$	Colwell, 2009)
Shannon's index (H')	$H' = -\sum_{i=1}^{S} p_i \ln(p_i)$	Shannon, 1948
Species evenness (J)	$J = H'/\ln(S)$	Pielou, 1966
Simpson's index (D)	$D = 1 - \sum_{i=1}^{S} p_i^2$	Simpson, 1949

3.2.3. Spectral Data Acquisition

At the IT-PD site, the hyperspectral data of the nine plots were collected in the summer of 2019 by means of a SPECIM IQ hyperspectral camera (SPECIM Ltd., Finland). The spatial sampling of the camera is 512 pixels per line and the spectral resolution is 7 nm, with 204 bands across the VIS (397 nm–700 nm) and NIR (700 nm–1003 nm) spectral range. The hyperspectral camera was mounted on a tripod and two nadir images were collected at approximately 1 and 2 m from the ground (with an image footprint of approximately 0.55 × 0.55 m and 1.1 × 1.1 m, respectively). The images were acquired using the simultaneous mode (the white reference panel was recorded simultaneously with the targeted vegetation). For both study sites, the spectral data were acquired between 11:00 and 14:00 local time under clear sky conditions. To record the images, an integration time of 1 ms was used, which provided a weak signal, but ensured non-saturated images. The SPECIM IQ did not allow the acquisition of non-saturated images with higher integration time under clear sky conditions. The ROIs (0.25 × 0.25 m and 0.5 × 0.5 m) of the IT-PD images were extracted and used for post-processing and spectral diversity metrics calculations. The distance from the canopy was approximately 1 m for IT-PD and 0.7 m for IT-MBo site. Although the distance between the canopy and the camera was kept as constant as possible, the number of pixels within the ROIs was not exactly the same due to slight variation in canopy height. In the IT-PD plots, the average number of pixels per ROI was 64,260 pixels, with an average pixel size of 1 mm (pixel size: min, 0.95 mm and max, 1.02 mm) and 10,8240 pixels with

an average pixel size of 1.5 mm (pixel size: min. 1.48 mm and max. 1.56 mm) within the ROIs of 0.25 × 0.25 m and 0.5 × 0.5 m, respectively.

At the IT-MBo site, we selected 30 randomly distributed plots with species richness ranging from 2 to 17. In the summer of 2018, at the biomass peak time, we collected canopy level spectral data using the same SPECIM IQ camera. The canopy height at IT-MBo was not consistent between the plots (varied from 0.3 to 1.2 m); therefore, the hyperspectral images were collected approximately 0.7 m from the canopy level to capture a squared footprint of approximately 0.55 × 0.55 m. A 0.25 × 0.25 m frame was placed within each image footprint to define the ROIs used for post-processing and spectral diversity metrics calculations. The average number of pixels within the IT-MBo ROIs was 84,100 with an average pixel size of 0.9 mm (pixel size: min, 0.70 mm and max, 1.48 mm). All the 30 plots images were visually evaluated to remove any blurred (because of moving leaves due to windy conditions) and out of focus images. Finally, 5 plots were discarded after the quality check of the hyperspectral images and 25 plots were kept for further analysis.

3.2.4. Pre- and Post-Processing

ROIs were extracted from the image using the ENVI (version 4.8) software. For further processing, we used the open-source statistical software R (R Core Team, 2019). The pre- and post-processing of the hyperspectral data were categorized into four processing levels. In $Level_0$, corresponding to processing of the raw spectral data, the bands 397–411 and 930–1003 nm were removed to avoid the use of noisy data which were detected in these spectral regions (Behmann et al., 2018). To further reduce the noise in the spectral signature, a Savitzky–Golay smoothing filter (Savitzky & Golay, 1964) was applied using a 25-band window width.

The brightness of the spectra may be affected by heterogeneous illumination, leaf volume, or subpixel shade (Feilhauer et al., 2010). For $Level_1$ processing, we applied brightness normalization (Feilhauer et al., 2010) to all the images and then calculated the optical diversity metrics from the brightness normalized images.

For $Level_2$ processing, we applied specific filters to remove bright pixels from the images, alongside pixels containing flowers, shadows, and soil background, as they are not linked to plant biodiversity. We used the red band (680 nm) to remove shadowed pixels (Han et al., 2018), and the thresholds were defined by visual interpretation. Pixels with red band reflectance below the first quartile were found to be suitable for obtaining a reliable separation between shaded and sunlit pixels for the investigated plots. To filter the flower pixels, we used the red-green normalized difference vegetation index (NDVIrg) based on the red and green bands (640 and 551 nm, respectively). Pixels with an NDVIrg value higher or equal to the visually selected threshold of 0.1 were excluded (Wan et al., 2018). Furthermore, to remove the bright pixels in the images due to hot spots at the leaf level, we used the NIR band (865 nm) and selected a threshold value (>third quartile) to filter out the over-illuminated pixels. To remove dead leaves pixels, we used a normalized difference vegetation index (NDVI) mask (≤0.7) for all of the images. For $Level_2$ processing, about 46% for IT-PD and 54% for IT-MBo of the pixels from the total number of pixels within the ROIs were classified as shadows, flowers, dead leaves, and bright pixels and were filtered out.

To normalize the spectral features and reduce noise, spectral vegetation indices are commonly used to remotely evaluate vegetation covers both quantitatively and qualitatively (Fang et al., 2016). In some cases, transformed (continuum-removed—CR) spectra is used to normalize reflectance data (Aneece et al., 2017). To further improve the quality of the images for $Level_3$ processing, we, therefore, calculated the CR spectra from the $Level_2$-processed data.

3.2.5. Calculation of Optical Diversity Metrics

As an indicator of the optical diversity of each plot, we used two spectral diversity metrics: the CV (i.e., ratio of the standard deviation to the mean, (Blanco-Sacristán et al., 2019; Wang & Gamon, 2018) and the SD calculated as the average across the spectrum (Wang & Gamon, 2018) from the $Level_0$-processed data using the following equations:

$$\mathrm{CV_{image}} = \frac{\sum_{\lambda=411}^{930} \left(\frac{\mathrm{std}\ (\rho_\lambda)}{\mathrm{mean}\ (\rho_\lambda)} \right)}{\mathrm{number\ of\ bands}} \quad (4)$$

where ρλ represents the reflectance value at wavelength λ and std (ρλ) and mean (ρλ) indicate the standard deviation and mean value of the reflectance at wavelength λ, respectively. The average CV and SD were also calculated considering different spectral regions (408–499 nm, 500–589 nm, 590–674 nm, 675–754 nm, and 755–930 nm) as in Aneece et al. (2017) from the $Level_0$-processed data. We also calculated the CV and SD for each spectral band using Equations (3) and (4) from the original images and for each of the post-processing levels ($Level_0$ processing, $Level_1$ processing, $Level_2$ processing, and $Level_3$ processing) described in **Section 2.4**:

$$CV_{image\ (\lambda)} = \frac{std\ (\rho_\lambda)}{mean\ (\rho_\lambda)} \quad (5)$$

$$SD_{image\ (\lambda)} = std\ (\rho_\lambda) \quad (6)$$

where ρλ represents the reflectance value at the wavelength λ and std (ρλ) and mean (ρλ) indicate the standard deviation and mean value of the reflectance at the wavelength λ, respectively. The CV and SD calculated from the fully transformed $Level_3$ reflectance (brightness normalized, filtered, and CR) are shown in Figure 16 (IT-PD CV: E and IT-PD SD: F) and Figure 17 (IT-MBo CV: E and IT-MBo SD: F).

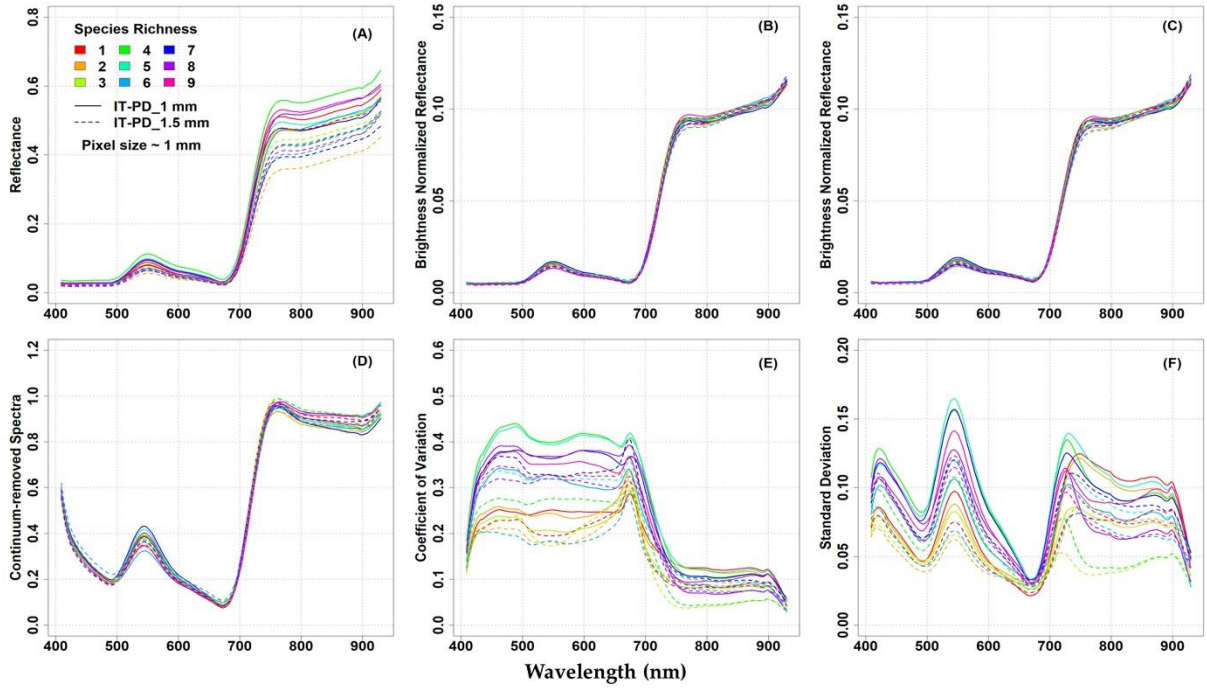

Figure 16. Mean reflectance spectra of nine plots located at the IT-PD site: (**A**) Original reflectance; (**B**) Brightness normalized reflectance; (**C**) Brightness normalized and filtered reflectance; (**D**) Brightness normalized, filtered, and continuum removed spectra; (**E**) Coefficient of variation; (**F**) Standard deviation. In panels (A–F), a solid line represents the mean reflectance obtained from 0.25 × 0.25 m ROIs with a pixel size of 1 mm and a dashed line represents reflectance from 0.25 × 0.25 m ROIs with a pixel size of 1.5 mm.

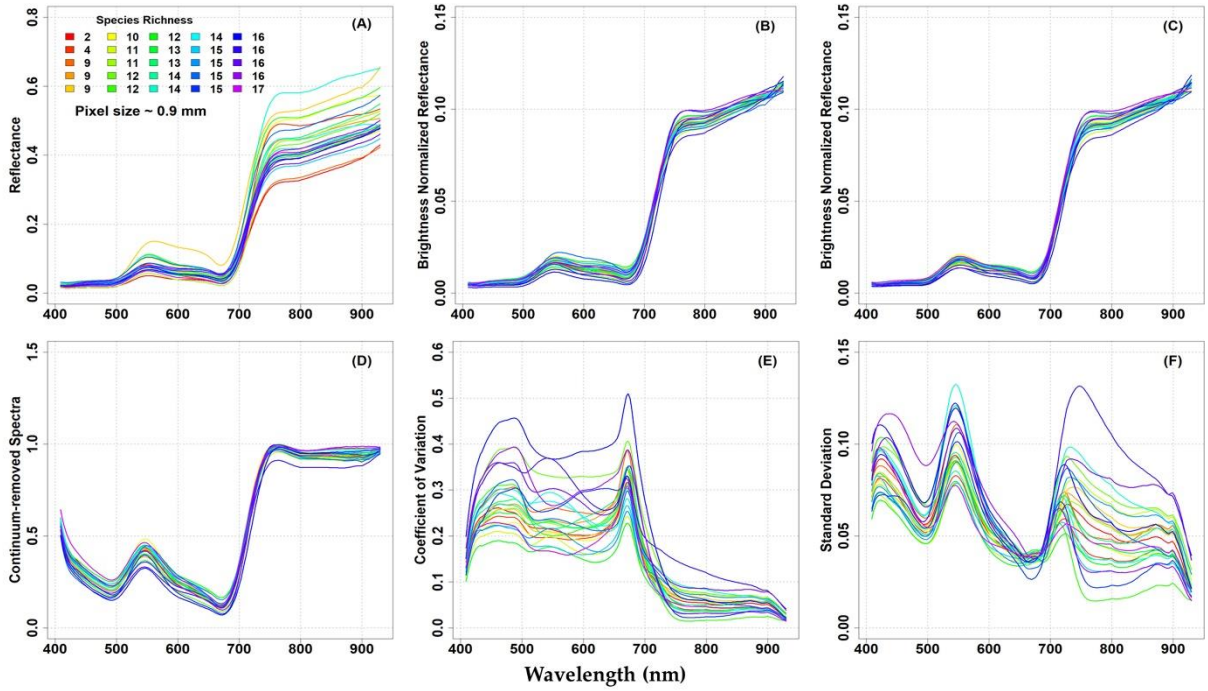

Figure 17. Mean reflectance spectra of 25 plots located at the IT-MBo site obtained from 0.25 × 0.25 m ROIs: (**A**) Original reflectance; (**B**) Brightness normalized reflectance; (**C**) Brightness normalized and filtered reflectance; (**D**) Brightness normalized, filtered, and continuum removed spectra; (**E**) Coefficient of variation; (**F**) Standard deviation.

The effects of pixel resolution and random pixel extraction on the relationship between optical diversity and biodiversity indices were tested at both sites. To study the impact of spatial resolution,

the original data were resampled using the nearest neighbor algorithm to different spatial resolutions (1 mm, 2.5 mm, 5 mm, 1 cm, 2.5 cm, 5 cm, and 8.3 cm), processed with $Level_3$ processing, and then the obtained pixels (approximately 54% of the pixels for IT-PD and 46% for IT-MBo) were used to calculate the optical diversity metrics at each resolution. Finally, to evaluate the sample size effects on the relationships between optical diversity and biodiversity indices, a varying number of pixels (50, 100, 150, 250, 300, and 500) were randomly extracted from the $Level_3$-processed data. Pixel random extraction was re-iterated 10 times and the optical diversity metrics were calculated at each extraction, and the 10 R values of the correlations between biodiversity and optical diversity metrics were averaged.

3.2.6. Statistical Analysis

The Pearson correlation coefficient (R) and the corresponding *p* values between the optical diversity metrics (CV and SD) and the biodiversity indices (species richness, Shannon's index, Simpson's index, and species evenness) of the surveyed plots were calculated with the "cor.test" function in the "stats" package separately for the two grassland sites. Calculations were done for both the original and transformed reflectance data. Normality of the data and residuals of the correlation between the best correlated optical diversity metrics and the field-measured species richness was checked with a Shapiro–Wilk test using the "shapiro.test" function in the "stats" package. The analyses were performed with the statistical software R (version 3.6.1) (R Core Team, 2019).

3.3. Results

In Figure 16 and Figure 17, the mean original reflectance (panel A), mean transformed reflectance (panels B–D), and the spectral diversity metrics (CV and SD, panels E and F, respectively) from each plot are presented with respect to the plot species richness at both study sites.

The original mean reflectance values of the different plots showed some variability, especially in the NIR domain, at both study sites (Figure 16A and Figure 17A). Reflectance values and spectral variability among the plots was reduced when brightness normalization was applied to the hyperspectral image (Figure 16B and Figure 17B). Additionally, the variability was slightly reduced when a filter was used to remove flowers, shadows, and bright pixels from the images C and Figure 4C). The CR spectra calculated from the brightness normalized and filtered images also showed low variability in the spectra, at both study sites (Figure 16D and Figure 17D).

At the IT-PD site, the mean original reflectance obtained from the 1 mm pixel size data (solid line, Figure 16A) was higher compared to the mean reflectance from the 1.5 mm pixel size data (dashed line, Figure 16A). There was not much difference observed between the mean spectra from the two different spatial resolutions (1 and 1.5 mm) at different processing stages (Figure 16B–D). In general, the reflectance increased with the increase of species richness from 1 to 4 and then it started to decrease (Figure 16A). On the other hand, at the IT-MBo, a clear link of the reflectance values with species richness was not noted (Figure 17A).

The optical diversity measured by the CV from the $Level_3$-processed data showed that the spectral variability in the reflectance within plots was particularly high in the VIS part of the spectrum, while the variability in the NIR spectral region was low (Figure 16E). In general, the

highest CV values were observed in the plots where four species were observed, while the lowest CV values in the plots with three species (Figure 16E). Therefore, no manifest association with plant biodiversity was observed. The SD showed three peaks in the blue, green, and red-edge spectral domains, and the lowest SD was detected around 680 nm (Figure 16F).

The lack of relationship between the spectral diversity across the spectrum (CV and SD) and species richness was particularly pronounced at the IT-MBo site (Figure 17). Similarly to the IT-PD site, the CV at the IT-MBo site showed that variability was observed mainly in the VIS part of the spectrum, while the NIR spectral region was characterized by low variability (Figure 17E). The SD at IT-MBo showed three peaks across the spectrum (Figure 17F). As in the IT-PD dataset, the highest values of SD were found around the blue, green, and red-edge part of the spectrum, while the lowest SD was detected around 680 nm at the IT-MBo site (Figure 17F).

In this study, the performance of spectral diversity to estimate plant diversity was not consistent across the spatial scale, over different grassland ecosystems, and across different spectral regions. For the IT-PD site, the Pearson correlation analysis revealed positive correlations between optical diversity metrics (calculated from the $Level_0$ data and averaged across the spectrum) and species diversity except for the SD metric calculated from 1.5 mm pixel size data, which showed almost no correlation in the NIR part of the spectrum (Appendix A, Figure A1). For both datasets, the CV in different spectral regions showed higher R values compared to the SD metric in the VIS and red-edge part of the spectrum. On the other hand, in the NIR spectral region, both metrics showed weak correlations (1 mm: CV: R = 0.23, p = 0.56, SD: R = 0.25, p = 0.51; 1.5 mm: CV: R = 0.13, p = 0.73, SD: R = −0.01, p = 0.98). At the IT-PD site, generally weak correlations were observed between the CV calculated across the spectrum and species richness (1 mm: R = 0.52, p = 0.15; 1.5 mm: R = 0.62, p = 0.08), while the SD metric showed lower R values (1 mm: R = 0.31, p = 0.41; 1.5 mm: R = 0.21, p = 0.59) for both datasets. For the IT-MBo site, the spectral diversity metrics showed contrasting results with pervious work (Aneece et al., 2017; Wang & Gamon, 2018), highlighting a weak correlation between optical diversity and biodiversity indices. The correlations obtained between optical diversity metrics calculated from the $Level_0$ data averaged across the spectral regions and within different spectral regions showed almost no correlation with species richness, although a weak positive correlation for CV and SD averaged in the 408–499 nm spectral region was recorded (Appendix A, Figure A2, panel A). For other biodiversity indices (Shannon's index, species evenness, and Simpson's index) both optical diversity metrics (calculated from the $Level_0$-processed data) mostly showed an inverse correlation both when the CV and SD were averaged within different spectral regions and when it was averaged across the VIS-NIR spectral region (Appendix A, Figure A2, panels B,D).

In a further step, to check the impact of image processing on the metrics performance, we calculated the CV and the SD for each spectral band from both untransformed ($Level_0$) and transformed ($Level_1$, $Level_2$, and $Level_3$) reflectance. We examined the correlations across the spectrum between species richness and both the CV and SD optical diversity metrics and we found high R values for both spatial scales: up to R = 0.83 (CV) and R = 0.84 (SD) and R = 0.87 (CV) and R = 0.86 (SD) for 1 and 1.5 mm pixel size, respectively (Figure 18). We observed that the CV and SD calculated from transformed reflectance showed, in general, higher R values compared to untransformed reflectance. For the 1 mm pixel size image, the correlations between species richness and the CV and SD metrics calculated from the transformed reflectance were mostly positive in the

VIS and negative in the NIR (Figure 18). The maximum R values and their respective wavelengths for both datasets (1 mm and 1.5 mm) and various processing levels are reported in Table S5.

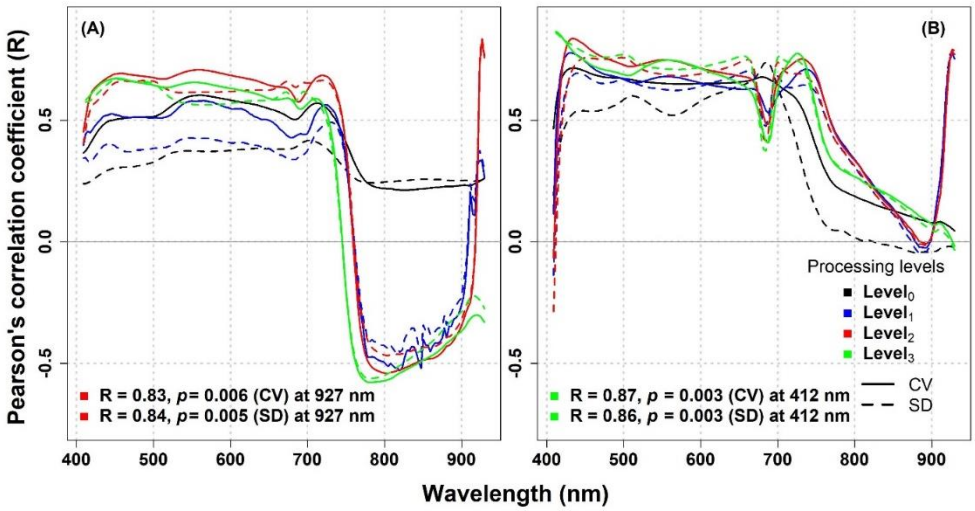

Figure 18. Correlation coefficient from the Pearson correlation analysis (R) between optical diversity expressed as CV and SD for each wavelength from 411 to 930 nm and species richness at the IT-PD site: (**A**): 1 mm pixel size; (**B**): 1.5 mm pixel size), considering different processing levels.

At the IT-MBo site, the shape of the R values curve was very different compared to the IT-PD site (Figure 19). Additionally, lower R values were occurring across the spectrum, with a small spike in the wavelengths around 680 nm for the SD calculated from $Level_2$ and $Level_3$ transformed reflectance. Similar trends were noted for R curves for all the investigated biodiversity indices (Figure 19A–D). The maximum R values and their respective wavelengths and various processing levels at IT-MBo are reported in Table S6.

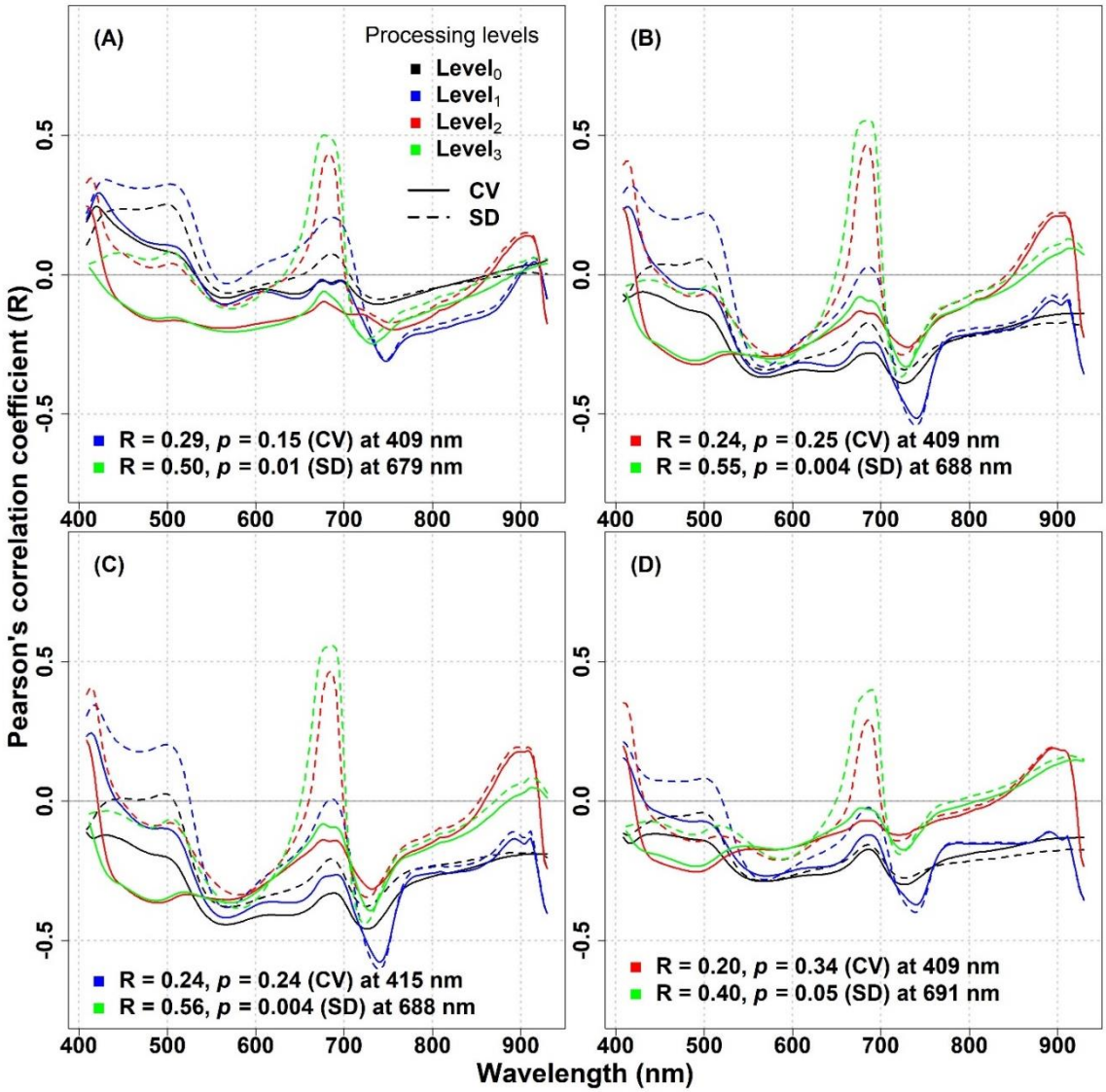

Figure 19. Correlation coefficient from the Pearson correlation analysis (R) between optical diversity expressed as CV and SD for each wavelength from 411 to 930 nm and biodiversity indices at the IT-MBo site: (**A**) species richness; (**B**) Shannon's index; (**C**) species evenness index; (**D**) Simpson's index, considering different processing levels.

3.3.1. The Impact of Spatial Resolution on the Spectral Diversity–Biodiversity Relationships

To study the scale effects, we investigated the relationships between optical diversity and biodiversity metrics at decreasing spatial resolutions (1 mm, 2.5 mm, 5 mm, 1 cm, 2.5 cm, 5 cm, and 8.3 cm) by resampling the original spectral data (Figure 20). For the IT-PD site, in the VIS part of the spectrum a strong relationship between optical diversity metrics and species richness with an R value ($R > 0.5$) was recorded when pixel size was reduced up to 1 cm, while with a larger pixel size (>2.5 cm), the R values started to decrease, reaching a value of −0.15 when the pixel size increased up to 8.3 cm (Figure 20). In the NIR part of the spectrum, a strong inverse correlation was obtained when the CV and the SD were calculated from 1 cm resampled data. The strength of the inverse correlation started to weaken when pixel size increased, and the weakest correlation was noted with 8.3 cm pixel size data ($R = -0.3$). The maximum R values and their respective wavelengths across different spatial resolutions for the IT-PD site are summarized in Table S7.

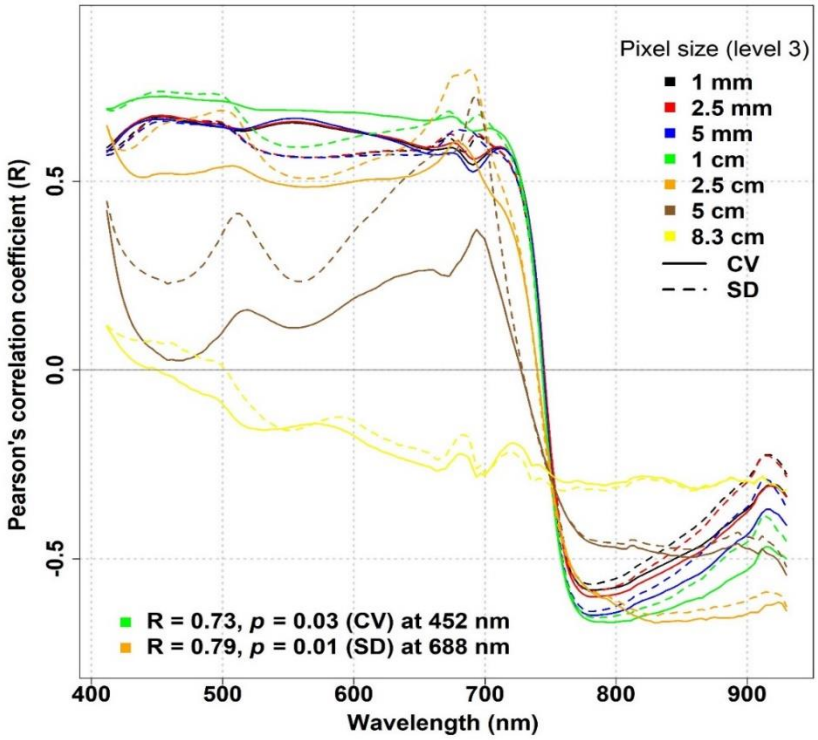

Figure 20. Correlation coefficient from the Pearson correlation analysis (R) at the IT-PD site between optical diversity expressed as CV and SD for each wavelength from 411 to 930 nm at different spatial scales and species richness.

In Figure 21, we considered the effect of pixel downsampling at the IT-MBo site. A clear difference in R values was observed between the two optical diversity metrics: around 680 nm, the SD showed a stronger correlation compared to the CV when the spatial resolution was reduced up to 5 cm, while for 8.3 cm, both metrics showed a weak inverse correlation with biodiversity indices around the same wavelengths. For the SD metric, the effect of pixel downsampling was noticeable when the pixel size went beyond 2.5 mm, as the maximum R value around 680 nm dropped from 0.48 to 0.12, 0.55 to 0.02, 0.54 to 0.01, and 0.39 to −0.16 for the species richness, Shannon's index, species evenness, and Simpson's index, respectively. In general, a similar pattern of R values was observed for all biodiversity indices, where the CV mostly showed an inverse correlation particularly around 550 nm, and the strength of the correlation increased with increasing pixel sizes up to 2.5 cm. On the other hand, for lower spatial resolutions (>2.5 cm), the strength of the correlation weakened, and for 8.3 cm, the weakest correlation was observed at the same wavelength. Similarly, at RE spectral bands (around 720 nm), the effect of decreasing spatial resolution could be noticed as the inverse correlation became stronger at increasing pixel sizes up to 5 cm.

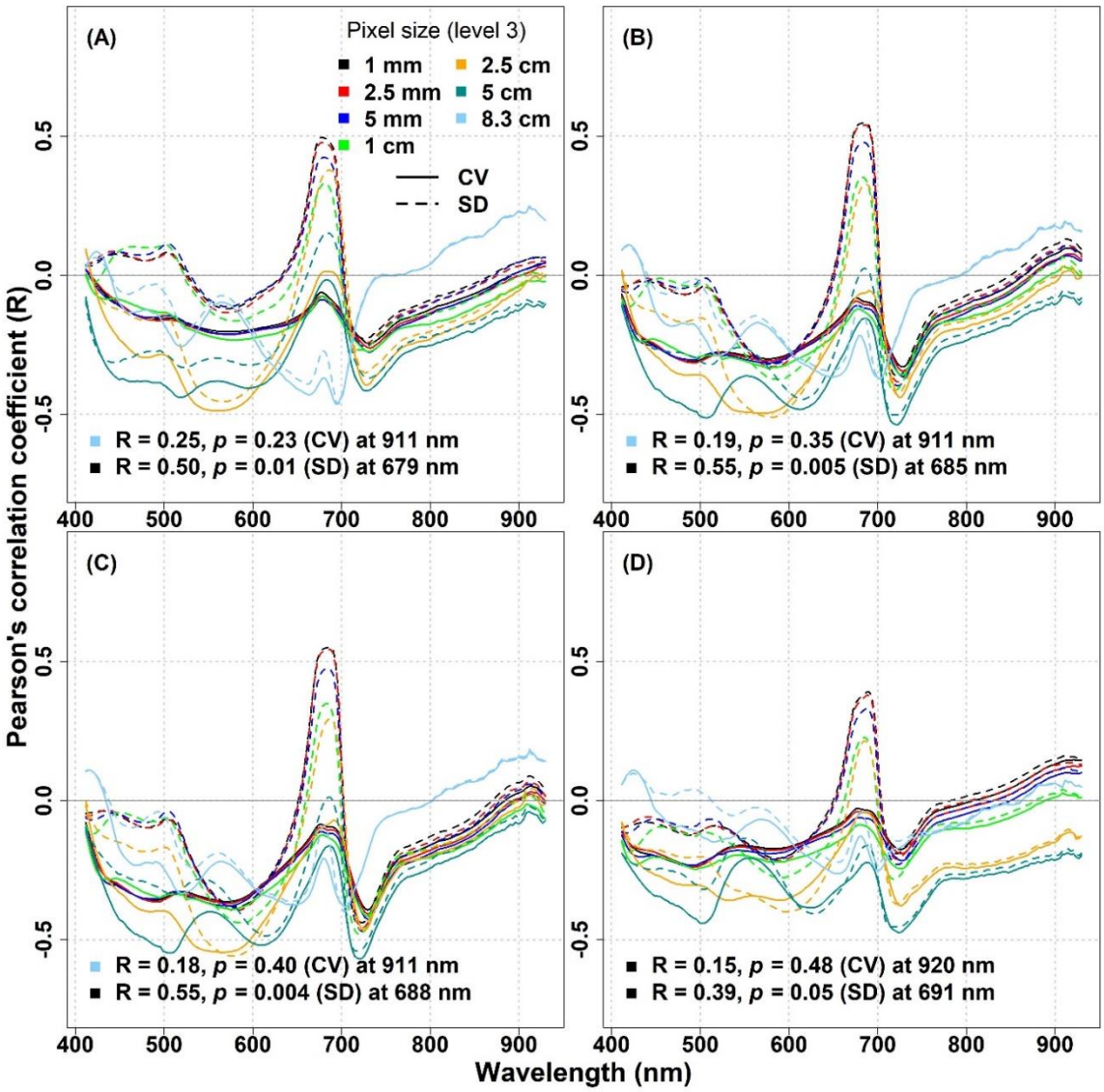

Figure 21. Correlation coefficient from the Pearson correlation analysis (R) between the optical diversity expressed as CV and SD for each wavelength from 411 to 930 nm at different spatial scales and biodiversity indices at the IT-MBo site: (**A**) species richness; (**B**) Shannon's index; (**C**) species evenness; (**D**) Simpson's index.

3.3.2. The Impact of Pixel Subsampling on the Spectral Diversity–Biodiversity Relationships

In Figure 22, we present the results achieved by using the subsampling approach presented by Schweiger et al. (2018) to calculate the optical diversity. For the IT-PD plots, subsampling by random pixel extraction generally did not cause any major changes in the R patterns across the spectrum, except for the NIR region, in which subsampling based on 50, 100, 250, and 300 pixels resulted in a noticeable reduction in the R values (Figure 22). Nevertheless, positive R values were observed in the VIS part of the spectrum, while mostly negative R values were observed in the NIR spectral bands.

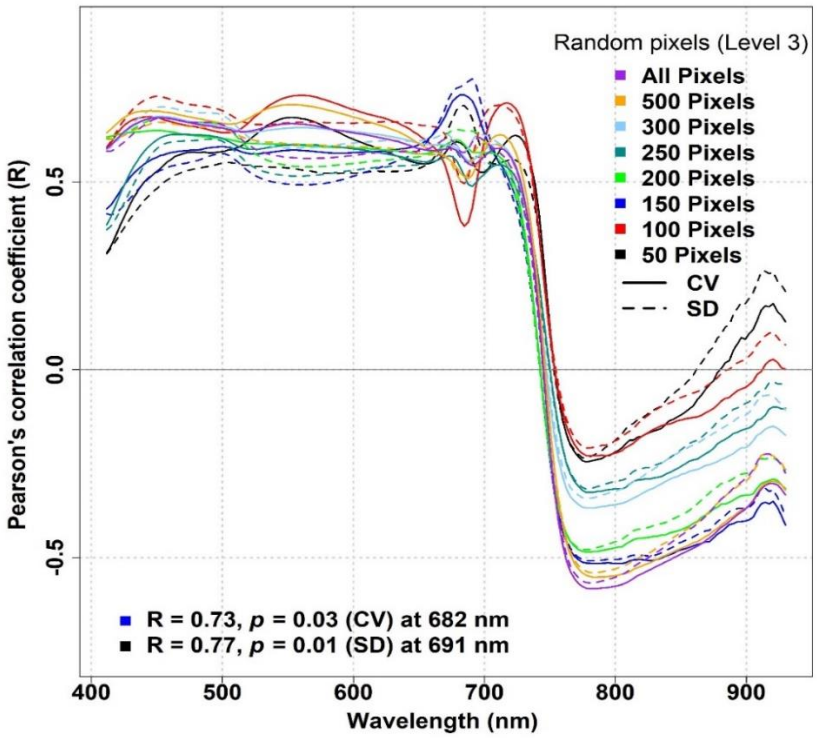

Figure 22. Correlation coefficient from the Pearson correlation analysis (R) between optical diversity expressed as CV and SD for each wavelength from 411 to 930 nm and species richness at the IT-PD site considering different numbers of pixels.

Similarly, for the IT-MBo site, there were generally no considerable improvements in the correlation coefficient between the optical diversity metrics calculated using randomly extracted subsample pixels and biodiversity indices compared to the results found between the same metrics when considering all pixels (Figure 23). In general, the SD metric showed stronger relationships with biodiversity indices compared to the CV metric. The highest R value ($R \geq 0.5$) was observed around 680 nm when 250 pixels were used to calculate the SD for all biodiversity indices, while for the CV around the same wavelength, very low R values ($R \leq 0.09$) were obtained (Figure 23A–D). For the IT-MBo site, the strongest relationship was observed between the Simpson's index and the SD metric calculated with 250 pixels at 685 nm ($R = 0.62$, $p = 0.001$, Figure 23D).

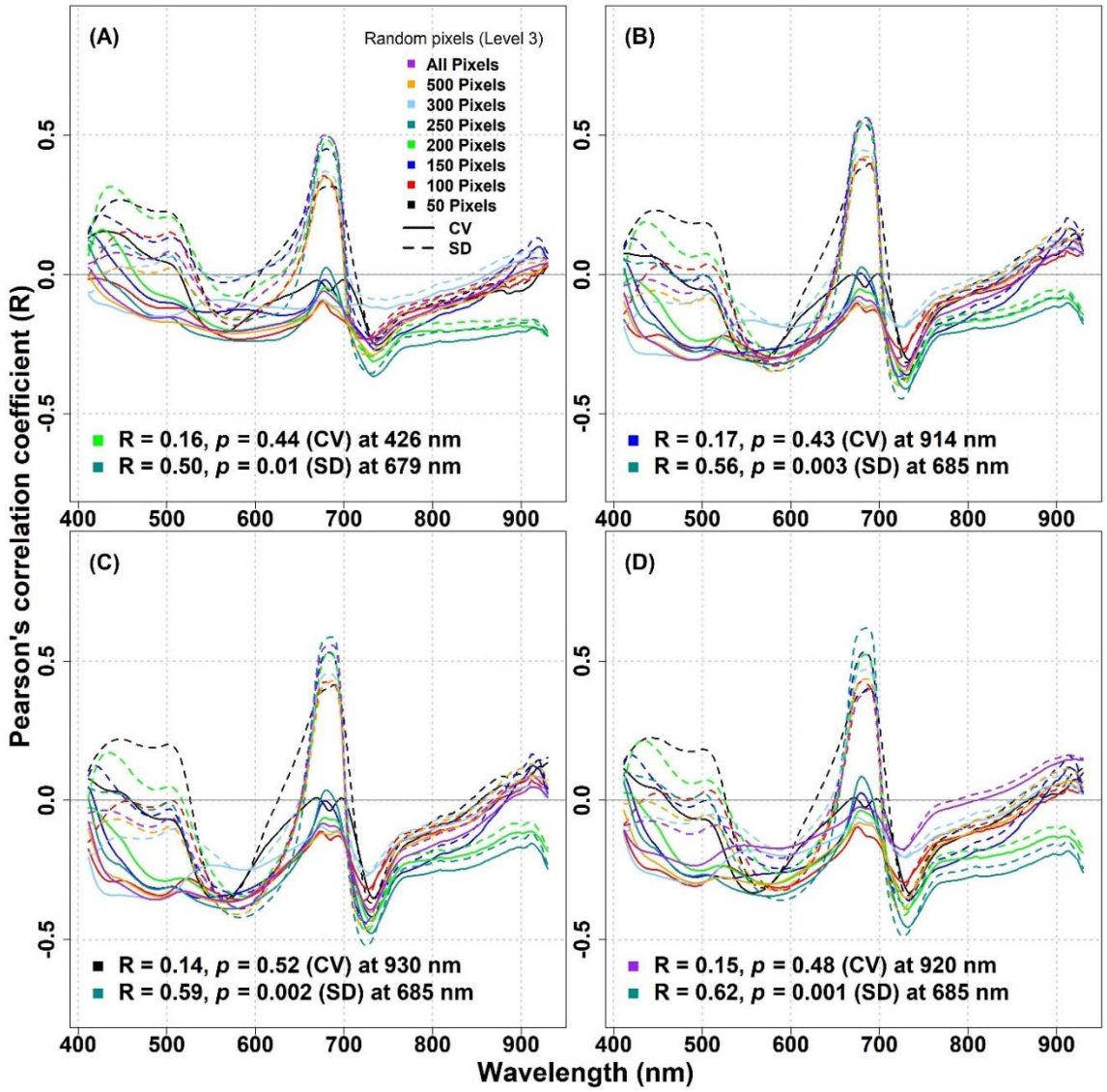

Figure 23. Correlation coefficient from the Pearson correlation analysis (R) between optical diversity expressed as CV and SD for each wavelength from 411 to 930 nm and biodiversity indices at the IT-MBo site: (**A**) species richness index; (**B**) Shannon's index; (**C**) species evenness; (**D**) Simpson's index, considering different number of pixels.

3.4. Discussion

Similarly, to other authors (Aneece et al., 2017; Peng et al., 2019; Wang & Gamon, 2018), our study found a significant relationship between spectral diversity (expressed as CV and SD) and species diversity in the lower-diversity artificial grassland site. However, the data acquired at the semi-natural subalpine grassland at IT-MBo with the same methodology and analyzed with the same approach provided much weaker correlations. Such results may be due to the very high level of biodiversity (up to 17 species in a 0.25 × 0.25 m plot) and to the rather complex structure of the IT-MBo grasslands (Imran et al., 2020) compared to the low-diversity turf canopy at the IT-PD site. Our main findings questioned the applicability of the optical diversity method to estimate biodiversity in highly diverse grasslands, such as the ones at the IT-MBo site. Despite the fact that we used several different processing techniques to enhance the optical diversity signal, for the subalpine grassland site of IT-MBo, we were not able to match the performance of optical-based

methods to estimate the biodiversity reported in other studies (Aneece et al., 2017; Peng et al., 2019; Wang & Gamon, 2018). In Aneece et al. (2017), an artificial ecosystem (with max. 5 species/m^2) was investigated, and the maximum R^2 value of the correlation between the optical diversity and α-diversity was 0.43. Wang et al. (2018) carried out on an artificial grassland (max. 16 species/m^2), in which the maximum R^2 value reached 0.58, while in the study of Peng et al. (2019), which focused on natural grasslands (with a maximum species richness of 12 in a 0.8 m diameter plot), the maximum R^2 value reached 0.40.

In our study, when optical diversity metrics were averaged across different spectral regions as in Aneece et al. (2017) and across the spectrum as in Wang et al. (2018), we found contradictory results at the two sites. At the IT-PD site, a positive correlation between optical diversity metrics and biodiversity indices was mostly observed, while at the IT-MBo site, the correlation was mostly negative (IT-PD and IT-MBo; Appendix A, Figure A1, panels A, B and Figure A2, panels A–D, respectively). When the CV and the SD were calculated for each spectral band on a separate basis, the R reached much higher values: 0.84 (SD metric at 927 nm) and 0.87 (CV metric at 412 nm) in the artificial turfgrass (maximum number of species was 9 in a 0.25 × 0.25 m and 0.5 × 0.5 m area). The maximum R value in the species-rich subalpine grassland was only 0.56 for the SD metric at 688 nm (maximum number of species was 17 in a 0.25 × 0.25 m area, Figure 19, panel C). Considering these results, we may conclude that the optical diversity approach appears more suitable for lower-diversity or artificial systems, and its application may be more challenging in highly diverse grasslands.

The applicability of the methods to estimate species diversity using hyperspectral data was also questioned by other authors (Gholizadeh et al., 2018; Lucas and Carter, 2008). In these studies, the relationships between species diversity and optical diversity metrics were not consistent across plant communities. Lucas and Carter (2008) evaluated the prediction of species diversity (species richness) in Horn Island, Mississippi by using ground transect data and remotely sensed data. However, they failed to find a significant relationship between spectral diversity metrics and species richness, which may be due to the fact that their study considered highly diverse habitat types. Gholizadeh et al. (2018) investigated the SVH-based approaches to access the α-diversity in Cedar Creek Ecosystem Science Reserve in Central Minnesota, USA and highlighted the effect of soil background on the performance of optical diversity metrics. The authors achieved significant correlations between spectral diversity metrics and the species richness when they applied an NDVI filter to remove the soil background from the hyperspectral image. In our study, however, the impact of soil was minimal, as the fractional cover of the vast majority of the plots was 100% (it was lower than 100% in only eight plots, but always higher than 99.5%). Wang et al. (2018) provided significant and detailed insights on the possible factors affecting the optical diversity and biodiversity relationships, highlighting the fact that canopy structure effects can determine substantial illumination and scattering differences and both leaf traits and canopy structure strongly influence optical diversity metrics. As a consequence of the fact that canopy structure can influence the optical diversity and modify the optical diversity–plant diversity relationships, we can expect that in heterogeneous grasslands characterized by complex structural patterns and by a very high number of species, biodiversity estimations based on optical diversity are not always reliable.

In this work, we adopted a range of techniques to fully disentangle the optical diversity due to plant diversity from the optical diversity due to illumination artifacts, or due to the presence of

pixels of non-photosynthetic material, such as dead material or flowers. The results of this paper highlight the impact of image processing techniques on the relationships between optical data and grassland diversity. The developed processing flow proved, in general, to slightly improve the remote estimations of plant diversity, by limiting the influence of the factors determining optical diversity but not related to plant diversity. As shown by other authors, spectral diversity is affected by canopy non-photosynthetic elements, such as flowers and, dead material, as well as by shaded pixels, overexposed pixels, and the soil background (Gholizadeh et al., 2018; Lopatin et al., 2017; Peng et al., 2019; Wang & Gamon, 2018). To normalize the effect of shadows, Feilhauer et al. (2010) proposed the brightness normalization approach to minimize the spectral differences between the sunlit and shaded areas. In the present study, we observed that after applying brightness normalization to the hyperspectral images, the reflectance variability in the NIR was strongly reduced. In our case, the performance of the models to estimate grassland biodiversity did not significantly improve compared to the original dataset when this transformation method was used alone. However, the filtering of flowers, shadows, and bright pixels and then the transformation of the reflectance to CR minimized the spectral differences, which were not linked to species diversity and improved the diversity estimations. Heumann et al. (2015) studied the impact that flowers have on spectral diversity and investigated how this may influence the applicability of the spectral diversity hypothesis. These authors reported that the inclusion of flower spectra increased the normalized root mean square error (nRMSE) by 30% for Shannon's diversity index, because there would be more inherent spectral diversity for each given species due to the spectral response difference between leaves and flowers.

The optical diversity–plant diversity relationships appeared to be both ecosystem-dependent and scale-dependent. Spatial scale was shown to strongly affect the spectral diversity–biodiversity relationships. In the study of Wang et al. (2018), with decreasing spatial resolution, the variability in reflectance and, therefore, CV and SD decreased, and the optical detectability of biodiversity was reduced. In our study, however, the correlation between optical diversity metrics and species richness initially increased and was only reduced when the pixel size was beyond 2.5 cm in IT-PD, even if for most of the species the average leaf size was much lower than this value. For IT-MBo, the optimal pixel size (at 680 nm) was 1 mm. Conversely, according to Wang et al. (2018) the optimal pixel size to detect species diversity using spectral diversity should match the size of the objects within the sampling unit.

Another key finding of this paper concerns the impact of processing methods on the performance of the optical diversity approach. When we compared the performances of the CV and SD metrics, we demonstrated that $Level_3$ data generally showed higher correlations with biodiversity indices, and that the use of CR spectra generally improved the R values of the correlation between SD and species diversity. Similarly, to Blanco-Sacristán et al. (2019), we found that the spectral bands in the red part of the spectrum (around 680 nm) showed to be best for estimating biodiversity in both grasslands. In our study, a random extraction of pixels did not improve our results as in Schweiger et al. (2018), who achieved successful results based on links between spectral, functional, and phylogenetic diversity.

Man-made grasslands, obtained by sowing, are simplified ecosystems which may not be representative of the complexity of natural field ecological conditions, where leaf and canopy traits can contribute to optical diversity in several ways, adding complexity to the optical and plant

diversity relationships in natural grasslands (Wang et al., 2019). This can explain the poor performance of the optical sampling methods in complex grassland canopies. In this respect, Wang et al. (2018a), adopting a modeling approach, observed that grassland biodiversity estimations are strongly affected by species intra-variations, which can be relevant even when caused by a single species. In natural grasslands located in heterogeneous landscapes such as the environment of the Alps, where (i) different associations and sub-associations can be found within a few meters distance, and transition zones are very frequent, (ii) geomorphology, soil characteristics and origin, and grassland vertical structure profile can strongly vary on the spatial basis, and (iii) the number of species is particularly high, estimating grassland α-diversity using optical methods can be extremely challenging. From an ecological point of view, Grace et al. (2007) highlighted the limits of manipulation experiments and the need for more analyses focused on mature natural ecosystems. In this regard, these authors stated that the ecological mechanisms cannot be extrapolated from studies of synthesized assemblages to mature natural ecosystems. Analogously, the optical diversity approach—based on grassland functional diversity dynamics determining spectra variability—may not be always transferable to mature and very complex natural grassland ecosystems.

The VIS part of the spectrum (and in particular the red domain), characterized by a strong absorbance, showed to be one of the key spectral areas for biodiversity detection. This highlights the importance for further studies to investigate canopy biochemistry variability and its link with both biodiversity and optical diversity. To detect α-biodiversity using optical methods, we should be able to detect biochemistry content and its variability within the canopy. However, this may not be possible when grasslands with heterogeneous structure are observed. Previous studies on the IT-MBo grasslands (Imran et al., 2020) determined how, due to structural complexity and heterogeneity, plant trait co-variation can strongly affect the ability to retrieve grassland traits using spectral data. More work is needed to determine how, in different grassland ecosystems, the optical dissimilarity of canopy spectra captures grassland functional differences and biochemical content variability (at the plot and at the spatial scale) determined by plant diversity. Additionally, further research will be able to clarify if in complex heterogeneous ecosystems, such as the grasslands of the Alps, the optical diversity approach can be adopted at the spatial scale to detect β-diversity. Such insights will provide more robust information on the mechanisms linking the optical diversity and the overall plant diversity.

3.5. Conclusions

Our study provided important observations on the performance of high spatial resolution imagery for grassland plant diversity estimations. The relationship between optical diversity and biodiversity proved to be ecosystem dependent. The spectral diversity approach to estimate biodiversity showed a similar performance to previous studies when artificially established grasslands were observed. On the other hand, in the natural subalpine grasslands of IT-MBo, this approach did not achieve satisfactory results, even if specific processing techniques were adopted to disentangle the optical diversity due to plant diversity from the optical diversity related to shadows, flowers, and brown material. The SD metric calculated from the $Level_3$ data in the red spectral domain (around 680 nm) showed the best optical diversity metric to estimate biodiversity in both study sites. The results of our study showed that the use of the optical diversity approach as a proxy

of plant diversity has some limitations, particularly when high-biodiversity natural landscapes are observed.

Spectral variation drivers include not only species richness but other important factors, e.g., intra-specific optical, biophysical, and biochemical variability. Other important factors include, e.g., vegetation structure, shadows, and phenology. Several post-processing methods (including brightness normalization, filtering of shadowed and bright pixels, non-photosynthetic element pixels filtering, and continuum removal) were tested successfully, which generally improved the performance of the optical diversity models. On the other hand, the pixel subsampling approach was not shown to be effective in our study. Interesting insights were provided by the scale effect study, such as that the optimum pixel size (1 cm) for biodiversity estimations—at the turf grass site—was generally higher than expected, according to previous studies. However, more advanced post-processing image methods or the adoption of higher resolution imagery (pixel size < 1 mm, which was not tested in this study) may improve the performance of the optical diversity metrics to estimate biodiversity even in heterogeneous grassland ecosystems. More studies are needed to fully investigate the mechanisms at the basis of the optical diversity, to highlight the pigment content variability and α-diversity relationships in high biodiversity grasslands, and to provide novel insights on the reliability of β-diversity estimations at the spatial scale.

3.6. Appendix A

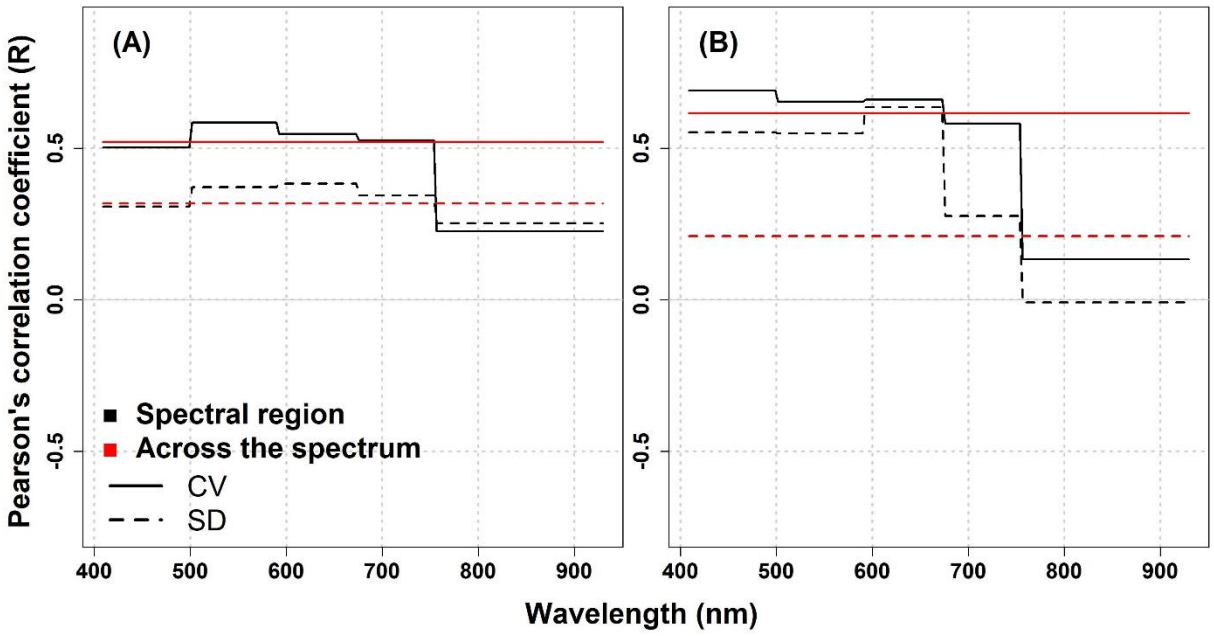

Figure A1. Correlation coefficient from the Pearson correlation analysis (R) between the species richness and optical diversity expressed as CV and SD, averaged across different spectral regions (black lines) and averaged across the spectrum (red lines) computed from the Level$_0$-processed data at the IT-PD site (panel (**A**): 1 mm pixel size; panel (**B**): 1.5 mm pixel size).

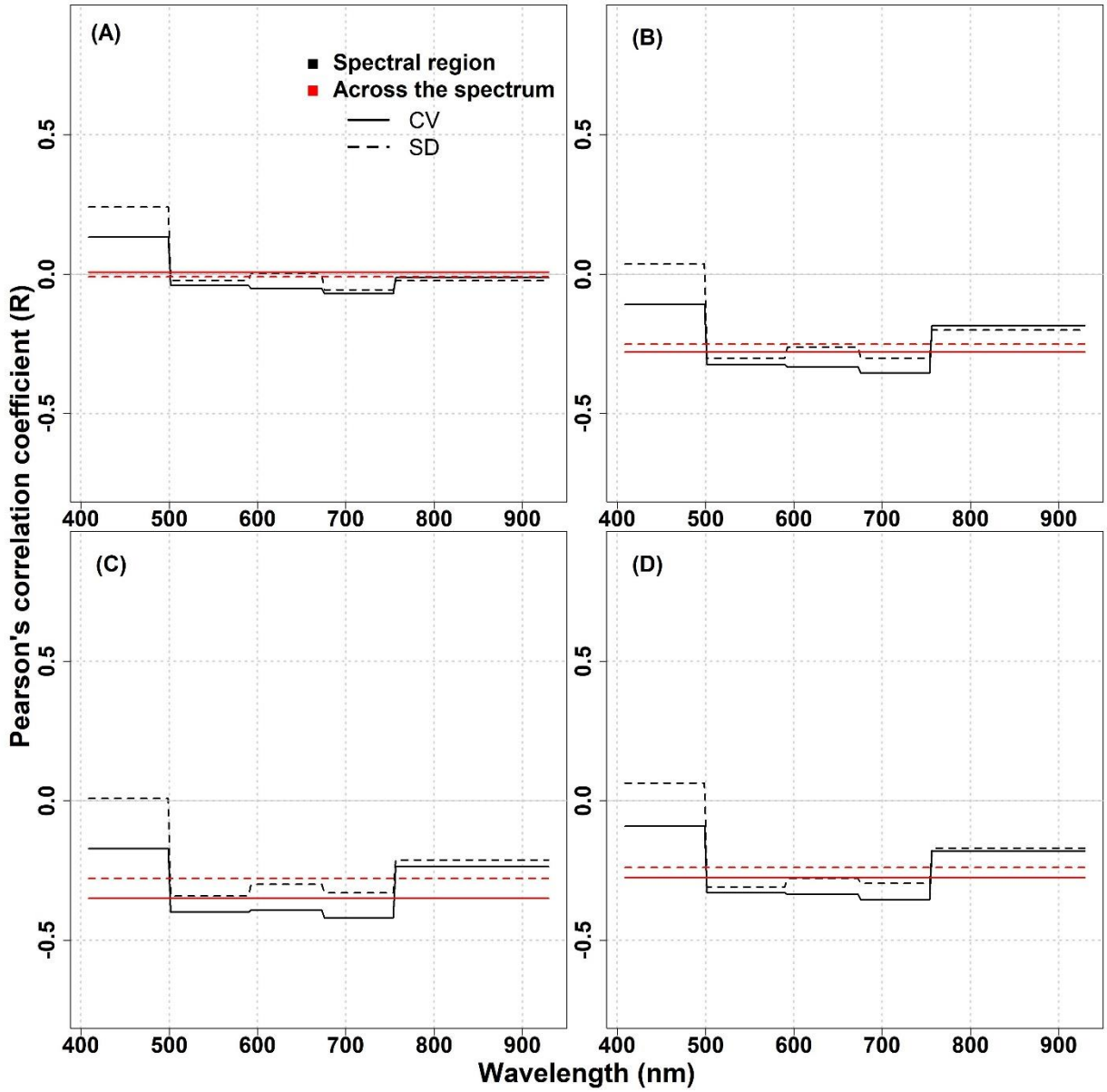

Figure A2. Correlation coefficient from the Pearson correlation analysis (R) between the optical diversity expressed as CV and SD, averaged across different spectral regions (black lines) and averaged across the spectrum (red lines) computed from the $Level_0$-processed data at the IT-MBo site (panel A–D: approximately 0.9 mm pixel size) and biodiversity indices: (**A**) species richness; (**B**) Shannon's index; (**C**) species evenness; (**D**) Simpson's index.

3.7. Supplementary Materials

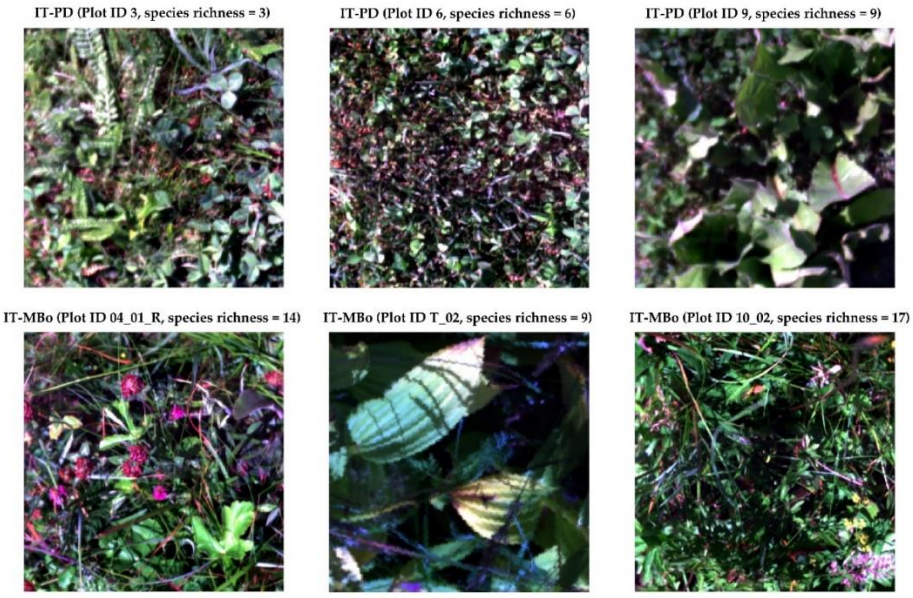

Figure S6. RGB images of the different plots at the IT-PD and the IT-MBo study sites.

Table S3. Species richness and composition of each plot investigated at the IT-PD study site.

Plot	Species richness	Species
1	1	*Trifolium repens nano*
2	2	*Festuca rubra, Trifolium repens nano*
3	3	*Achillea millefolium, Festuca rubra, Trifolium repens nano*
4	4	*Lolium perenne, Trifolium repens nano, Cicoria selvatica, Poa pratensis*
5	5	*Lolium perenne, Trifolium repens nano, Cicoria selvatica, Poa pratensis, Medicago lupulina*
6	6	*Lolium perenne, Trifolium repens nano, Cicoria selvatica, Poa pratensis, Medicago lupulina, Poa annua*
7	7	*Lolium perenne, Trifolium repens nano, Cicoria selvatica, Poa pratensis, Medicago lupulina, Poa annua, Festuca arundinacea*
8	8	*Lolium perenne, Trifolium repens nano, Cicoria selvatica, Poa pratensis, Medicago lupulina, Poa annua, Festuca arundinacea, Taraxacum officinale*
9	9	*Lolium perenne, Trifolium repens nano, Cicoria selvatica, Poa pratensis, Medicago lupulina, Poa annua, Festuca arundinacea, Taraxacum officinale, Lotus corniculatus*

Table S4. Species richness and composition of each of the 25 plots investigated at the IT-MBo study site.

Plot	Species richness	Species
01_2	*16*	*Agrostis tenuis, Brachypodium pinnatum (rup), Briza media Chamaecytisus hirsutus, Euphrasia rostkoviana, Festuca nigrescens, Galium pumilum, Lotus corniculatus, Nardus stricta, Phleum alpinum, Polygonum viviparum, Potentilla crantzii, Potentilla erecta, Ranunculus montanus, Trifolium pratense, Trifolium repens*
02_2	*13*	*Achillea millefolium, Agrostis tenuis, Crocus albiflorus, Euphrasia rostkoviana, Galium pumilum, Hieracium cymosum, Nardus stricta, Pimpinella major, Polygonum viviparum, Potentilla erecta, Ranunculus montanus, Trifolium pratense, Trifolium repens*
04_1_R	*14*	*Achillea millefolium, Anthoxanthum odoratum, Brachypodium pinnatum (rup), Chaerophyllum hirsutum, Galium pumilum, Helianthemum numm. grandifl., Laserpitium krapfii ssp. Gaudinii, Lathyrus pratensis, Nardus stricta, Paradisea liliastrum, Phyteuma betonicifolium, Polygonum viviparum, Potentilla erecta, Trifolium pratense*
05_2	*12*	*Achillea millefolium, Agrostis tenuis, Festuca nigrescens, Hypericum maculatum, Lathyrus pratensis, Lotus corniculatus, Nardus stricta, Plantago atrata, Polygonum viviparum, Potentilla erecta, Ranunculus montanus, Trifolium repens*
06_2	*13*	*Alchemilla vulgaris, Festuca nigrescens, Gentianella germanica, Leucanthemum vulgare, Lotus corniculatus, Nardus stricta, Plantago atrata, Poa violacea, Polygonum viviparum, Potentilla erecta, Rhinanthus alectorolophus, Trifolium montanum, Trifolium repens*
07_2	*12*	*Carex montana, Cerastium caespitosum, Festuca nigrescens, Helianthemum numm. grandifl., Lathyrus pratensis, Phyteuma orbiculare, Plantago atrata, Pulsatilla alpina ssp. Alpina, Rumex alpestris, Stachys alopecuros, Trifolium pratense, Vicia cracca*
08_2	*9*	*Agrostis tenuis, Chamaecytisus hirsutus, Festuca nigrescens, Genista germanica, Luzula campestris, Nardus stricta, Plantago atrata, Polygonum viviparum, Potentilla erecta*
09_2	*12*	*Achillea millefolium, Agrostis tenuis, Chamaecytisus hirsutus, Festuca nigrescens, Helianthemum numm. grandifl., Hieracium cymosum, Lotus corniculatus, Plantago atrata, Polygonum viviparum, Ranunculus montanus, Stachys alopecuros, Trifolium montanum*
10_2	*17*	*Agrostis tenuis, Alchemilla vulgaris, Crocus albiflorus, Festuca nigrescens, Galium pumilum, Hieracium pilosella, Laserpitium krapfii ssp. Gaudinii, Lathyrus pratensis, Leontodon hispidus, Polygonum viviparum, Potentilla erecta, Ranunculus montanus, Scorzonera aristata, Trifolium montanum, Trifolium pratense, Trifolium repens, Trollius europaeus*
11_2	*9*	*Achillea millefolium, Brachypodium pinnatum (rup), Briza media, Genista tinctoria, Lilium martagon, Phyteuma betonicifolium, Pulsatilla alpina ssp. Alpina, Ranunculus montanus, Trifolium pratense*

12_2	*15*	*Agrostis tenuis, Cerastium caespitosum, Chamaecytisus hirsutus, Crocus albiflorus, Festuca nigrescens, Galium pumilum, Galium rubrum, Genista tinctoria, Geum montanum, Nardus stricta, Paradisea liliastrum, Polygonum viviparum, Pulsatilla alpina ssp. Alpina, Vaccinium myrtillus, Viola canina*
13_2	*16*	*Arnica montana, Chaerophyllum hirsutum, Crocus albiflorus, Euphrasia rostkoviana, Galium pumilum, Geum montanum, Nardus stricta, Phleum alpinum, Phyteuma betonicifolium, Plantago atrata, Polygonum viviparum, Potentilla erecta, Ranunculus montanus, Stellaria graminea, Trifolium pratense, Trifolium repens*
14_2	*14*	*Achillea millefolium, Agrostis tenuis, Cerastium caespitosum, Chaerophyllum hirsutum, Dactylis glomerata, Festuca nigrescens, Hypericum maculatum, Phleum alpinum, Poa violacea, Polygonum viviparum, Ranunculus montanus, Rumex alpestris, Stellaria graminea, Trifolium repens*
16_2	*15*	*Agrostis tenuis, Chaerophyllum hirsutum, Chamaecytisus hirsutus, Galium pumilum, Nardus stricta, Paradisea liliastrum, Phleum alpinum, Phyteuma betonicifolium, Polygonum viviparum, Potentilla erecta, Pulsatilla alpina ssp. Alpina, Ranunculus montanus, Stellaria graminea, Trifolium repens, Trollius europaeus*
17_2	*15*	*Agrostis tenuis, Alchemilla vulgaris, Campanula scheuchzeri, Chaerophyllum hirsutum, Dactylis glomerata, Festuca nigrescens, Nardus stricta, Poa pratensis, Polygonum viviparum, Potentilla crantzii, Ranunculus montanus, Trifolium pratense, Trifolium repens, Valeriana wallrothii, Veronica chamaedrys*
18_2	*11*	*Achillea millefolium, Agrostis tenuis, Brachypodium pinnatum (rup), Briza media, Chamaecytisus hirsutus, Crocus albiflorus, Dactylis glomerata, Hypericum maculatum, Phleum alpinum, Polygonum viviparum, Trifolium repens*
19_2	*15*	*Agrostis tenuis, Campanula scheuchzeri, Cerastium caespitosum, Chaerophyllum hirsutum, Crocus albiflorus, Euphrasia rostkoviana, Festuca nigrescens, Geum montanum, Plantago atrata, Polygonum viviparum, Potentilla crantzii, Potentilla erecta, Ranunculus montanus, Stellaria graminea, Trifolium repens*
20_2	*16*	*Agrostis tenuis, Brachypodium pinnatum (rup), Centaurea triumfettii, Festuca nigrescens, Helianthemum numm. grandifl., Heracleum sphondylium L., Koeleria pyramidata, Phyteuma orbiculare, Plantago atrata, Poa violacea, Polygonum viviparum, Potentilla erecta, Ranunculus montanus, Trifolium montanum, Trifolium repens, Viola canina*
T_02	*9*	*Achillea millefolium, Alchemilla vulgaris, Brachypodium pinnatum (rup), Briza media, Chamaecytisus hirsutus, Festuca nigrescens, Koeleria pyramidata, Poa chaixii, Veratrum album*
T_03	*4*	*Agrostis tenuis, Carex sp., Epilobium angustifolium, Fragaria sp.*

T_05	*11*	*Agrostis tenuis, Chamaecytisus hirsutus, Crocus albiflorus, Festuca nigrescens, Galium pumilum, Helianthemum numm. grandifl., Nardus stricta, Polygonum viviparum, Trifolium montanum, Trifolium pratense, Trifolium repens*
T_10_B	*2*	*Agrostis tenuis, Chaerophyllum hirsutum*
T_14	*16*	*Achillea millefolium, Agrostis tenuis, Festuca nigrescens, Festuca pratensis, Galium spp., Leontodon hispidus, Leucanthemum vulgare, Phyteuma betonicifolium, Plantago atrata, Ranunculus montanus, Rhinanthus alectorolophus, Stellaria graminea, Trifolium pratense, Trifolium repens, Trisetum flavescens, Veronica chamaedrys*
T_15	*14*	*Achillea millefolium, Agrostis tenuis, Dactylis glomerata, Festuca nigrescens, Festuca pratensis, Galium spp., Gentiana kochiana, Gentiana lutea, Leontodon hispidus, Plantago atrata, Trifolium pratense, Trifolium repens, Trisetum flavescens, Veronica chamaedrys*
T_20	*10*	*Agropyron repens, Alchemilla vulgaris, Alopecurus pratensis, Dactylis glomerata, Festuca pratensis, Ranunculus acris, Rumex obtusifolius, Taraxacum officinale, Trisetum flavescens, Vicia sepium*

Table S5. The highest Pearson correlation coefficient (R) and *p*-values (in brackets) for the relationship between species richness and two optical diversity metrics (CV and SD) for different processing levels at the IT-PD study site. The highest R values for each processing level are highlighted in bold.

Processing levels	IT-PD 1 mm				IT-PD 1.5 mm			
	WL[1]	**CV[1]**	**WL**	**SD[1]**	**WL**	**CV**	**WL**	**SD**
$Level_0$	560	0.60 (0.086)	703	0.42 (0.265)	435	0.71 (0.031)	685	**0.74 (0.023)**
$Level_1$	563	0.58 (0.102)	733	0.49 (0.179)	432	0.78 (0.014)	927	**0.78 (0.013)**
$Level_2$	927	0.83 (0.006)	927	**0.84 (0.005)**	435	0.84 (0.005)	927	0.80 (0.011)
$Level_3$	452	0.67 (0.048)	455	0.67 (0.049)	412	**0.87 (0.003)**	412	0.86 (0.003)

[1] WL: wavelength, CV: coefficient of variation, SD: standard deviation.

Table S6. The highest Pearson correlation coefficient (R) and *p*-values (in brackets) for the relationship between biodiversity indices (species richness, Shannon's index, species evenness, and Simpson's index) and the two optical diversity metrics (CV and SD) for different processing levels at the IT-MBo study site. The highest R values for each processing level are highlighted in bold.

Processing levels	Richness				Shannon				Evenness				Simpson			
	WL[1]	CV[1]	WL	SD[1]	WL	CV	WL	SD	WL	CV	WL	SD	WL	CV	WL	SD
$Level_0$	420	0.25 (0.236)	499	**0.25 (0.224)**	429	-0.06 (0.772)	499	0.06 (0.79)	409	-0.11 (0.594)	499	0.03 (0.898)	446	-0.12 (0.576)	499	-0.04 (0.847)
$Level_1$	423	0.29 (0.154)	429	0.34 (0.096)	415	0.24 (0.24)	418	0.32 (0.118)	415	0.24 (0.24)	418	**0.35 (0.091)**	409	0.16 (0.459)	409	0.21 (0.308)
$Level_2$	409	0.25 (0.236)	682	0.43 (0.03)	409	0.24 (0.248)	685	**0.48 (0.018)**	409	0.22 (0.294)	685	0.47 (0.019)	409	0.20 (0.344)	409	0.35 (0.084)
$Level_3$	930	0.04 (0.852)	679	0.5 (0.011)	911	0.10 (0.652)	688	0.55 (0.004)	911	0.05 (0.816)	688	**0.56 (0.004)**	920	0.15 (0.479)	691	0.4 (0.047)

[1] WL: wavelength, CV: coefficient of variation, SD: standard deviation.

Table S7. The highest Pearson correlation coefficient (R) and *p*-values (in brackets) for the relationship between species richness and the two optical diversity metrics (CV and SD) calculated from $Level_3$ processed data at different spatial scales for the IT-PD study site. The highest R values for each spatial scale are highlighted in bold.

Spatial scale	IT-PD 1 mm			
	WL[1]	**CV[1]**	**WL**	**SD[1]**
1 mm	452	**0.67 (0.05)**	455	**0.67 (0.05)**
2.5 mm	452	**0.67 (0.05)**	455	**0.67 (0.05)**
5 mm	554	**0.68 (0.05)**	455	0.66 (0.054)
1 cm	452	0.73 (0.027)	452	**0.74 (0.023)**
2.5 cm	412	0.65 (0.059)	688	**0.79 (0.011)**
5 cm	412	0.42 (0.257)	694	**0.73 (0.027)**
8.3 cm	412	0.11 (0.769)	412	**0.12 (0.762)**

[1] WL: wavelength, CV: coefficient of variation, SD: standard deviation.

Table S8. The highest Pearson correlation coefficient (R) and *p*-values (in brackets) for the relationship between biodiversity indices (species richness, Shannon's index, species evenness, and Simpson's index) and two optical diversity metrics (CV and SD) calculated from $Level_3$ processed data at different spatial scales for the IT-MBo study site. The highest R values for each spatial scale are highlighted in bold.

Spatial scale	Richness				Shannon				Evenness				Simpson			
	WL[1]	CV[1]	WL	SD[1]	WL	CV	WL	SD	WL	CV	WL	SD	WL	CV	WL	SD
1 mm	930	0.05 (0.833)	679	0.50 (0.012)	914	0.10 (0.643)	685	**0.55 (0.005)**	911	0.05 (0.807)	688	0.55 (0.004)	921	0.15 (0.482)	691	0.39 (0.054)
2.5 mm	930	0.03 (0.875)	679	0.48 (0.016)	921	0.08 (0.715)	688	**0.54 (0.005)**	914	0.03 (0.881)	688	**0.54 (0.005)**	921	0.13 (0.549)	688	0.38 (0.062)
5 mm	930	0.05 (0.828)	682	0.42 (0.035)	914	0.07 (0.737)	685	**0.48 (0.016)**	911	0.02 (0.913)	685	**0.48 (0.016)**	930	0.10 (0.628)	688	0.33 (0.105)
1 cm	412	0.00 (0.996)	682	0.33 (0.108)	908	0.03 (0.877)	682	**0.35 (0.085)**	908	-0.01 (0.955)	685	0.35 (0.088)	908	0.03 (0.894)	688	0.23 (0.274)
2.5 cm	412	0.09 (0.653)	685	**0.38 (0.063)**	917	0.02 (0.934)	685	0.33 (0.11)	917	0.02 (0.919)	688	0.29 (0.154)	685	-0.04 (0.84)	688	0.22 (0.3)
5 cm	682	-0.02 (0.942)	685	**0.15 (0.466)**	911	-0.07 (0.729)	685	0.03 (0.907)	911	-0.04 (0.852)	685	0.01 (0.953)	914	-0.19 (0.37)	552	-0.13 (0.523)
8.3 cm	911	**0.25 (0.23)**	911	**0.25 (0.23)**	911	0.19 (0.352)	911	0. 2 (0.338)	911	0.18 (0.396)	911	0.19 (0.375)	426	0.11 (0.604)	426	0.10 (0.644)

[1] WL: wavelength, CV: coefficient of variation, SD: standard deviation.

Table S9. The highest Pearson correlation coefficient (R) and *p*-values (in brackets) for the relationship between species richness and the two optical diversity metrics (CV and SD) calculated from $Level_3$ processed data at different sample size for the IT-PD study site. The highest R values are highlighted in bold.

Sub-sample (No. of pixels)	IT-PD 1 mm			
	WL[1]	**CV[1]**	**WL**	**SD[1]**
All pixels	452	0.67 (0.042)	455	**0.67 (0.048)**
500 pixels	554	**0.71 (0.034)**	452	0.66 (0.054)
300 pixels	452	0.68 (0.046)	452	**0.70 (0.036)**
250 pixels	473	**0.63 (0.071)**	490	0.61 (0.079)
200 pixels	452	0.64 (0.065)	452	**0.67 (0.048)**
150 pixels	679	0.62 (0.078)	691	**0.71 (0.033)**
100 pixels	546	**0.69 (0.042)**	706	0.66 (0.054)
50 pixels	412	**0.77 (0.015)**	412	0.77 (0.016)

[1] WL: wavelength, CV: coefficient of variation, SD: standard deviation

Table S10. The highest Pearson correlation coefficient (R) and *p*-values (in brackets) for the relationship between biodiversity indices (species richness, Shannon's index, species evenness, and Simpson's) and the two optical diversity metrics (CV and SD) calculated from $Level_3$ processed data at different sample size for the IT-MBo study site. The highest R values are highlighted in bold.

Sub-sample (No. of pixels)	**Richness**				**Shannon**				**Evenness**				**Simpson**			
	WL[1]	**CV[1]**	**WL**	**SD[1]**	**WL**	**CV**	**WL**	**SD**	**WL**	**CV**	**WL**	**SD**	**WL**	**CV**	**WL**	**SD**
All pixels	930	0.04 (0.852)	679	0.50 (0.011)	911	0.10 (0.652)	688	0.55 (0.004)	911	0.05 (0.816)	688	**0.56 (0.004)**	920	0.15 (0.479)	691	0.40 (0.047)
500 pixels	927	0.03 (0.883)	679	0.35 (0.086)	920	0.13 (0.549)	685	0.42 (0.035)	911	0.09 (0.671)	688	0.43 (0.032)	911	0.07 (0.736)	688	**0.44 (0.029)**
300 pixels	920	0.06 (0.776)	679	0.37 (0.068)	908	0.10 (0.624)	682	0.45 (0.025)	908	0.05 (0.803)	682	0.46 (0.022)	908	0.06 (0.768)	688	**0.47 (0.018)**
250 pixels	412	0.11 (0.614)	679	0.50 (0.012)	679	0.03 (0.899)	685	0.56 (0.003)	679	0.04 (0.861)	685	0.59 (0.002)	679	0.09 (0.684)	685	**0.62 (0.001)**
200 pixels	426	0.16 (0.441)	682	0.48 (0.015)	420	-0.01 (0.948)	685	**0.55 (0.005)**	415	-0.03 (0.905)	685	0.53 (0.006)	415	0.03 (0.892)	685	0.52 (0.007)
150 pixels	418	0.14 (0.507)	682	0.45 (0.024)	914	0.17 (0.429)	682	**0.54 (0.006)**	911	0.13 (0.552)	682	0.53 (0.006)	914	0.12 (0.57)	685	0.53 (0.006)
100 pixels	930	0.03 (0.881)	676	0.36 (0.082)	911	0.09 (0.687)	679	0.41 (0.04)	911	0.07 (0.726)	679	0.43 (0.034)	911	0.05 (0.829)	679	**0.43 (0.034)**
50 pixels	429	0.15 (0.461)	688	0.32 (0.123)	930	0.15 (0.487)	691	0.40 (0.048)	930	0.14 (0.52)	691	**0.42 (0.039)**	412	0.11 (0.593)	688	0.40 (0.045)

[1] WL: wavelength, CV: coefficient of variation, SD: standard deviation

Chapter 4

On the importance of functional diversity links with α and β diversity for the applicability of the optical diversity approach in a subalpine grassland of the Italian Alps

Hafiz Ali Imran [1,2,3*], Karolina Sakowska [6] Damiano Gianelle [1], Duccio Rocchini [4,5], Michele Dalponte [1], Michele Scotton [7] and Loris Vescovo [1]

[1] Research and Innovation Centre, Fondazione Edmund Mach, Via E. Mach 1, 38010 San Michele all'Adige (TN), Italy; damiano.gianelle@fmach.it (D.G.); michele.dalponte@fmach.it (M.D.); loris.vescovo@fmach.it (L.V.)

[2] Department of Civil, Environmental and Mechanical Engineering, University of Trento, Via Mesiano 77, 38123 Trento (TN), Italy

[3] Metacortex S.r.l., Via dei Campi 27, 38050 Torcegno, TN, Italy

[4] Alma Mater Studiorum University of Bologna, Department of Biological, Geological and Environmental Sciences, Via Irnerio 42, 40126 Bologna, Italy; duccio.rocchini@unibo.it

[5] Czech University of Life Sciences Prague, Faculty of Environmental Sciences, Department of Applied Geoinformatics and Spatial Planning, Kamýcka 129, 16500 Prague-Suchdol, Czech Republic

[6] Institute of BioEconomy, National Research Council (IBE-CNR), Via Biasi 75, 38098 San Michele all'Adige, TN, Italy; karolina.sakowska@ibe.cnr.it (K.S)

[7] Department of Agronomy, Food, Natural Resources, Animals and Environment (DAFNAE), Viale dell'Università 16, 35020 Legnaro, PD, Italy; michele.scotton@unipd.it (M.S.)

*** Correspondence:** hafizali.imran@unitn.it; Tel.: +39-389-8921-946

Abstract

As the need for ecosystem biodiversity assessment increases within the climate crisis framework, more and more studies are proposed using remote sensing tools based on the Spectral Variability Hypothesis (SVH) approach to assess biodiversity at various scales. The reflectance measured from the plant canopy encodes fundamental information in different spectral regions about the variability of canopy and leaf structure and other biochemical and biophysical properties of canopy leaves. The SVH implies optical diversity is driven by light absorption dynamics associated with plant traits (PTs) variability (biophysical and biochemical) which is, in turn, determined by species diversity. Based on the SVH hypothesis which links optical, functional, and taxonomic diversity, in this study we examined the relationship between PTs variability (which is an indicator of functional diversity and can be measured by the standard deviation of the biochemical and biophysical PTs) and α-diversity (measured by Shannon's index) at different taxonomic ranks (species, families, and functional groups) at the Monte Bondone grasslands, located in the Trentino province, Italy. Also, the relationship between β-diversity (measured by Jaccard dissimilarity index of the species, families, and functional groups percent cover) and the PTs variability (measured by the Euclidean distances of the biochemical and biophysical PTs) was also investigated. The results of the study showed that the PTs variability, at the α scale, was not correlated with biodiversity. The linear regression analysis showed weak and non-significant correlations between PTs variability and α-diversity for all taxonomic ranks. On the other hand, the

results from the community scale (β-diversity) showed that the variation of some of the investigated biochemical and biophysical PTs was associated with the β-diversity. We used the Mantel test to analyze the relationship between the PTs variability and species β-diversity and the results showed a moderate correlation up to r = 0.50, p = 0.0005 while for the higher taxonomic ranks (family and functional groups) with dry biomass slightly strong correlation up to r = 0.64, p = 0.0001 and r = 0.61, p = 0.0001 was observed. The SVH approach was also tested to estimate β-diversity and we found that spectral diversity calculated by spectral angular mapper (SAM) showed to be a better proxy of biodiversity in the same ecosystem where the spectral diversity failed to estimate α-diversity, this leading to the conclusion that the link between functional and species diversity may be an indicator of the applicability of optical sampling methods to estimate biodiversity.

Keywords: α-diversity; β-diversity; biochemical diversity; distance matrix; Mantel test.

4.1. Introduction

Biodiversity is an essential component to estimate ecosystem functioning and ecosystem services (Record et al., 2020), particularly important within the accelerated climate change context (Schweiger et al., 2018). In the last decades, changes in agricultural practices involving large-scale modification of biogeochemistry by large-scale irrigation, fertilization, and pesticide application, as well as changes in human activities have altered biodiversity patterns, directly affecting the individual species abundances and distributions (Gholizadeh et al., 2020; Record et al., 2020). Such modifications have accelerated biodiversity loss at unprecedented rates and caused a considerable loss of landscape diversity, particularly for grassland ecosystems (Bolch et al., 2020; Gholizadeh et al., 2020; Record et al., 2020; Stevens, 2018). Monitoring plant diversity is always considered challenging because it requires extensive field surveys, which are limited in their ability to sample over large regions. In this context, the effective monitoring and management of the grassland biodiversity can be carried out using its optical properties acquired by remote optical sensors (Reinermann et al., 2020).

Reflectance of the vegetation is the result of the complex physical interactions between incoming solar radiation and canopy surfaces at different spectral regions that encode essential information on vegetation status, function, and structure and is called “spectral signature” (Ma et al., 2020). The reflectance from the visible (VIS) to near-infrared (NIR) spectral region is related to the biophysical and biochemical properties of leaves and canopy structure (Homolova et al., 2013; Ma et al., 2020). Individual plant species respond in their own way to incoming solar radiation according to their pigment, water, biochemical content, and leaf and canopy structure. Based on this, variability in the canopy reflectance might provide information about the presence of different plant species within the measurement footprint. In the literature, this concept is defined as the Spectral Variability Hypothesis (SVH): as the number of plant species increases for a given area, the spectral diversity observed from that area is also expected to increase (Imran et al., 2021; Heumann et al., 2015; Palmer et al., 2002; Rocchini et al., 2004). Different parts of the spectrum characterized by a strong absorbance due to the leaf chlorophyll pigment (particularly the red

domain) showed to be one of the key spectral areas for biodiversity detection (Blanco-Sacristán et al., 2019; Imran et al., 2021).

In the last years, the SVH approach was tested to explore α and β diversity in different ecosystems, such as grasslands (Aneece et al., 2017; Aneece & Epstein 2015; Gholizadeh et al., 2019; Möckel et al., 2016; Wang et al., 2018a) and forests (Khare et al., 2019; Schäfer et al., 2016; Torresani et al., 2019; Zhao et al., 2016), however to our knowledge, no studies have investigated the links between PTs variability and biodiversity in semi-natural grasslands ecosystems. However, few recent studies (Durán et al., 2019; Torresani et al., 2021) found in the literature focused on the relationship between PTs variability, spectral, and plant diversity in forest ecosystems. Durán et al., (2019) combined the imaging spectroscopy and in-situ foliar traits to estimate remotely sensed functional diversity in tropical forests while Torresani et al., (2021) explored the relationship between traits variability retrieved from physical based models and species diversity in a dense coniferous forest. In the later study authors retrieved different parameters of PROSPECT-5 and INFORM models from the canopy spectral data Sentinel-2 images) and used them as optical traits indicators (OTIs, Torresani et al., 2021). Concerning α-diversity, several studies have reported that the SVH can be used as a proxy of plant diversity in various ecosystems and at various spatial scales (Aneece et al., 2017; Aneece & Epstein 2015; Conti et al., 2021; Gholizadeh et al., 2019; Imran et al., 2021; Möckel et al., 2016; Wang et al., 2018a). But at the same time, few studies (Conti et al., 2021; Imran et al., 2021) found that the SVH approach is not straightforward, especially when focusing on the structurally heterogeneous grassland community. The spectral variability is not only due to the leaf and canopy structure, because reflectance is also influenced by biochemical processes, stress, and phenological processes (e.g., senescence, Aneece & Epstein, 2015). To understand if the non-photosynthetic elements and vertical structure of the canopy hamper the optical detection of the species diversity, PTs variations could be used to determine species diversity (Conti et al., 2021; Torresani et al., 2021).

Regarding the β-diversity, the SVH approach is used to estimate species turnover by analyzing distance decay models disclosing floristic dissimilarities (Jaccard and Bray–Curtis) and spectral distances. Marzialetti et al., (2021) studied the relationship between pairwise (Jaccard dissimilarity index, Bray–Curtis dissimilarity index) and spectral pair wise (Euclidean distance) measures and reported the effectiveness of the distance decay model to describe coastal landscape β-diversity on natural as well as on invaded dunes. Similarly, Rocchini et al., (2010) examined the SVH approach to estimate both α and β diversity and reported that the spectral diversity can be used as a proxy to estimate diversity, highlighting some challenges and limitations of this approach. Moreover, in another study, Rocchini et al., (2009) examined the SVH approach to estimate β-diversity at different taxonomic ranks (plant species, genera, and families) at the regional scale and demonstrated that a lower taxonomic rank is important when changes in the taxonomic composition are examined spatially using remotely sensed data. In this study, the authors emphasized that the use of spectral distances for summarizing β-diversity patterns may be more reliable compared to the α-diversity due to this method explicitly taking environmental heterogeneity into account instead of mere spatial distances among sites.

The spectral variability among plants "capture functional differences in chemical, anatomical and morphological traits", and describes the extent and filling pattern of the spectral space occupied by a plant community and thus its functional complexity determined by biodiversity (Schweiger et al., 2018). The applicability of the optical diversity approach to estimate taxonomic diversity is based on the hypothesis (in this study called plant traits (PTs) variability hypothesis – PTVH, Figure 1) that, as optical diversity is determined by PTs (biochemical and biophysical) variability, PTs variability, in turn, should be an indicator of species diversity (Torresani et al., 2021).

PTs variability (also called plant functional diversity, Ma et al., 2020) is defined as the range and dispersion of the biochemical and biophysical PTs including pigment content (e.g., chlorophyll, carotene, xanthophyll), leaf essential elements, and plant leaf traits. The optical diversity approach (Ustin and Gamon, 2010) is based on variation in spectral patterns retrieved by optical remote sensing, which can, in turn, be related to species diversity, genetic diversity, and functional diversity. Relatively few studies have explored the relationships among spectral diversity, PTs diversity, and taxonomic diversity in grassland ecosystems (Zhao et al., 2021) and PTs variability information has been often retrieved by using optical models, making use of OTI, and not by direct biochemical and biophysical PT laboratory measurements (e.g., pigments, element concentration, and PTs) carried out on field samples, in the laboratory (Torresani et al., 2021).

In this study, we examined the relationship between PTs variability measured *in-situ* (expressed standard deviation (SD) at the α scale, and pairwise Euclidean distances between the sampling unit - referred as PTs variability at community scale) and both α-diversity (e.g., within the sampling unit - measured by Shannon's index) and β-diversity (e.g., between samples/pixels variability - measured by Jaccard dissimilarity).

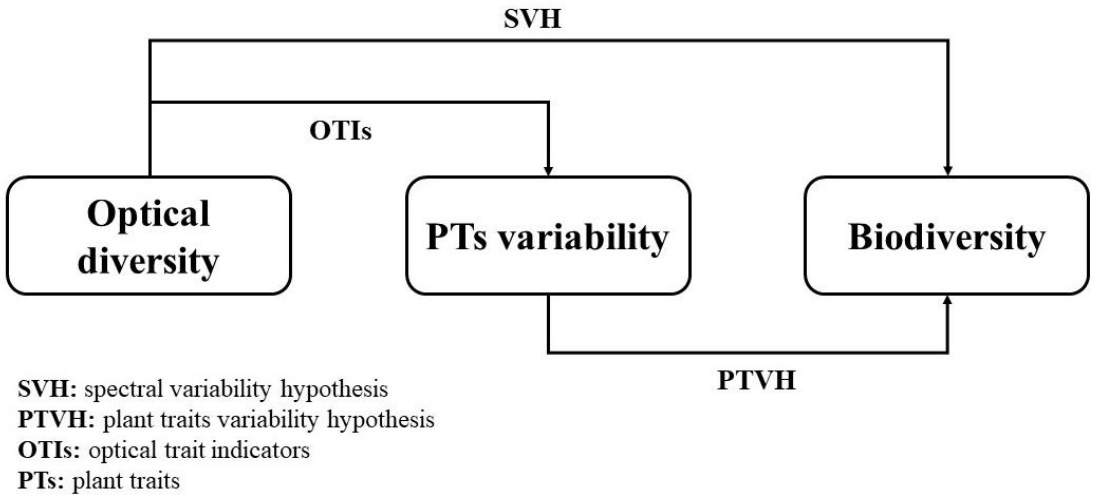

Figure 24. Links between spectral diversity, plant traits (PTs) diversity, and biodiversity

In principle, the aim of this study is to clarify the mechanisms at the basis of the optical diversity approach to estimate biodiversity, analyzing the links between PTs diversity and both α and β diversity. In this context, the specific research objectives of the study were:

(1) To investigate the links between α-diversity and both biochemical and biophysical PTs variability. (2) To explore the links between β-diversity and measured pairwise distances of the biochemical and biophysical PTs. (3) To analyze the performance of spectral diversity proxies to estimate β-diversity using the measured pairwise distances.

4.2. Materials and Methods

4.2.1. Study area

The study area is situated in the Italian subalpine vegetation belt at the Viote del Monte Bondone, Trentino province, Italy (46°00′ N, 11°01′ E; 1480–1550 m a.s.l., IT-MBo, Figure 25). The site is located on a plateau and is managed as an extensive grassland, with low mineral fertilization and one cut per year around mid-July at the green biomass peak time (Sakowska et al., 2019). The vegetation of the area is very heterogeneous, in terms of species richness and canopy structure. The *Sieverso-Nardetum strictae* association covers a high portion of the plateau characterized by short canopies. The *Scorzonero Aristatae-Agrostidetum tenuis* association canopy is generally taller, and it grows on calcareous soils. The latter association includes more productive species, and it can be found in the most fertile and well-exposed areas of the plateau (Sakowska et al., 2019). Initially, 27 randomly distributed vegetation plots were included in the study, but 5 plots were discarded after the quality check of the hyperspectral images. Eventually, in the 22 investigated plots of the IT-MBo plateau, the species richness ranged from 2 to 17 and the species composition and the proportion of each species within the 0.25 × 0.25 m area is presented in Figure 25.

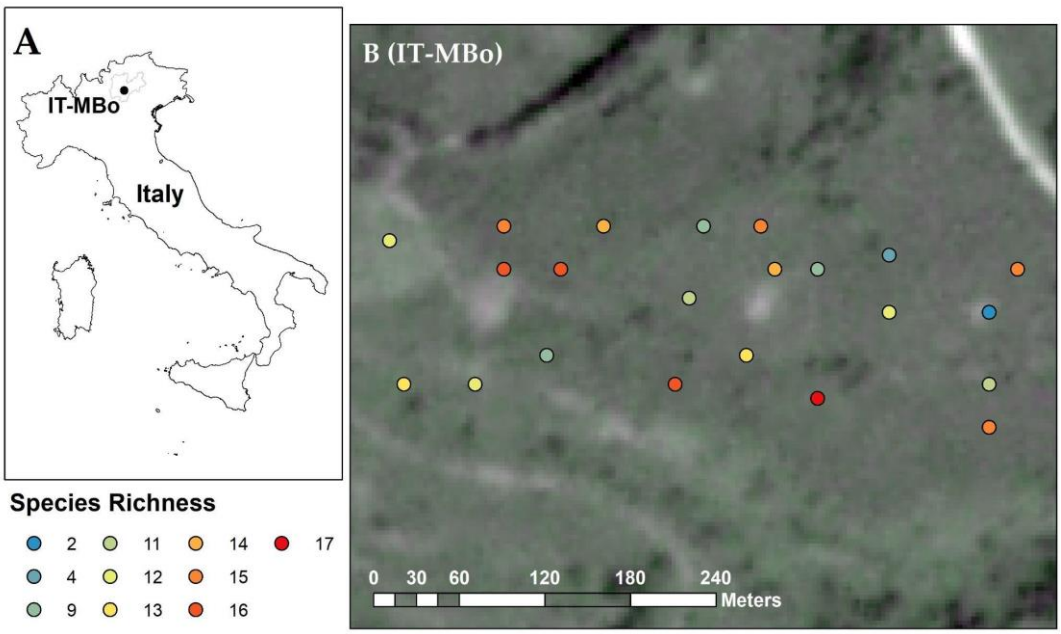

Figure 25. (A) Location of the sample plots in study area (IT-MBo). (B) The plots (n = 22) are located in the natural grassland ecosystem in the Italian Alps (Monte Bondone, Trento, Italy).

4.2.2. Field data collection

The dataset used in this study includes the floristic data, leaf level biochemical and biophysical data, and the top-of-canopy (TOC) spectral data collected on the 22 randomly

distributed georeferenced vegetation plots at the IT-MBo site. To collect the floristic information, vegetation surveys within each region of interest (ROI, 0.25 × 0.25 m) were carried out by a trained person who listed all the species along with their percent cover within the ROIs based on visual estimation (Kent and Coker 1992). The information about the higher taxonomic ranks (species family and functional groups) was also recorded for the plant diversity analysis. In each of the investigated plots, biomass samples were collected at the peak of the growth season using a cutter machine, stored in sealed plastic bags, and kept at low temperatures (4 °C) until further processing. In the laboratory, the sampled biomass was well mixed and divided into two samples of equal weight. The first sample has been dedicated to analyzes beyond the scope of this publication, therefore it was not used in this study. The second sample was furtherly divided into two portions: one portion was used to measure the variability of the biophysical PTs, while the second portion was stored at -80 °C for further determination of the foliar biochemical PTs variability. To calculate the biophysical PTs variability, we divided the first portion into 8 subsamples which were separately weighted to obtain the fresh leaf mass (FLM, g), then scanned to obtain the leaf area (LA, cm^2) and finally oven-dried at 60 °C for 48 h and weighted again to obtain the leaf dry mass (LDM, g). Specific leaf area (SLA) was calculated for each subsample as the ratio of leaf area to leaf dry mass. The variability of the leaf water content (LWC, %) was also determined for each subsample. The LWC was calculated as a difference between the FLM and LDM divided by FLM and multiplied by 100.

The second portion which was stored at -80 °C was used to measure the biochemical PTs variability: the portion was divided into 10 subsamples (in total 220 samples from 22 plots) and the PTs concentration (mg/g dry matter) was determined for each subsample, including chlorophyll-a (chla), chlorophyll-b (chlb), β-carotene (bcar), lutein (lut), neoxanthin (neox), violaxanthin (violax), and antheraxanthin (anther) by using high-performance liquid chromatography (HPLC). The variability of the essential elements (% dry matter) including carbon (C), hydrogen (H), nitrogen (N), sulphur (S), and oxygen (O) was also assessed. The foliar biochemistry analysis were performed by an external laboratory, Celignis Analytical, Limerick, Ireland. PTs concentration was determined by means of the ICS-3000 Ion Chromatography System (Dionex, CA, USA). The analytical procedure is described on the Celignis Analytical website (https://www.celignis.com/package.php?value=78). PTs including elemental components (C, H, N, S, O) were determined using the Vario MACRO Cube elemental analyser (Elementar Analysensysteme GmbH, DE). Further details can be found at the Celignis Analytical website (https://www.celignis.com/package.php?value=19).

We collected TOC level spectral data for the investigated plots (0.25 x 0.25 m) with an imaging spectrometer (SPECIM IQ, Specim Ltd., Oulu, Finland) mounted on a tripod. The canopy height was not consistent between the plots (varied from 0.3 to 1.2 m); therefore, the hyperspectral images were collected approximately 0.7 m from the canopy level to capture a squared footprint of approximately 0.55 × 0.55 m. A metallic or wood frame with dimension 0.25 × 0.25 m was then placed within each image footprint to define the ROIs used for post-processing and spectral diversity metrics calculations.

4.2.3. Measures of species diversity

In this study, two biodiversity metrics - α and β diversity- were used to capture biological variation at different spatial extents.

4.2.3.1. Species α-diversity

α-diversity measures the diversity within sampling units, which are usually spatial subunits within a region or landscape (Shannon, 1948). To calculate the α-diversity (Shannon's index) species percent cover information was used. The Shannon's index was also calculated for the higher taxonomic ranks (species family and functional groups). It was calculated using the following equation:

$$H' = -\sum_{i=1}^{S} p_i \ln(p_i) \qquad (7)$$

where pi is the proportion of individuals that belong to species i and S is the number of species in the sample.

4.2.3.2. Species β-diversity

The β-diversity concept was introduced by Whittaker (1960), who defined it as the variation in biodiversity among local communities. In this study, β-diversity was calculated by generating the pairwise distance matrix based on pairwise dissimilarity methods (Li et al., 2021). The β-diversity was measured for all taxonomic ranks from species to family and function group. β-diversity in field data was analyzed using the Jaccard dissimilarity matrix using plant occurrence (presence/absence data). Jaccard dissimilarity index (J) quantifies the pairwise dissimilarity between vegetation plots as the ratio between the number of species shared between the vegetation plots and the number of species that are unique to each plot (Marzialetti et al., 2021). The formula suggested by Jaccard (1912) implies relativization of the ratio between the number of species in common and the number of species that are unique to each plot.

$$Jaccard\ dissimilariy\ (i,j) = 1 - \frac{a_{ij}}{(a_{ij} + b_i + c_j)} \qquad (8)$$

Where a = number of species shared between i and j vegetation plots, b = number of unique species in the i vegetation plot, c = number of unique species in the j plot.

All biodiversity indices were calculated in R 3.6.1 software (R Core Team, 2019) using the 'vegan' R package (Oksanen et al., 2020). The "vegdist" function was used to calculate species, families, and functional group β-diversity.

4.2.4. Measures of biochemical and biophysical PTs variability

The variability of biochemistry variables and biophysical PTs at α scale measured by using the standard deviation of the biochemical variables included chla, chlb, bcar, lut, neox,

violax, anther, C, H, N, S, O, while the PTs included SLA and LWC. The PTs β-diversity was calculated based on Euclidean distance obtained from the biochemical and biophysical PTs. Euclidean distance represents the geometric distance between two points in multidimensional space. Euclidean distance is bounded by zero when two objects have identical variable values. However, it is not well suited to data such as species abundances (without prior standardizations) due to its lack of a maximum and its high susceptibility to large differences (Hoffmann et al., 2019). Before calculating the pairwise Euclidean distances of biochemical and biophysical PTs, we standardized each of the variables to a mean of 0 and a standard deviation of 1 and then we used the following Euclidean distance matrix by using the "decostand" function of the "vegan" R package (Oksanen et al., 2020).

$$d_{i,j} = \sqrt{\sum (X_{iz} - X_{jz})^2} \quad (9)$$

Where *i* and *j* are the plots being compared and *z* refers to the variables.

4.2.5. Measures of α and β spectral diversity

To measure the spectral α-diversity of each plot, we used the coefficient of variation - CV (i.e., the ratio of the standard deviation to the mean (Blanco-Sacristán et al., 2019; Wang et al., 2018a). In this study, the CV was calculated by averaging the CV for each wavelength from 411 to 930 nm. Higher CV values correspond to higher spectral diversity. The CV was calculated using the following equation:

$$\mathrm{CV}_{\mathrm{image}} = \frac{\sum_{\lambda=411}^{930} \left(\frac{\mathrm{std}\ (\rho_\lambda)}{\mathrm{mean}\ (\rho_\lambda)} \right)}{\mathrm{number\ of\ bands}} \quad (10)$$

where ρ_λ represents the reflectance value at wavelength λ and std (ρ_λ) and mean (ρ_λ) indicate the standard deviation and mean value of the reflectance at wavelength λ, respectively.

To compare the spectral diversity to the taxonomic β-diversity index, spectral β-diversity was calculated using the Spectral Angle Mapper (SAM, Kruse et al., 1993). The SAM is a spectral classification technique which measures the angle between two spectral signatures and treats them as vectors. Similar spectra have low SAM values, while more diverse spectra have higher SAM values. SAM was calculated by using the "dist.speclib" function of the "hsdar" R package (https://cran.r-project.org/web/packages/hsdar/hsdar.pdf) using the following equation:

$$SAM = \cos^{-1}\left(\frac{\sum_{i=1}^{sb} t_i r_i}{\sqrt{\sum_{i=1}^{sb} t_i^2} \sqrt{\sum_{i=1}^{sb} r_i^2}}\right) \quad (11)$$

sb is the number of bands in Speclib. t_i and r_i are the reflectance of target and reference spectrum in band i, respectively.

4.2.6. Statistical analyses

To analyze the species distribution within the plot, the percentage of the individual species within the plot was visualized as a stacked bar graph. The descriptive analysis of biochemical and biophysical PTs variability is summarized in Table S11-S13 in Supplementary Materials where the minimum, maximum, and SD of each biochemical and PTs are reported. To analyze the SVH performance for α-diversity, we analyzed the linear relationship between α-diversity (measured by Shannon's index) for different taxonomic ranks (species, family, and functional groups) and biochemical and PTs variability (measured by SD) of each plot.

To test the SVH approach for β-diversity, we used the Mantel permutation test (Mantel, 1967) to determine relationships between biochemical and biophysical β-diversity metrics calculated from the Euclidean distances of all the 12 biochemical PTs (including 2 chlorophyll pigments: chla and chlb; 1 carotene: bcar; 4 xanthophyll pigments: lut, neox, violax, anther; 5 essential elements: C, H, N, S, and O), and 3 biophysical PTs (SLA, LWC, and dry biomass) and taxonomic β-diversity measured by Jaccard dissimilarity index. The relationship between spectral β-diversity measured as SAM and taxonomic β-diversity was also analyzed by using Mantel statistics. All statistical analyses were performed with the statistical software R (version 3.6.1) (R Core Team, 2019).

4.3. Results

The species distribution in the investigated plots expressed as a proportion (in percentage) is presented in Figure 26. The proportions of the species within the plots of the study area showed a high species diversity in the grassland ecosystem. The highest number of recorded species within the 0.25 x 0.25 m area was 17, it was observed in plot 09 where the dominating species were *Festuca nigrescens Lam.* and *Leontodon hispidus L.* with a contribution of appro*ni*ximately 18% and 20%, respectively. In the plot 01, 12, and 18, 16 species were observed, and *Agrostis tenuis Sibth.*, *Phleum alpinum L.*, and *Festuca nigrescens Lam.* accounted with the highest proportion of species composition of approximately 25%, 20%, and 35%, respectively. In general, a high number of species was observed -considering the relatively small area compared to the other studies (Aneece et al., 2017; Peng et al., 2019; Wang et al., 2018a). Among the 22 investigated plots, only 2 plots (20 and 22) were showing less than 5 species. In plot 20 there were 4 species observed, where *Epilobium angustifolium L.* covered about 95% of the area, while *Epilobium angustifolium L.*, *Carex sp.*, *Euphrasia rostkoviana.*, and *Agrostis tenuis Sibth.*, covered 4%, 1%, and 0.1% of the area respectively. In plot 22 there were only 2 species, and *Agrostis tenuis Sibth.* covered almost the whole area (99% proportion), while *Chaerophyllum hirsutum L.* covered only 1% of the area. The distribution of the family and functional group taxonomy level is presented in Appendix B Figure B1 and Figure B2, respectively.

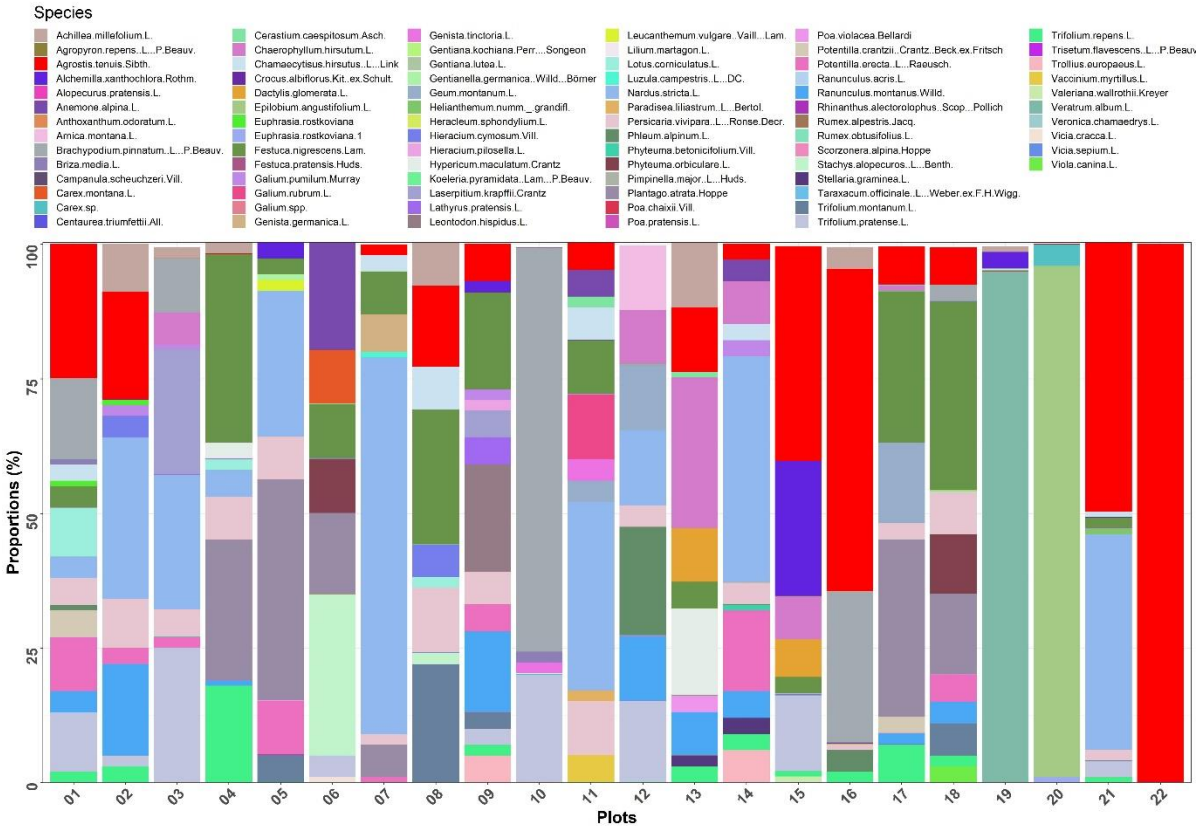

Figure 26. Species distribution (in %) within each plot.

4.3.1. Biochemical and biophysical PTs variability across the study plots

The variation of the biochemical and biophysical PTs among the 22 investigated plots in the grassland ecosystem expressed as SD measured from the average PTs value of each plot are presented in Figure 27. The chlorophyll PTs (chla and chlb) showed high variation compared to the carotene (bcar) and xanthophyll PTs (lut, neox, violax, and anther). Out of the chlorophyll pigments, chla showed the highest SD range and showed to be a highly heterogeneous metric (Figure xx, panel A). In the xanthophyll pigments, we observed some outlier values in the SD, but the median SD was always lower than the median SD of chla and bcar. Out of the biochemical elements, Nitrogen showed the highest variation within SD varying from 0.24 to 0.44 (Figure 27, panel A). The variation in the biophysical PTs including SLA and LWC is also presented in Figure 27, panel B, where the SLA showed a higher variation compared to the LWC in the study area.

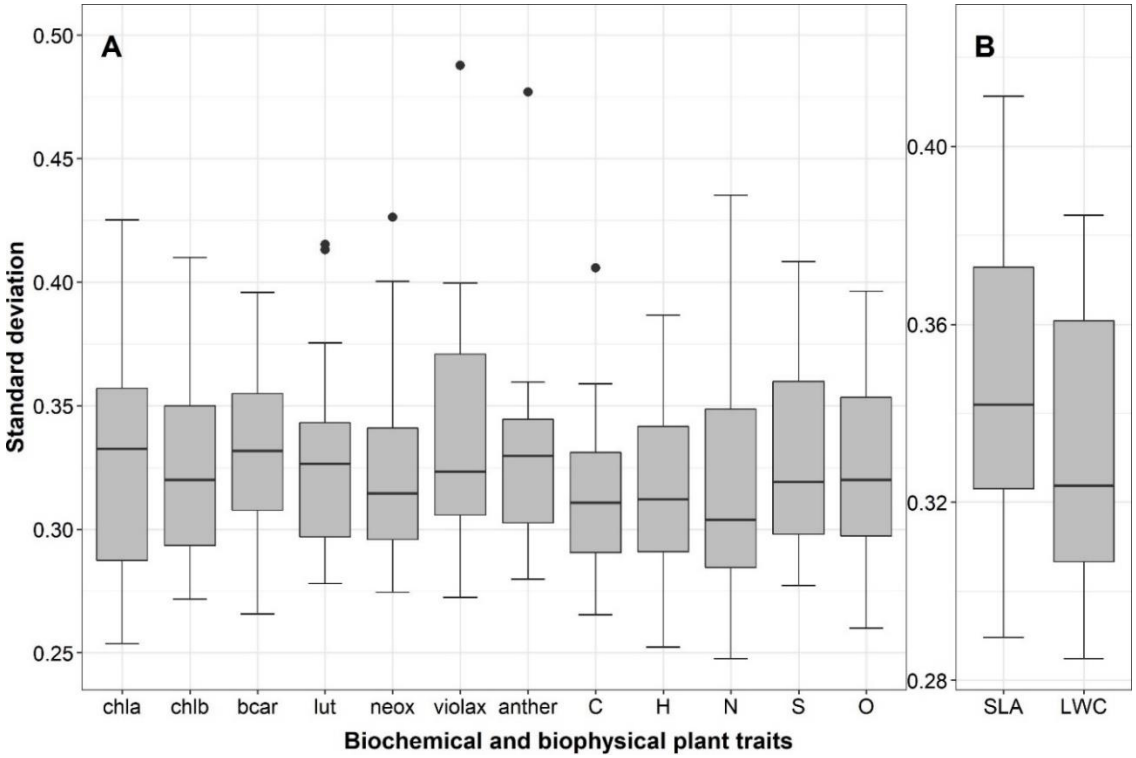

Figure 27. Box plots of the biochemical (panel A) and biophysical (panel B) plant traits (PTs) standard deviation (SD) among the investigated plots measured from the 10 subsamples of PTs in each plot. The grey box represents the inter-quartile range, with a horizontal line showing the median. Each whisker extends to the highest value that is within 1.5 times the inter-quartile range. The black points indicate outliers values in the PTs measurement (Wickham, 2007). The abbreviations of the x axis labels are: chla (chlorophyll a); chlb (chlorophyll b); bcar (β-carotene); lut (lutein); neox (neoxanthin); violax (violaxanthin); anther (antheraxanthin); C (carbon); H (hydrogen); N (nitrogen); S (sulphur); O (oxygen); SLA (specific leaf area); LWC (leaf water content).

4.3.2. α-diversity and PTs diversity

A weak and non-significant linear relationship was observed between PTs variability (at local scale, measured as SD) and species α-diversity (measured as Shannon's index) for all three taxonomy levels (Table 10). The results are very similar to the ones obtained with spectral diversity metrics at the local scale (which also failed to estimate α-diversity in the same ecosystem) which were presented previously in Imran et al., (2021). All the metrics based on biochemical PTs variability failed to estimate biodiversity and hardly any of the metrics was correlated with α-diversity with an R^2 value greater than 0.10 (Table 10). The biophysical PTs (SLA and LWC) variability at the local scale was also not significantly correlated with α-diversity.

Table 10. Summary of linear regressions for α-diversity at three taxonomy levels (Shannon's index) vs. biochemical and biophysical variability (measured as standard deviation). Values outside parentheses represent the R^2 (coefficient of determination), while values inside parentheses indicate the p-value.

Biochemical and biophysical PTs	**Shannon's index**		
	species	**families**	**functional group**
	Biochemical PTs (mg/g dry mass)		
chlorophyll a	0.04 (0.39)	0.01 (0.73)	0.02 (0.57)
chlorophyll b	0.00 (0.88)	0.02 (0.52)	0.00 (0.95)
β-carotene	0.00 (0.95)	0.00 (0.89)	0.03 (0.43)
lutein	0.10 (0.70)	0.00 (0.86)	0.00 (0.90)
neoxanthin	0.01 (0.75)	0.00 (0.88)	0.02 (0.53)
violaxanthin	0.01 (0.63)	0.00 (0.98)	0.02 (0.50)
antheraxanthin	0.00 (0.83)	0.00 (0.92)	0.00 (0.98)
carbon	0.10 (0.30)	0.04 (0.38)	0.02 (0.43)
hydrogen	0.01 (0.63)	0.00 (0.81)	0.02 (0.58)
nitrogen	0.03 (0.44)	0.01 (0.72)	0.10 (0.16)
sulphur	0.00 (0.82)	0.02 (0.54)	0.00 (0.78)
oxygen	0.03 (0.46)	0.00 (0.88)	0.00 (0.77)
	Biophysical PTs		
specific leaf area	0.01 (0.70)	0.00 (0.98)	0.10 (0.20)
leaf water content	0.01 (0.68)	0.10 (0.28)	0.10 (0.18)

4.3.3. Biochemical and biophysical PTs distances vs species turnover

The correlation between Jaccard species dissimilarities vs. biochemical and biophysical PTs Euclidean distance showed that the taxonomic β-diversity is correlated with PTs variability among plots, at the spatial scale. For taxonomic β-diversity at the species level, the variation of the chlorophyll PTs (chla and chlb) showed a higher significant correlation with β-diversity (r = 0.5, p = 0.0002 and r = 0.46, p = 0.0014, Figure 28, panel A and B) compared to beta carotene and xanthophyll PTs (Figure 28, panel C and G). The strength of the correlation between the taxonomic β-diversity and biochemical PTs variability varied depending on the analyzed PT. Some PTs, such as chla and chlb, lut, neox, and violax, associated with the taxonomic β-diversity with an r => 0.3, while other PTs, such as bcar and anther, were not linked with the β-diversity. The correlations between the variation of leaf

element content and Jaccard dissimilarity also gave some evidence of the connection between PTs diversity and taxonomic β-diversity. Among the investigated leaf elements, the strongest correlation with β-diversity was found for N and O (r = 0.48, p = 0.0002 and r = 0.38, p = 0.004, respectively; Figure 28, panel J and L). In case of the other elements, the correlation with taxonomic β-diversity was weak or negligible: for example, C showed an r value of = 0.21 (Figure 28, panel H) while H, and S showed values around zero (Figure 28 panel I and K).

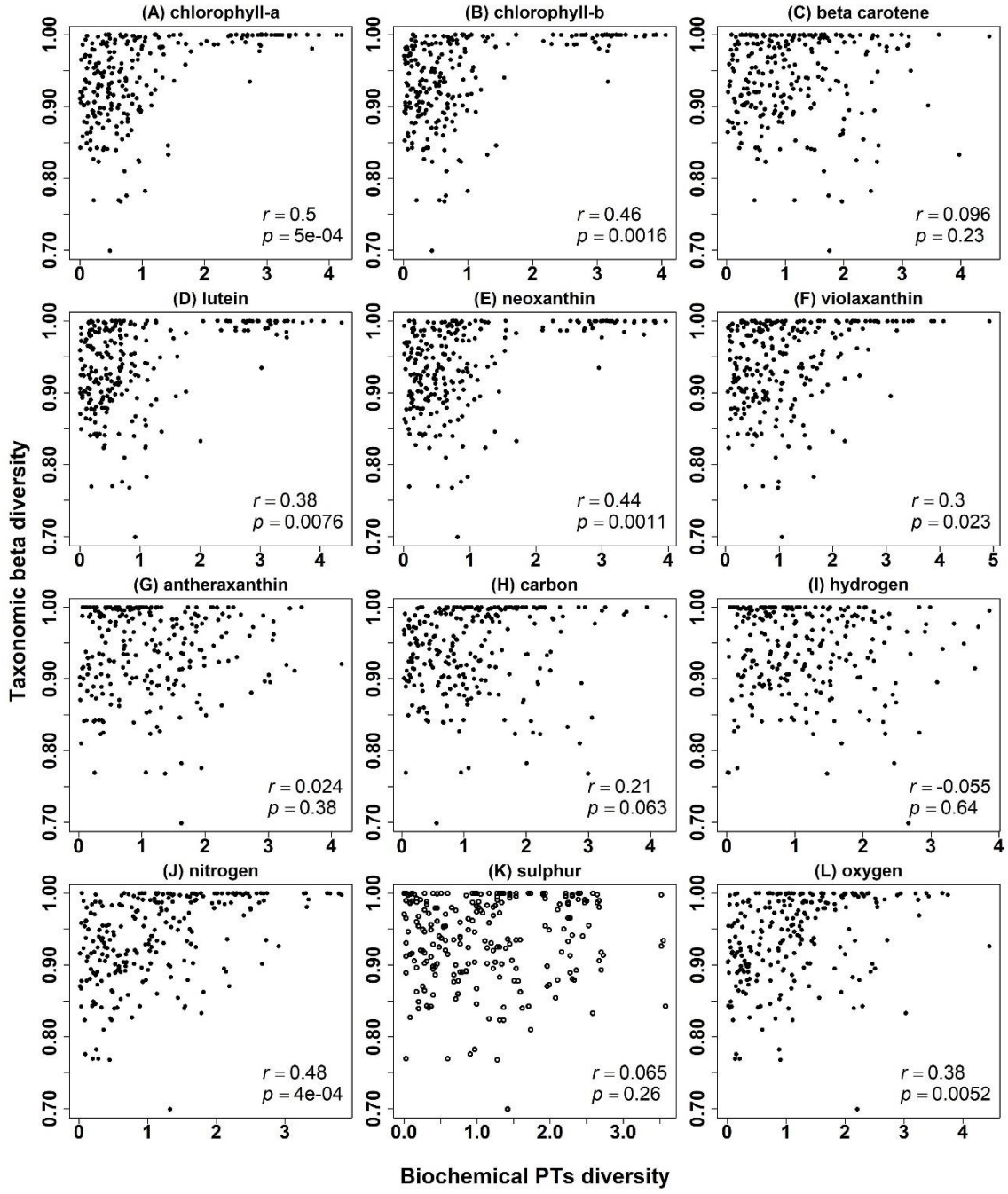

Figure 28. Mantel correlations between the biochemical PTs diversity (measured by Euclidean distance of various PTs) and species β-diversity (measured by Jaccard dissimilarity index).

The correlation between biophysical PTs diversity calculated from the Euclidean distances and the taxonomic β-diversity was moderate, (r = 0.42, p = 0.039) when the canopy dry biomass variability was related to β-diversity, while the variability of SLA showed a weaker correlation with an r = 0.29 (p = 0.0011; Figure 29, panel A). The biophysical LWC diversity, on the other hand, showed almost no correlation with taxonomic β-diversity with an r = -0.075, p = 0.70.

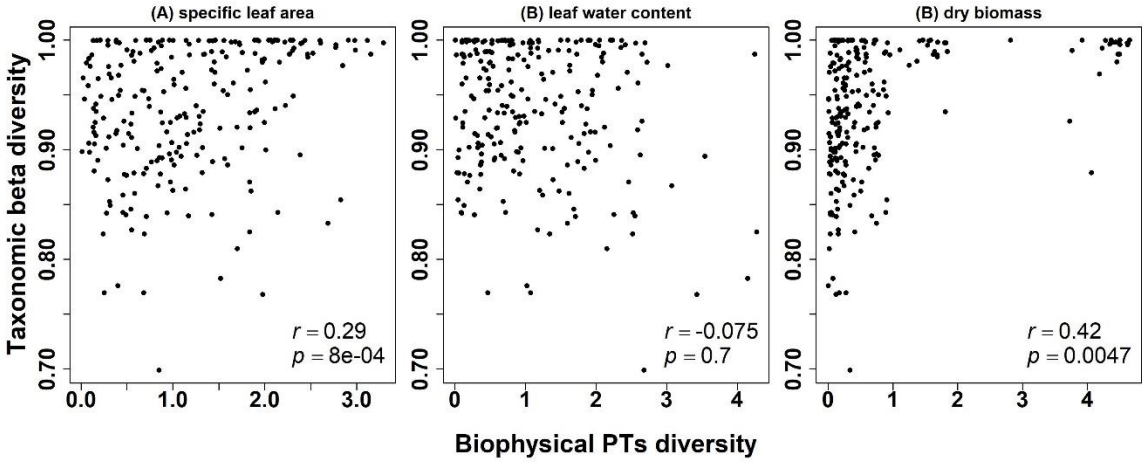

Figure 29. Mantel correlations between the biophysical PTs diversity (measured by Euclidean distance of biophysical PTs) and species β-diversity (measured by Jaccard dissimilarity index).

The correlations between β-diversity at different higher taxonomic levels (families and functional groups) and both biochemical and biophysical PTs variability are presented in Table 11. The Mantel r values between Jaccard species dissimilarities and biochemical and biophysical PTs Euclidean distance showed a similar correlation compared to the taxonomic β-diversity at the species level. A slight drop in r-values was observed for the dissimilarity matrices calculated from the species family-level data and a further decrease in r values was observed when considering dissimilarity matrices at higher taxonomy level (functional group). Among the investigated biochemical PTs, chla and lut showed the highest correlations with the taxonomic β-diversity at the family rank (r values of 0.33, p = 0.02 and r = 0.32, p= 0.02) compared to chlorophyll and other xanthophyll PTs which showed r values < 0.30. At higher taxonomic levels (functional groups) a further decrease in r values was generally observed; for example, chla and lut showed r values of 0.19 (p = 0.09) and 0.27 (p = 0.04), respectively.

Among the xanthophyll PTs, violax, and anther showed an overall weak and non-significant correlation with taxonomic β-diversity at both taxonomic ranks (families and functional group). The nitrogen and oxygen biochemical elements variability showed a moderate correlation for the taxonomic β-diversity for species family rank with an r value r = 0.44, p = 0.001 and r = 0.52, p = 0.0001 while a slight decrease in the r values was observed when the higher taxonomic rank (functional groups) was considered. The biophysical PTs diversity measured by PTs Euclidean distances between plots showed a weak correlation except the dry biomass which showed a strong significant correlation with an r value r = 0.64,

p = 0.0001 and r = 0.61, p = 0.0001 for both taxonomic ranks families, and functional groups respectively.

Table 11. Summary of Mantel correlations for β-diversity at higher taxonomy levels (measured by Jaccard dissimilarity index) vs. biochemical and biophysical variability (measured as Euclidean distance). In the brackets the p-value is presented.

Biochemical and biophysical PTs	**Shannon's index**	
	families	**functional groups**
Biochemical PTs (mg/g dry mass)		
chlorophyll a	0.33 (0.02)	0.19 (0.09)
chlorophyll b	0.29 (0.03)	0.24 (0.05)
β-carotene	0.32 (0.02)	0.27 (0.04)
lutein	0.28 (0.03)	0.30 (0.02)
neoxanthin	0.28 (0.03)	0.17 (0.11)
violaxanthin	0.16 (0.13)	-0.05 (0.58)
antheraxanthin	0.03 (0.36)	-0.10 (0.83)
carbon	0.14 (0.14)	0.12 (0.16)
hydrogen	0.08 (0.25)	0.01 (0.44)
nitrogen	0.44 (0.001)	0.29 (0.02)
sulphur	0.26 (0.01)	0.30 (0.004)
oxygen	0.52 (0.0001)	0.49 (0.0002)
Biophysical PTs		
specific leaf area	0.17 (0.03)	0.14 (0.05)
leaf water content	-0.06 (0.64)	0.09 (0.22)
dry biomass	0.64 (0.0001)	0.61 (0.0001)

4.3.4. Spectral distances vs species turnover

The analysis of the correlation between spectral β-diversity measured by the SAM between the average reflectance of the study plots and taxonomic β-diversity measures at different taxonomic ranks is presented in Figure 30. The correlation between spectral diversity and taxonomic β-diversity showed a significant correlation with r value of 0.48, p = 0.0018 for the species taxonomic rank while a slightly decrease in r values between two metrics were observed for the two other taxonomic ranks (families and functional groups) with r = 0.47, p = 0.002 and r = 0.41, p = 0.001, respectively.

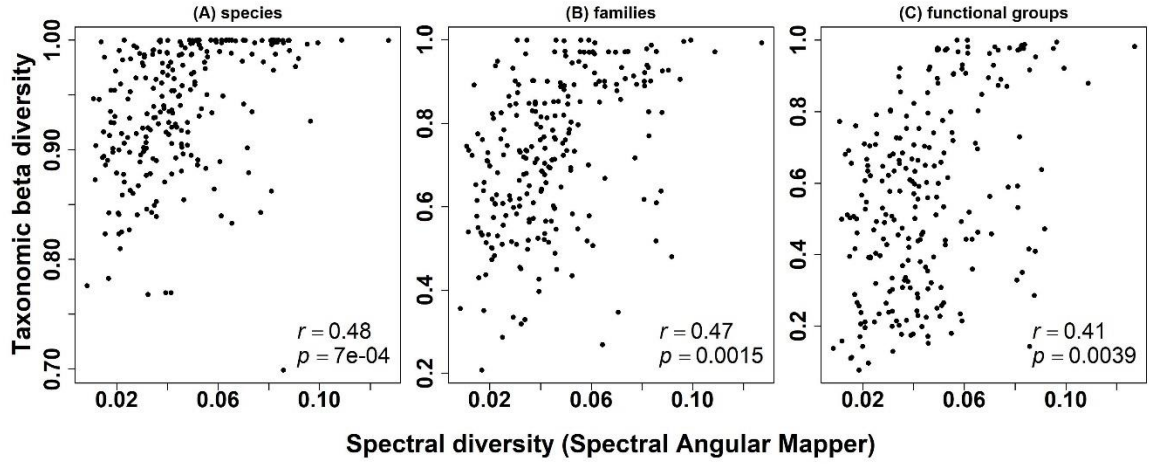

Figure 30. Mantel correlations between the spectral diversity (measured by spectral angular mapper of average reflectance of each plot) and species β-diversity (measured by Jaccard dissimilarity index).

4.4. Discussion

The potential of the spectral diversity approach to estimate the taxonomic diversity at α and β diversity scales has been recently explored, and many authors (Aneece & Epstein, 2015, Aneece et al., 2017, Wang et al., 2018a, Peng et al., 2019, Marzialetti et al., 2021) used the SVH approach to study either man-made simpler ecosystems or relatively low diverse plant communities. In such low-diverse plant communities, authors claimed the successful estimation of both α and β taxonomic diversity (Aneece et al., 2017; Aneece & Epstein, 2015; Marzialetti et al., 2021; Peng et al., 2019; Wang et al., 2018a). However, the SVH approach has also been criticized for being unstable and not reliable in every context, and this demonstrated to be potentially due to the differences in the level of heterogeneity of in the investigated ecosystems (Conti et al., 2021; Imran et al, 2021; Schmidtlein & Fassnacht, 2017) although the diversity dynamics for complex and high-biodiversity ecosystems are still not completely clear. The structurally-heterogeneous canopy modifies optical diversity patterns because high structural diversity and complex vertical structure, in these canopies, may express high spectral diversity even when low species diversity, and vice versa (Conti et al., 2021; Imran et al., 2021). So, according to these studies, optical diversity may not be able to detect PTs variability (functional diversity), and thus biodiversity.

In order to better understand the mechanisms behind the relationship between spectral diversity and biodiversity, in this study we used the PTs variability approach (PTVH) to bridge spectral diversity to biodiversity. To our knowledge, the present study is the first work exploring the links between *in-situ* PTs variability and species diversity at both the α and β scales. We found that the relationship between PTs variability (which expresses functional diversity) and species diversity strongly varies across the diversity scales. Presumably due to the complex nature of the canopies in the investigated ecosystem, we found weak correlations between PTs variability and taxonomic α-diversity. This result was unexpected, and it is suggesting that the lack of correlation between optical diversity and taxonomic α-diversity may be not only due to the fact that heterogeneous canopy modifies optical diversity patterns (as demonstrated by Conti et al., 2021 and Imran et al., 2021), but also to the fact that PTs

diversity (determining optical diversity) is not always associated with α-diversity. Based on this, variability in the canopy reflectance is expected to provide information about the presence of different plant species within the measurement footprint as each species is supposed to respond in a different way to incoming solar radiation according to their pigment, water, biochemical content, and leaf and canopy structure. According to our results, such biochemical and biophysical variability cannot always be associated with α-diversity.

The overall weak relationship between PTs variability and species α-diversity suggested that the relationship between PTs and species diversity may be impaired by other sources of variability such as e.g., the presence of heterogeneous elements (e.g., flowers, stems, leaves, and dead material) in the biomass samples. The presence of the non-photosynthetic elements is one of the canopy characteristics which might hamper not only the optical diversity approach to estimate diversity (as shown by Imran et al., 2021), but also the PTs variability link to the α-diversity. Another possible reason for the weak correlation between ecosystem functional diversity (estimated by PT variability) and α-diversity may be related to the PT variability sampling strategy adopted in this study. To this regard, more studies are needed to verify this hypothesis.

The results of the study showed that the relationship between PTs variability and biodiversity varied across the biodiversity spatial scales. The analysis of the Mantel test showed that a moderate correlation can be found between the PTs variability (measured by Euclidean distances of the biochemical variables among the sampling units) or spectral diversity (measured by SAM among the plots) with taxonomic β-diversity (measured by Jaccard dissimilarity among the plots) at IT-MBo grassland site. The PTs variability (chla, chlb, lut, neox, violax, N, O, and dry biomass) could be associated with species distance in structurally heterogeneous plant communities. Our analysis showed that the variability at the spatial scale of leaf N content (mg/g dry mass) among the plots (as measured by pairwise Euclidean distances) is correlated ($r = 0.48$) with β-diversity (calculated using species pairwise distance matrix). More specifically, N content (in this unfertilized grassland) was directly correlated with β-diversity, differently from what suggested by Humbert for fertilized grasslands (Humbert et al., 2016).

The relationship between the variability of chlorophyll traits (chla and chlb) and β-diversity are in line with a recent study of Torresani et al., (2021) where PTs variability links with biodiversity were analyzed in forest ecosystems. The variation of Cbrown, Car and Cab was shown to be an accurate proxy of tree species diversity (Torresani et al., 2021) although uncertainties in the estimation of leaf chemistry were deducted from physical model inversion and not (like in our study) from direct observations.

Our study confirmed the recent findings of Zhao et al., 2021 concerning the ability of estimating ecosystem productivity from the variation of grassland leaf traits. The optical diversity approach, investigating the spectral variation of the canopy reflectance, is able to provide significant information on productivity, functional diversity and, in turn, on grassland biodiversity (Imran et al., 2021 and Sakowska et al., 2019). However, our study confirmed that most assessments of diversity (from remote observations or from laboratory

measurements of *in-situ* samples) are rather uncertain and more studies need to be performed to quantify such uncertainties.

Our study is significantly contributing to the analysis and explanations of the limits of the optical diversity approach that describes the extent and filling pattern of the spectral space occupied by a plant community. Such approach is expected to describe ecosystem functional complexity Schweiger et al., 2018) which stems from biodiversity. But why is the optical approach sometimes not showing satisfactory performances for biodiversity estimations in e.g., high biodiversity and highly heterogeneous ecosystems (as in Imran et al., 2021)? Our results are only preliminary -considering the small study area-, but they indicate that this might be partly due to the complex relationships between functional diversity and biodiversity.

4.5. Conclusions

In several studies (Rocchini et al., 2019; Rocchini et al., 2018; Rocchini et al., 2016; Wang et al. 2018a; Wang & Gamon, 2019) the relationship between spectral diversity and plant diversity has been studied, but it has also been demonstrated to be unstable and not reliable in every context (Schmidtlein & Fassnacht, 2017, Imran et al., 2021). These contradictory findings might be due to site-specificity and in particular to the differences in the level of heterogeneity of the investigated ecosystems, which may hamper the ability to detect PTs variability (functional diversity). On the other hand, it is not clear whether, in such heterogeneous ecosystems, functional diversity, expressed as PTs variability directly measured *in-situ*, is linked to biodiversity.

In this paper, we demonstrated that: i) functional diversity (expressed as PTs variability) is not correlated with α-biodiversity in a species-rich semi-natural subalpine grassland site where, in previous studies, the optical diversity approach was not able to reliably detect α-biodiversity ii) functional diversity at the spatial scale (for chlorophyll, xanthophyll and nitrogen content) is linked with β-biodiversity iii) β-diversity has a statistically significant relationship with spectral variability since plant compositional turnover monotonically increases with increasing spectral distance among sites.

Our preliminary results indicate that the poor performance of optical diversity proxies in estimating biodiversity in structurally heterogeneous grasslands might be partly due to the complex relationships between functional diversity and biodiversity, besides the impossibility to detect functional diversity (and then, in turn, species diversity) with spectral proxies.

4.6. Appendix B

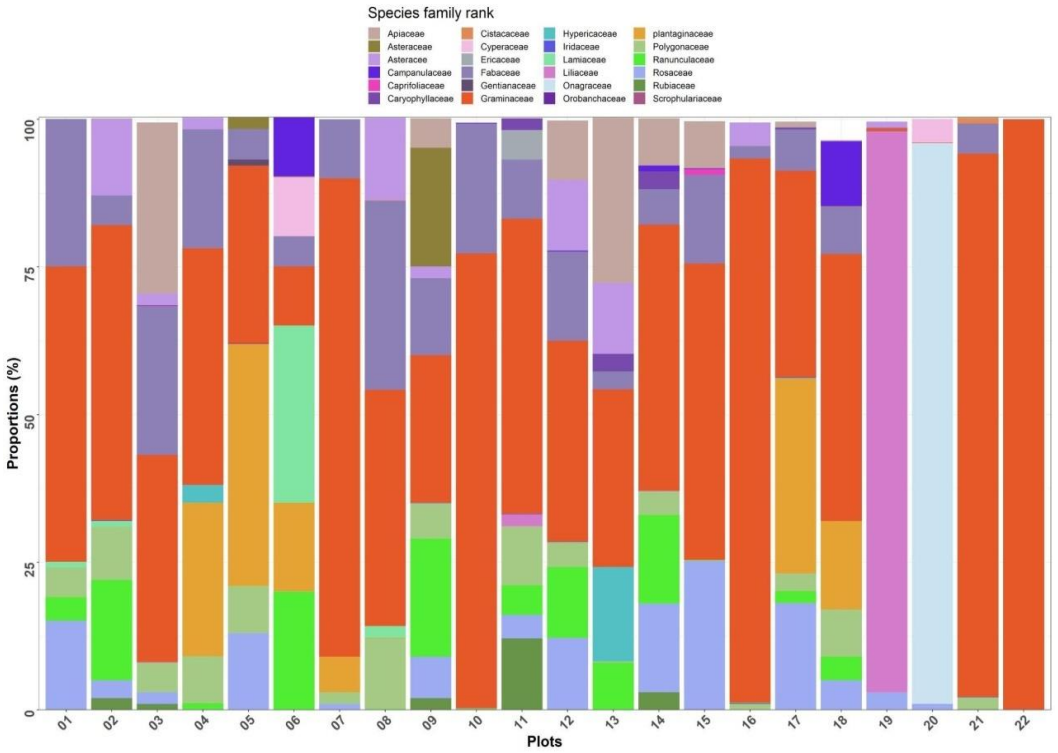

Figure B1. Families distribution (in %) within each plot.

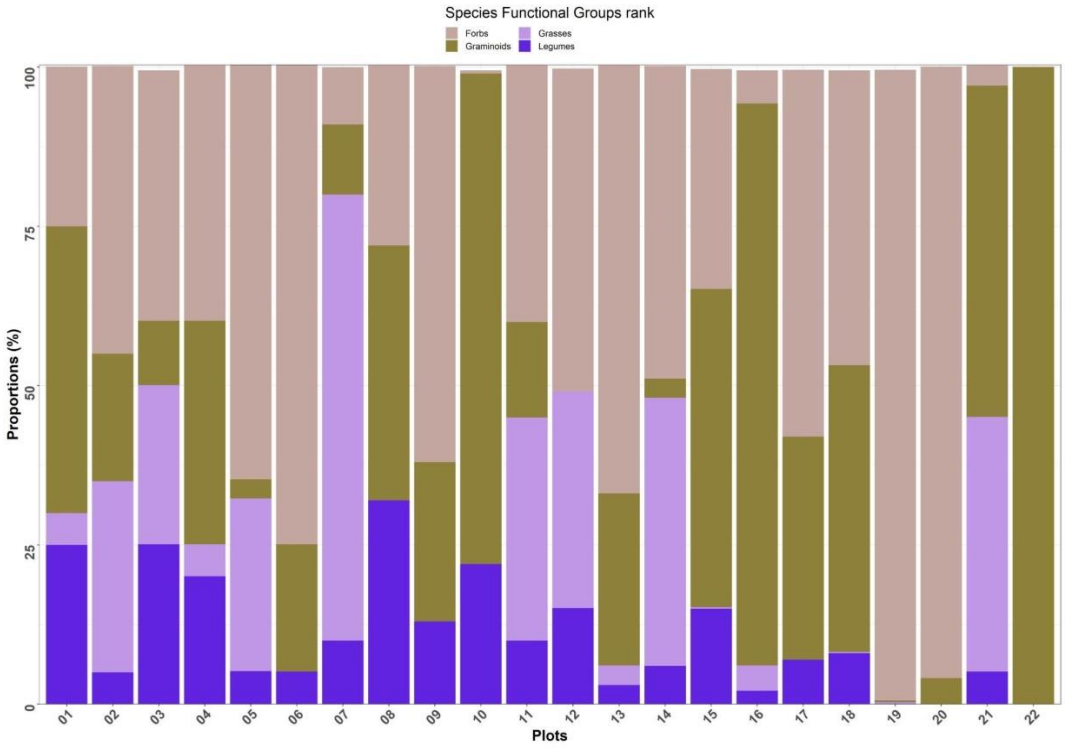

Figure B2. Functional groups distribution (in %) within each plot.

4.7. Supplementary material

Table S11. Descriptive statistics (Min: minimum, Max: maximum, SD: standard deviation) of the biochemical plant traits (chlorophyll, β-carotene, and xanthophyll pigments).

Plots	chlorophyll a			chlorophyll b			β-carotene			lutein			neoxanthin			violaxanthin			antheraxanthin		
	Min	Max	SD	Min	Max	SD	Min	Max	SD	Min	Max	SD	Min	Max	SD	Min	Max	SD	Min	Max	SD
01_02	1.52	2.98	0.43	1.44	2.24	0.27	0.64	1.07	0.14	0.21	0.40	0.06	0.05	0.32	0.02	0.08	0.13	0.02	0.02	0.11	0.01
02_02	1.05	3.28	0.62	1.21	2.57	0.42	0.54	1.15	0.19	0.26	0.43	0.04	0.03	0.11	0.02	0.00	0.16	0.05	0.00	0.03	0.01
04_01_R	1.99	3.28	0.37	0.95	3.15	0.64	0.49	1.79	0.38	0.29	0.43	0.04	0.06	0.11	0.02	0.00	0.16	0.04	0.00	0.03	0.01
05_02	1.85	3.31	0.50	0.73	3.15	0.20	0.18	1.79	0.05	0.24	0.42	0.06	0.06	0.11	0.02	0.08	0.16	0.02	0.01	0.03	0.00
06_02	1.54	3.31	0.52	0.90	1.56	0.18	0.22	0.35	0.04	0.20	0.41	0.06	0.05	0.11	0.01	0.09	0.14	0.02	0.02	0.03	0.00
07_02	1.91	3.18	0.22	0.91	1.56	0.17	0.23	0.35	0.04	0.23	0.40	0.03	0.06	0.09	0.01	0.08	0.13	0.01	0.02	0.03	0.00
08_02	1.76	2.50	0.24	0.90	1.58	0.24	0.21	0.35	0.05	0.25	0.33	0.03	0.05	0.08	0.01	0.09	0.12	0.01	0.02	0.03	0.00
09_02	0.57	2.73	0.92	0.68	1.58	0.24	0.18	0.35	0.04	0.07	0.35	0.11	0.01	0.08	0.03	0.02	0.11	0.03	0.01	0.05	0.01
10_02	1.20	3.10	0.62	0.80	1.43	0.11	0.19	0.31	0.02	0.16	0.35	0.06	0.03	0.11	0.02	0.05	0.14	0.03	0.01	0.05	0.00
11_02	1.59	3.43	0.67	0.77	1.16	0.10	0.19	0.27	0.02	0.20	0.39	0.07	0.05	0.13	0.03	0.08	0.16	0.03	0.02	0.03	0.01
12_02	0.98	3.43	0.29	0.25	1.38	0.46	0.06	0.30	0.10	0.16	0.39	0.05	0.04	0.13	0.01	0.03	0.16	0.02	0.01	0.03	0.00
13_02	1.21	2.40	0.35	0.60	1.50	0.28	0.14	0.33	0.06	0.15	0.32	0.05	0.04	0.09	0.01	0.04	0.10	0.02	0.01	0.02	0.00
14_02	0.25	3.28	0.83	0.83	1.80	0.35	0.17	0.38	0.07	0.13	0.33	0.06	0.02	0.12	0.03	0.00	0.10	0.01	0.00	0.02	0.00
16_02	1.35	3.28	0.64	0.45	1.80	0.12	0.14	0.38	0.03	0.18	0.40	0.07	0.04	0.12	0.02	0.01	0.12	0.03	0.01	0.03	0.01
17_02	0.12	3.23	0.80	0.58	1.13	0.16	0.14	0.30	0.04	0.17	0.40	0.05	0.02	0.10	0.02	0.00	0.12	0.04	0.00	0.03	0.01
18_02	1.19	2.33	0.41	0.67	1.84	0.36	0.16	0.40	0.07	0.16	0.34	0.05	0.04	0.08	0.01	0.05	0.11	0.02	0.01	0.03	0.01
19_02	1.27	3.58	0.66	0.67	1.84	0.32	0.16	0.40	0.07	0.17	0.47	0.09	0.04	0.12	0.02	0.06	0.13	0.02	0.01	0.03	0.00
20_02	1.54	3.58	0.37	0.64	1.62	0.21	0.15	0.36	0.05	0.22	0.47	0.06	0.05	0.12	0.01	0.07	0.17	0.03	0.02	0.03	0.01
T_02	0.67	2.59	0.37	0.62	1.31	0.19	0.15	0.31	0.04	0.10	0.38	0.06	0.02	0.08	0.01	0.04	0.17	0.03	0.01	0.03	0.01
T_03	2.47	7.14	1.18	0.62	1.66	0.31	0.14	0.39	0.07	0.17	0.60	0.15	0.09	0.29	0.05	0.02	0.26	0.07	0.00	0.03	0.01
T_05	3.82	7.14	0.55	0.62	1.66	0.18	0.19	0.39	0.05	0.17	0.60	0.10	0.13	0.29	0.02	0.16	0.26	0.02	0.02	0.03	0.00
T_10_B	1.15	5.78	0.18	0.31	1.13	0.17	0.09	0.31	0.06	0.10	0.45	0.02	0.03	0.19	0.01	0.03	0.24	0.01	0.01	0.03	0.01

Table S12. Descriptive statistics (Min: minimum, Max: maximum, SD: standard deviation) of the biochemical plant traits (carbon, hydrogen, nitrogen, sulphur, and oxygen elements).

Plots	carbon			hydrogen			nitrogen			sulphur			oxygen		
	Min	Max	SD	Min	Max	SD	Min	Max	SD	Min	Max	SD	Min	Max	SD
01_02	47.22	48.07	0.28	5.18	5.90	0.23	1.49	2.46	0.28	0.06	0.19	0.05	35.32	40.75	1.72
02_02	40.11	47.96	2.73	4.38	5.81	0.44	1.46	2.02	0.16	0.09	0.41	0.09	32.33	40.77	2.51
04_01_R	46.19	47.52	0.44	5.42	5.77	0.09	1.54	2.61	0.33	0.00	0.22	0.07	36.30	41.04	1.70
05_02	47.16	48.78	0.50	5.50	5.84	0.11	1.15	2.28	0.40	0.05	0.22	0.07	36.33	44.42	2.43
06_02	45.45	46.98	0.44	5.27	5.75	0.15	1.31	1.89	0.19	0.07	0.58	0.15	37.12	41.55	1.60
07_02	47.49	48.53	0.35	5.79	6.05	0.09	0.90	1.57	0.17	0.08	0.18	0.03	38.94	42.25	1.08
08_02	46.12	48.41	0.65	5.24	5.99	0.19	0.77	2.72	0.59	0.07	0.23	0.06	36.25	43.06	2.32
09_02	45.38	47.71	0.62	5.09	5.95	0.29	1.14	2.37	0.38	0.01	0.23	0.07	36.73	42.23	2.18
10_02	47.23	48.30	0.33	4.39	6.01	0.42	1.29	1.86	0.22	0.02	0.16	0.04	38.32	41.16	0.93
11_02	47.63	49.26	0.52	5.33	6.00	0.24	1.04	2.02	0.26	0.02	0.27	0.07	37.02	42.30	1.57
12_02	47.08	48.88	0.54	4.45	5.84	0.40	1.15	2.66	0.45	0.10	0.51	0.12	34.90	41.33	2.13
13_02	46.41	47.87	0.42	5.38	5.90	0.17	1.11	2.59	0.45	0.04	0.26	0.07	35.07	42.11	2.12
14_02	45.41	48.00	0.70	5.63	5.99	0.12	1.10	2.22	0.37	0.02	0.26	0.09	38.37	43.54	1.46
16_02	46.46	47.89	0.51	4.44	5.92	0.43	1.22	2.54	0.52	0.02	0.20	0.06	35.80	42.27	2.10
17_02	47.26	48.33	0.34	5.56	5.96	0.12	1.16	1.58	0.13	0.11	0.28	0.06	39.82	41.64	0.53
18_02	46.58	47.80	0.42	5.32	5.96	0.17	1.12	2.25	0.40	0.02	0.22	0.08	37.32	42.30	1.54
19_02	46.06	47.74	0.49	5.32	5.88	0.20	1.36	2.20	0.25	0.06	0.29	0.07	38.62	40.80	0.80
20_02	45.81	48.02	0.63	5.70	6.01	0.12	1.33	2.16	0.23	0.02	0.37	0.10	37.91	42.29	1.17
T_02	46.02	47.57	0.45	5.31	5.83	0.15	0.95	2.83	0.82	0.10	0.51	0.13	32.62	40.94	3.10
T_03	48.11	49.15	0.42	5.18	5.91	0.28	1.80	2.70	0.35	0.10	0.49	0.12	36.34	39.02	1.06
T_05	47.95	48.90	0.30	5.68	5.85	0.06	2.00	2.69	0.17	0.07	0.26	0.06	36.39	38.82	0.69
T_10_B	47.16	47.97	0.24	4.98	5.67	0.21	0.95	1.60	0.18	0.01	0.21	0.08	40.28	44.39	1.07

Table S13. Descriptive statistics (Min: minimum, Max: maximum, SD: standard deviation) of the biophysical plant traits (specific leaf area and leaf water content).

Plots	Specific leaf area			Leaf water content		
	Min	**Max**	**SD**	**Min**	**Max**	**SD**
01_02	140.66	203.59	20.55	62.35	71.08	2.78
02_02	79.10	142.26	19.40	32.25	62.80	10.28
04_01_R	119.36	156.67	10.81	64.63	72.61	3.02
05_02	127.04	160.26	12.56	72.74	76.58	1.48
06_02	126.54	154.01	9.43	64.05	71.54	2.58
07_02	131.26	153.01	8.40	62.00	69.36	2.16
08_02	93.04	126.36	10.49	54.57	68.81	4.37
09_02	114.13	150.83	12.95	61.62	72.62	3.49
10_02	156.30	198.24	14.28	69.60	75.89	2.27
11_02	147.99	259.24	35.25	61.49	73.71	3.62
12_02	114.57	150.51	11.18	57.44	70.99	3.86
13_02	135.81	185.70	16.90	72.98	82.17	2.95
14_02	161.48	206.54	15.75	62.62	78.02	5.55
16_02	123.07	202.26	32.56	64.66	69.52	1.76
17_02	165.81	339.00	57.45	65.27	78.56	4.00
18_02	118.72	214.46	32.09	71.74	82.11	3.12
19_02	108.64	161.91	18.54	68.87	74.03	1.68
20_02	110.46	143.75	12.17	63.44	66.23	1.06
T_02	172.95	272.05	37.22	76.42	81.08	1.50
T_03	163.50	202.67	12.61	67.94	71.58	1.22
T_05	196.17	235.98	14.94	64.65	72.90	3.15
T_10_B	164.07	266.54	38.96	52.31	69.23	5.19

5. Conclusions of the thesis

5.1. Summary of the key results

5.1.1. Chapter 2. VIS-NIR, Red-Edge and NIR-Shoulder Based Normalized Vegetation Indices Response to Co-Varying Leaf and Canopy Structural Traits in Heterogeneous Grasslands

The key results of chapter 2 highlighted the importance of using hyperspectral and super-spectral sensors adopting SVIs with band combinations in the VIS, RE, and NIR shoulder spectral region to estimate canopy structure traits in montane temperate grassland ecosystems (IT-MBo and AT-Neu). The results of the study showed that the spectral response across different spectral regions is both site-specific and scale-dependent. The performance of the SVIs based on different parts of the spectrum (VIS, red-edge, and NIR shoulder) in predicting LAI in grassland canopies were analyzed and both reflectance across the spectrum and band combinations showed to be strongly dependent on biochemistry and leaf and canopy structural traits. Very contrasting results were achieved at the temporal and spatial scales. At IT-MBo temporal scale strong correlations ($R^2 > 0.8$) were observed between LAI and both traditional RE and NIR-shoulder SVIs. While, at the AT-Neu study site, generally lower R^2 values were observed compared to the IT-MBo temporal observations. The R^2 patterns were more different across the RE and NIR-shoulder regions. In particular, an evident shift of the well-correlated areas towards the lower wavelengths (from around 750 nm to 740 nm) was observed for AT-Neu compared to IT-MBo temporal observations (Figure 31). This is probably due to the fact that the chlorophyll absorption threshold is different at the two grassland ecosystems (Rossi et al., 2019; Vescovo et al., 2012), and absorption is still present at 754 nm only in the IT-MBo grassland. The evident shift of the well-correlated areas at the AT-Neu site suggests that the performance of some of the RE SVIs is site-specific, probably partly due to different absorption thresholds.

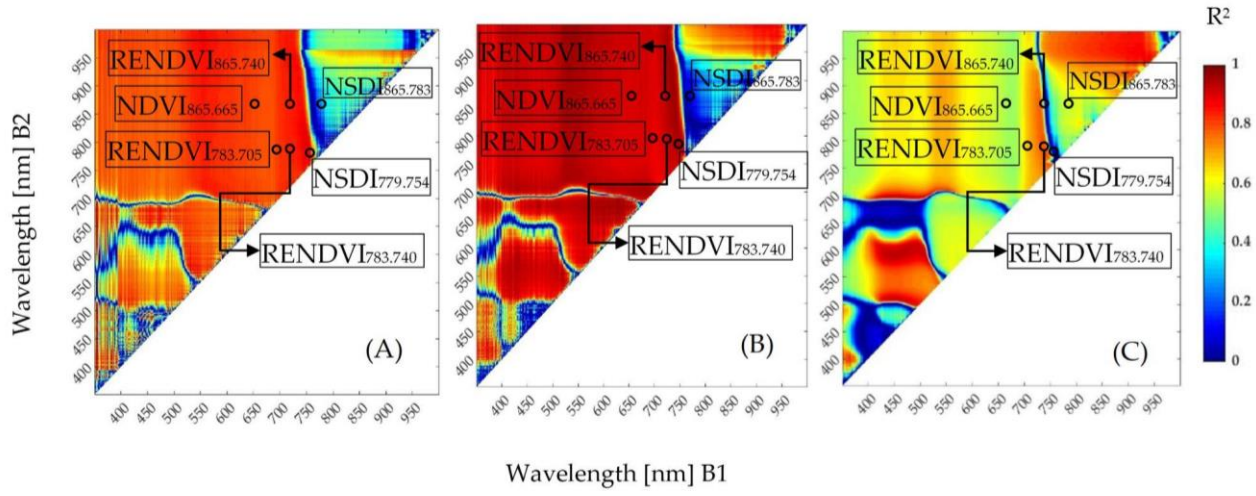

Figure 31. R^2 values based on linear regression between the normalized difference of all two-band combinations and LAI for both study sites (IT-MBo 2013 (**A**); IT-MBo 2014 (**B**); and AT-Neu 2018 (**C**)) considering the temporal scale hyperspectral observations. R^2 obtained using: (**A**–**C**) the hyperspectral data.

Black circles refer to the position of the indices in the correlogram and arrows are indicating the name of the respective indices.

On the other hand, very contrasting results were achieved at the spectral scale at IT-MBo, with very low coefficients of determination values (R^2 < 0.1) between band combinations and LAI along the VIS, red-edge, and the NIR shoulder region of the spectrum (Figure 32). Moreover, the NIR-shoulder slope response at the spatial scale appeared to be more complex compared to the temporal scale and did not strictly follow the typical temporal response at increasing LAI, characterized by an increase of NIR-shoulder slope corresponding to an increase of LAI. The poor performance of the SVIs in retrieving LAI at the spatial scale observations is noteworthy and confirms the observations of Dong et al., (2019) on the strong response of canopy reflectance to canopy structural traits. Darvishzadeh et al., (2008c) showed that LAI, in heterogeneous grasslands, could be estimated at the spatial scale using the SVIs approach with intermediate accuracy (R^2cv values from 0.49 to 0.69).

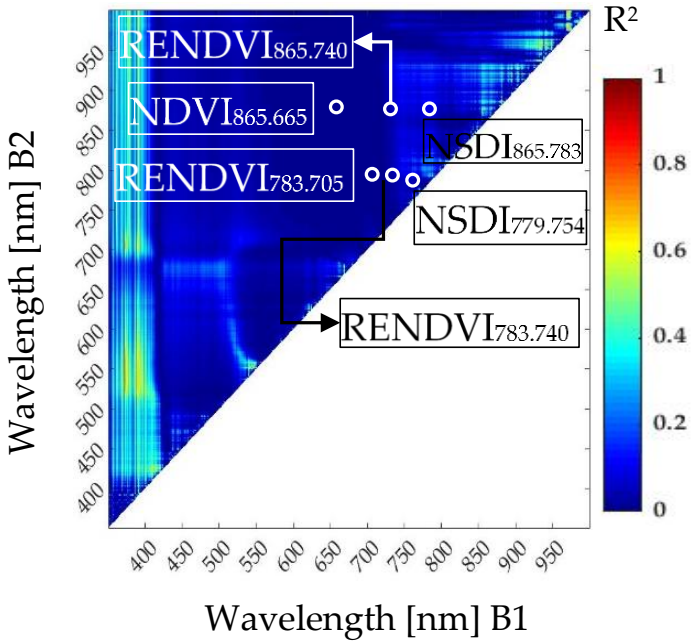

Figure 32. R^2 values based on linear regression between the normalized difference of all two-band combinations and LAI for IT-MBo 2017 considering the spatial scale observations. White circles refer to the position of the indices in the correlogram and arrows are indicating the name of the respective indices.

The SVIs solely based on NIR-shoulder bands (both beyond 750 nm), for example, $NSDI_{779.75}$ (calculated from S-3 simulated bands) performed very well at IT-MBo, but not at the AT-Neu. This is probably due to the fact that the chlorophyll absorption threshold is different at the two grassland ecosystems, and absorption is still present at 754 nm only in the IT-MBo grassland. This result is defining the green-dependency of NIR shoulder SVIs investigated in Vescovo et al., (2012) which were thought to be related to scattering mechanisms and not chlorophyll absorption. The results of the empirical approach were confirmed by the simulations performed with the RTM PROSAIL when both structural and biochemical traits were co-varied. The results of the PROSAIL RTM demonstrated that grassland structural heterogeneity strongly affects the ability to retrieve LAI, with high

uncertainties due to structural and biochemical PTs co-variation. The PROSAIL RTM results confirmed that: (i) the co-variation of all structural traits (such as LAI, LAD, Cm, and N, at the spatial scale) could explain the poor performance of most SVIs; and (ii) due to the co-variation of both structural and biochemistry traits, no SVI is able to provide reliable LAI spatial estimations. In this context, the uncertainties of satellite-based LAI products (in grassland canopies with either spatially or temporally varying structure) need to be carefully taken into account adopting a modeling approach which is minimizing the impact of canopy structural heterogeneity.

5.1.2. Chapter 3. Potential and Limitations of Grasslands α-Diversity Prediction Using Fine-Scale Hyperspectral Imagery

The key results of chapter 3 highlighted the applicability of the optical diversity (also called spectral variability hypothesis, SVH) approach to estimate plant diversity in two different grassland ecosystems (IT-PD: artificially established grassland plots with a species-poor mixture and IT-MBo: species-rich semi-natural grasslands). The results of the study demonstrated that the optical diversity – plant diversity relationships appeared to be not consistent across plant communities. The spectral diversity (expressed as CV and SD) metrics showed to be a proxy of plant diversity similarly to other studies (Aneece et al., 2017; Peng et al., 2019; Wang et al., 2018a), when this approach was used in lower diversity artificial grassland site. However, the data acquired at the semi-natural subalpine grassland at IT-MBo with the same methodology and analyzed with the same approach provided much weaker correlations. When the optical diversity metrics were averaged across different spectral regions as in Aneece et al., (2017) At the IT-PD site, a positive correlation between optical diversity metrics (Appendix A, Figure 1A) and biodiversity indices was mostly observed, while at the IT-MBo site, the correlation was mostly negative (Appendix A, Figure 2A).

When the spectral diversity metrics were calculated for each spectral band on a separate basis, the R-value for some of the spectral bands reached up to R = 0.84 (SD metric at 927 nm) and R = 0.87 (CV metric at 412 nm) in the artificial turfgrass (IT-PD). On the other hand, the maximum R-value observed in the species-rich subalpine grassland (IT-MBo) was only 0.56 for the SD metric at 688 nm. These contradictory results may be due to the very high level of biodiversity (up to 17 species in a 0.25 x 0.25 m plot) and to the rather complex structure of the IT-MBo grasslands (maximum number of species was 17 in a 0.25 x 0.25 m area) compared to the low-diversity turf canopy at the IT-PD site (maximum number of species was 9 in a 0.25 x 0.25 m and 0.5 x 0.5 m area). Further, the artificially established grassland plots, are simplified ecosystems that may not be representative of the complexity of natural field ecological conditions, where leaf and canopy traits can contribute to optical diversity in several ways, adding complexity to the optical and plant diversity relationships in natural grasslands. This can explain the poor performance of the optical sampling methods in complex grassland canopies.

The accuracy of the species diversity estimation varied with the spectral data spatial resolution and with the level of complexity of the community. Spatially heterogeneous canopy structure has a greater possibility to create heterogeneous shadow patterns. Heterogeneous canopy shadow patterns modify optical diversity patterns, which are

influenced not only by plant diversity but also by shadow rates. On the one hand, the use of very high spatial resolution (up to 1 mm) imagery, provides new opportunities, but at the same time pixels of canopy non-photosynthetic elements (flowers and dead material) may create a higher spatial heterogeneity among the spectra, which leads to noise rather than enhancing the information content (Rocchini et al., 2016).

Other studies (Gholizadeh et al., 2018; Lopatin et al., 2017; Peng et al., 2019; Wang et al., 2018a) also highlighted the effect of non-photosynthetic elements, shaded pixels, overexposed pixels, and the soil background on the performance of optical diversity metrics to estimate plant diversity. To improve the accuracy of spectral diversity metrics to predict the plant alpha diversity a range of image post-processing techniques (brightness normalization, filter flowering pixels, filter shaded pixels, and continuum removal) adopted to fully disentangle the optical diversity due to plant diversity from the optical diversity due to illumination artifacts, or due to the presence of pixels of non-photosynthetic material, such as dead material or flowers. The developed processing flow proved, in general, to slightly improve the estimations of plant diversity, by limiting the influence of the factors determining optical diversity but not related to plant diversity. When optical diversity metrics calculated from the post-processed ($Level_3$) data showed higher correlations with biodiversity indices, and that the use of CR spectra generally improved the R values of the correlation between SD and species diversity. Similarly, Blanco-Sacristán et al., (2019) the results in this study, the spectral bands in the red part of the spectrum (around 680 nm) showed to be best for estimating biodiversity in both grasslands study sites.

In this study, the pixel subsampling approach was also tested to check the optimal pixel size to estimate the plant diversity as, with decreasing spatial resolution, the variability in reflectance and, therefore, CV and SD decreased, so the optical detectability of biodiversity was reduced. The results of the pixel subsampling approach were not shown to be effective in this study. The correlation between optical diversity metrics and species richness initially increased and was only reduced when the pixel size was beyond 1 cm in IT-PD, even if for most of the species the average leaf size was much lower than this value. For IT-MBo, the optimal pixel size (at 680 nm) was 1 mm. Conversely, according to Wang et al., (2018), the optimal pixel size to detect species diversity using spectral diversity should match the size of the objects within the sampling unit. Further studies are directed to fully investigate the mechanisms at the basis of the optical diversity, to highlight the biochemical variability and plant diversity relationships in high biodiversity grasslands, and to provide novel insights on the reliability of beta diversity estimations at the spatial scale.

5.1.3. Chapter 4. On the importance of functional diversity links with α and β diversity for the applicability of the optical diversity approach in a subalpine grassland of the Italian Alps

The results of chapter 4 revealed that the relationship between PTs variability (which expresses functional diversity) and species diversity strongly varies across the diversity scales. The complex dynamics of the structurally heterogeneous canopy might hamper the PTs variability link to the α-diversity in a semi-natural grassland ecosystem (IT-MBo). An overall weak relationship between PTs variability and species α-diversity was found and these results suggested that the relationship between PTs and species diversity may be

determined by the presence of heterogeneous elements (e.g., flowers, stems, leaves, and dead material) in the biomass samples. The presence of such non-photosynthetic elements might hamper the PTs variability link to α-diversity. Further the weak correlation between ecosystem functional diversity (estimated by PT variability) and α-diversity may be related to the PT variability sampling strategy adopted in this study, however more studies are needed to verify this hypothesis.

Conversely, a moderate to high correlation is found between taxonomic β-diversity (measured by Jaccard dissimilarity index of the species, families, and functional groups percent cover) and the Euclidean distances of the biochemical and biophysical PTs. The variability of PTs (including chla, chlb, lut, neox, violax, N, O, and dry biomass) showed to be associated with species distance. More specifically, N content (in the IT-MBo unfertilized grassland) was directly correlated with β-diversity, differently from what suggested by Humbert et al., (2016). The relationship between chlorophyll traits (chla and chlb) and beta diversity are in line with a recent study of Torresani et al., (2021) where PTs variability links with biodiversity were analyzed in forest ecosystems. The variation of Cbrown, Car and Cab was shown to be an accurate proxy of tree species diversity (Torresani et al., 2021) although uncertainties in the estimation of leaf chemistry were deducted from physical model inversion and not from direct observations. However, the current study confirmed that most assessments of diversity (from remote observations or from laboratory measurements of *in-situ* samples) are rather uncertain and more studies need to be performed to assess their suitability for biodiversity studies.

Furtherly, the results of the study suggested the SVH approach can be a better proxy of biodiversity at community scale in the same ecosystem where the spectral diversity failed to estimate alpha diversity. The analysis of the Mantel test revealed that a moderate correlation can be found between the spectral diversity (measured by SAM among the plots) with taxonomic β-diversity (measured by Jaccard dissimilarity among the plots), this leading to the conclusion that the link between functional and species diversity may be an indicator of the applicability of optical sampling methods to estimate biodiversity.

5.2. Conclusion and outlook

This research shows that remote sensing provides efficient methods and tools which can effectively be used to monitor biodiversity and PTs in grasslands ecosystems. During the research, I was able to predict key ecological grassland PTs (i.e., LAI, species richness) which are crucial for biodiversity conservation and ecosystem health and highlighted some constraints to predict the PTs when structurally heterogeneous canopies are investigated. The findings of the study can give useful guidance for the selection of the most suitable methods and scale to estimate structural PTs and biodiversity in heterogeneous grassland ecosystems.

The specific conclusions for the study and the main outcome of each chapter are summarized as follows:

The results of the Paper I revealed that the spectral response across different spectral regions (VIS, RE, and NIR-shoulder) are to be both site-specific and scale-dependent. The Paper I highlighted the impact of canopy structural and biochemical PTs heterogeneity on the

LAI estimations by using different SVIs based on different spectral regions (VIS, RE, and NIR-shoulder) at temporal and spatial scales. The results demonstrated that the relationship between SVIs and LAI is strongly mediated by canopy structural heterogeneity, for this reason, no reliable estimation of LAI was possible at spatial scale. The unexpected weak correlation between SVIs and LAI at spatial scale were confirmed by modeling, through the physical-based RTM PROSAIL model: when both structural and biochemical traits were co-varied, a similar performance of the SVIs to estimate LAI was achieved, as observed in the empirical approach. In this context, the uncertainties of satellite-based LAI products (in grassland canopies with either spatially or temporally varying structure) need to be carefully taken into account adopting a modelling approach which is minimizing the impact of canopy structural heterogeneity.

The Paper II showed that the relationship between spectral diversity metrics and species diversity is strongly affected by canopy structural heterogeneity and complexity, and that relationships between species diversity and optical diversity metrics were not consistent across plant communities. In this study, I found a significant relationship between spectral diversity and species diversity in the lower diversity artificial grassland site. However, the same approach provided much weaker correlations in the species-rich semi-natural grassland ecosystem. The results of this study also highlighted the impact of post processing techniques on the relationships between optical data and grassland diversity. Finally, the results of the study revealed that the VIS part of the spectrum (and in particular the red domain), characterized by a strong absorbance, showed to be one of the key spectral areas for biodiversity detection.

The Paper III demonstrated that PTs variability and spectral diversity can be associated with biodiversity at community scale while at local scale PTs variability and spectral diversity were not well-correlated. The structurally heterogeneous canopy modifies optical diversity patterns because high structural diversity and complex vertical structure, in these canopies, may express high spectral diversity even when low species diversity is observed, and vice versa. So, our first hypothesis was that the reason of the poor correlation between optical data and biodiversity may be due to the inability of the spectral data to detect PTs variability (functional diversity). The preliminary results of this study, conversely, indicate that the poor performance of optical diversity proxies in estimating biodiversity in structurally heterogeneous grasslands might be due to the complex relationships between functional diversity and biodiversity, rather than the impossibility to detect functional diversity with spectral proxies. Such first insights need to be confirmed by further studies focused on the spectral feedback of both functional and species diversity.

Overall, the recommendations for further research arising from the following PhD thesis

can be summarized as followed:

1. Further research will be able to clarify if, in complex heterogeneous ecosystems such as the grasslands of the Alps, the optical diversity approach can be adopted to detect biodiversity (at local and community scale). Such insights will provide more robust

information on the mechanisms linking optical diversity, functional diversity, and biodiversity.

2. This research was conducted by using a limited number of experimental plots (10 spatial plots in Paper I, 25 plots in Paper II, and 22 plots in Paper III). This sample size was, in some cases, too small to draw robust conclusions. Further multi-year studies with larger sample sizes are required to fully understand and generalize the complex underlying mechanisms typical of natural plant communities.
3. To test the applicability of the SVH approach in this study the hyperspectral sensor used for the field data collection had fine spectral resolution but covered only the VIS-NIR region of the spectrum. Therefore, the optical diversity analyses presented in (Paper II) study primarily reflected the influence of non-photosynthetic elements of the canopies. Future work may consider the full range of spectra (VIS-NIR-SWIR) because this may provide useful information related to water content which can be critical for accurate assignment of PTs both at leaf and canopy scales.

References

Adams, J. E., & Arkin, G. F. (1977). A light interception method for measuring row crop ground cover. *Soil Science Society of America Journal*, *41*(4), 789-792.

Aldakheel, Y. Y., & Danson, F. M. (1997). Spectral reflectance of dehydrating leaves: measurements and modelling. *International journal of remote sensing*, *18*(17), 3683-3690.

Anderson, J. M. (1991). The effects of climate change on decomposition processes in grassland and coniferous forests. *Ecological Applications*, *1*(3), 326-347.

Aneece, I. P., Epstein, H., & Lerdau, M. (2017). Correlating species and spectral diversities using hyperspectral remote sensing in early-successional fields. *Ecology and evolution*, *7*(10), 3475-3488.

Aneece, I., & Epstein, H. (2015). Distinguishing early successional plant communities using ground-level hyperspectral data. *Remote Sensing*, *7*(12), 16588-16606.

Aoki, M., Yabuki, K., Totsuka, T., & Nishida, M. (1986). Remote sensing of chlorophyll content of leaf (I). *Environment Control in Biology*, *24*(1), 21-26.

Asner, G. P., & Martin, R. E. (2009). Airborne spectranomics: mapping canopy chemical and taxonomic diversity in tropical forests. *Frontiers in Ecology and the Environment*, *7*(5), 269-276.

Atkin, O., Kattge, J., Diaz, S., Lavorel, S., Prentice, I. C., Leadley, P., ... & Zaehle, S. (2011). TRY-a global database of plant traits.

Atzberger, C., Darvishzadeh, R., Immitzer, M., Schlerf, M., Skidmore, A., & Le Maire, G. (2015). Comparative analysis of different retrieval methods for mapping grassland leaf area index using airborne imaging spectroscopy. *International Journal of Applied Earth Observation and Geoinformation*, *43*, 19-31.

Atzberger, C., Darvishzadeh, R., Schlerf, M., & Le Maire, G. (2013). Suitability and adaptation of PROSAIL radiative transfer model for hyperspectral grassland studies. *Remote sensing letters*, *4*(1), 55-64.

Babar, M. A., Van Ginkel, M., Klatt, A. R., Prasad, B., & Reynolds, M. P. (2006). The potential of using spectral reflectance indices to estimate yield in wheat grown under reduced irrigation. *Euphytica*, *150*(1), 155-172.

Balzarolo, M., Peñuelas, J., & Veroustraete, F. (2019). Influence of landscape heterogeneity and spatial resolution in multi-temporal in situ and MODIS NDVI data proxies for seasonal GPP dynamics. *Remote Sensing*, *11*(14), 1656.

Baselga, A. (2013). Separating the two components of abundance-based dissimilarity: balanced changes in abundance vs. abundance gradients. *Methods in Ecology and Evolution*, *4*(6), 552-557.

Behmann, J., Acebron, K., Emin, D., Bennertz, S., Matsubara, S., Thomas, S., ... & Rascher, U. (2018). Specim IQ: evaluation of a new, miniaturized handheld hyperspectral camera and its application for plant phenotyping and disease detection. *Sensors*, *18*(2), 441.

Berger, W. H., & Parker, F. L. (1970). Diversity of planktonic foraminifera in deep-sea sediments. *Science*, *168*(3937), 1345-1347.

Blackburn, G. A. (1998). Spectral indices for estimating photosynthetic pigment concentrations: A test using senescent tree leaves. International Journal of Remote Sensing, 19(4), 657-675.

Blanco-Sacristán, J., Panigada, C., Tagliabue, G., Gentili, R., Colombo, R., Ladrón de Guevara, M., ... & Rossini, M. (2019). Spectral diversity successfully estimates the α-diversity of biocrust-forming lichens. *Remote Sensing*, *11*(24), 2942.

Bolch, E. A., Santos, M. J., Ade, C., Khanna, S., Basinger, N. T., Reader, M. O., & Hestir, E. L. (2020). Remote detection of invasive alien species. In *Remote Sensing of Plant Biodiversity* (pp. 267-307). Springer, Cham.

Bray, J. R., & Curtis, J. T. (1957). An ordination of the upland forest communities of southern Wisconsin. *Ecological monographs*, *27*(4), 326-349.

Casas, A., Riaño, D., Ustin, S. L., Dennison, P., & Salas, J. (2014). Estimation of water-related biochemical and biophysical vegetation properties using multitemporal airborne hyperspectral data and its comparison to MODIS spectral response. *Remote Sensing of Environment*, *148*, 28-41.

Cavender-Bares, J., Schweiger, A. K., Pinto-Ledezma, J. N., & Meireles, J. E. (2020). Applying remote sensing to biodiversity science. In *Remote Sensing of Plant Biodiversity* (pp. 13-42). Springer, Cham.

Chemini, C., & Rizzoli, A. (2014). Land use change and biodiversity conservation in the Alps. *Journal of Mountain Ecology*, *7*, 1–7.

Clark, M. L., & Roberts, D. A. (2012). Species-level differences in hyperspectral metrics among tropical rainforest trees as determined by a tree-based classifier. *Remote Sensing*, *4*(6), 1820-1855.

Claudio, H. C., Cheng, Y., Fuentes, D. A., Gamon, J. A., Luo, H., Oechel, W., ... & Sims, D. A. (2006). Monitoring drought effects on vegetation water content and fluxes in chaparral with the 970 nm water band index. *Remote Sensing of Environment*, *103*(3), 304-311.

Cogato, A., Pagay, V., Marinello, F., Meggio, F., Grace, P., & De Antoni Migliorati, M. (2019). Assessing the feasibility of using sentinel-2 imagery to quantify the impact of heatwaves on irrigated vineyards. *Remote Sensing*, *11*(23), 2869.

Colwell, R. K. (2009). III. 1 biodiversity: concepts, patterns, and measurement. In *The Princeton guide to ecology* (pp. 257-263). Princeton University Press.

Colwell, R. K., & Coddington, J. A. (1994). Estimating terrestrial biodiversity through extrapolation. *Philosophical Transactions of the Royal Society of London. Series B: Biological Sciences*, *345*(1311), 101-118.

Conti, L., Malavasi, M., Galland, T., Komárek, J., Lagner, O., Carmona, C. P., ... & Šímová, P. (2021). The relationship between species and spectral diversity in grassland communities is mediated by their vertical complexity. *Applied Vegetation Science*, 24(3).

Danner, M., Berger, K., Wocher, M., Mauser, W., & Hank, T. (2019). Fitted PROSAIL parameterization of leaf inclinations, water content and brown pigment content for winter wheat and maize canopies. *Remote Sensing*, *11*(10), 1150.

Darvishzadeh, R., Skidmore, A., Abdullah, H., Cherenet, E., Ali, A., Wang, T., ... & Paganini, M. (2019). Mapping leaf chlorophyll content from Sentinel-2 and RapidEye data in

spruce stands using the invertible forest reflectance model. *International Journal of Applied Earth Observation and Geoinformation*, *79*, 58-70.

Darvishzadeh, R., Skidmore, A., Schlerf, M., & Atzberger, C. (2008a). Inversion of a radiative transfer model for estimating vegetation LAI and chlorophyll in a heterogeneous grassland. *Remote sensing of environment*, *112*(5), 2592-2604.

Darvishzadeh, R., Skidmore, A., Schlerf, M., Atzberger, C., Corsi, F., & Cho, M. (2008b). LAI and chlorophyll estimation for a heterogeneous grassland using hyperspectral measurements. *ISPRS journal of photogrammetry and remote sensing*, *63*(4), 409-426.

Darvishzadeh, R., Skidmore, A., Atzberger, C., & van Wieren, S. (2008c). Estimation of vegetation LAI from hyperspectral reflectance data: Effects of soil type and plant architecture. *International journal of applied Earth observation and geoinformation*, *10*(3), 358-373.

Datt, B. (1998). Remote sensing of chlorophyll a, chlorophyll b, chlorophyll a+ b, and total carotenoid content in eucalyptus leaves. *Remote Sensing of Environment*, *66*(2), 111-121.

Delegido, J., Verrelst, J., Alonso, L., & Moreno, J. (2011). Evaluation of sentinel-2 red-edge bands for empirical estimation of green LAI and chlorophyll content. *Sensors*, *11*(7), 7063-7081.

Delegido, J., Verrelst, J., Meza, C. M., Rivera, J. P., Alonso, L., & Moreno, J. (2013). A red-edge spectral index for remote sensing estimation of green LAI over agroecosystems. *European Journal of Agronomy*, *46*, 42-52.

Delegido, J., Verrelst, J., Rivera, J. P., Ruiz-Verdú, A., & Moreno, J. (2015). Brown and green LAI mapping through spectral indices. *International Journal of Applied Earth Observation and Geoinformation*, *35*, 350-358.

Derner, J. D., & Schuman, G. E. (2007). Carbon sequestration and rangelands: a synthesis of land management and precipitation effects. *Journal of soil and water conservation*, *62*(2), 77-85.

Disney, M., Lewis, P., & Saich, P. (2006). 3D modelling of forest canopy structure for remote sensing simulations in the optical and microwave domains. *Remote Sensing of Environment*, *100*(1), 114-132.

Dong, T., Liu, J., Shang, J., Qian, B., Ma, B., Kovacs, J. M., ... & Shi, Y. (2019). Assessment of red-edge vegetation indices for crop leaf area index estimation. *Remote Sensing of Environment*, *222*, 133-143.

Donita, N., Ivan, D., & Pedrotti, F. (2003). Structure and Productivity of the Meadows of Viote on Monte Bondone. *Centro di ecologia alpine: Trento, Italy*, 36.

Durán, S. M., Martin, R. E., Díaz, S., Maitner, B. S., Malhi, Y., Salinas, N., ... & Enquist, B. J. (2019). Informing trait-based ecology by assessing remotely sensed functional diversity across a broad tropical temperature gradient. *Science advances*, *5*(12), eaaw8114.

Ellenberg, H., & Leuschner, C. (2010). *Vegetation Mitteleuropas mit den Alpen: in ökologischer, dynamischer und historischer Sicht* (Vol. 8104).

Fang, H., Liang, S., & Kuusk, A. (2003). Retrieving leaf area index using a genetic algorithm with a canopy radiative transfer model. *Remote sensing of environment*, *85*(3), 257-270.

Fava, F., Colombo, R., Bocchi, S., Meroni, M., Sitzia, M., Fois, N., & Zucca, C. (2009). Identification of hyperspectral vegetation indices for Mediterranean pasture

characterization. *International Journal of Applied Earth Observation and Geoinformation*, *11*(4), 233-243.

Fernández-Manso, A., Fernández-Manso, O., & Quintano, C. (2016). SENTINEL-2A red-edge spectral indices suitability for discriminating burn severity. *International journal of applied earth observation and geoinformation*, *50*, 170-175.

Filella, I., & Penuelas, J. (1994). The red edge position and shape as indicators of plant chlorophyll content, biomass and hydric status. *International journal of remote sensing*, *15*(7), 1459-1470.

Frampton, W.J.; Dash, J.; Watmough, G.; Milton, E.J. Evaluating the capabilities of Sentinel-2 for quantitative estimation of biophysical variables in vegetation. *ISPRS J. Photogramm. Remote Sens.* **2013**, *82*, 83–92.

Gamon, J. A., & Surfus, J. S. (1999). Assessing leaf pigment content and activity with a reflectometer. *The New Phytologist*, *143*(1), 105-117.

Gamon, J. A., Wang, R., Gholizadeh, H., Zutta, B., Townsend, P. A., & Cavender-Bares, J. (2020). Consideration of scale in remote sensing of biodiversity. In *Remote sensing of plant biodiversity* (pp. 425-447). Springer, Cham.

Gholizadeh, H., Gamon, J. A., Helzer, C. J., & Cavender-Bares, J. (2020). Multi-temporal assessment of grassland α-and β-diversity using hyperspectral imaging. *Ecological Applications*, *30*(7), e02145.

Gholizadeh, H., Gamon, J. A., Townsend, P. A., Zygielbaum, A. I., Helzer, C. J., Hmimina, G. Y., ... & Cavender-Bares, J. (2019). Detecting prairie biodiversity with airborne remote sensing. *Remote Sensing of Environment*, *221*, 38-49.

Gholizadeh, H., Gamon, J. A., Zygielbaum, A. I., Wang, R., Schweiger, A. K., & Cavender-Bares, J. (2018). Remote sensing of biodiversity: Soil correction and data dimension reduction methods improve assessment of α-diversity (species richness) in prairie ecosystems. *Remote sensing of environment*, *206*, 240-253.

Gianelle, D., & Vescovo, L. (2007). Determination of green herbage ratio in grasslands using spectral reflectance. Methods and ground measurements. *International Journal of Remote Sensing*, *28*(5), 931-942.

Gitelson, A. A., & Merzlyak, M. N. (1996). Signature analysis of leaf reflectance spectra: Algorithm development for remote sensing of chlorophyll. Journal of Plant Physiology, 148(3-4), 494-500.

Gitelson, A. A., Chivkunova, O. B., & Merzlyak, M. N. (2009). Nondestructive estimation of anthocyanins and chlorophylls in anthocyanic leaves. *American Journal of Botany*, *96*(10), 1861-1868.

Gitelson, A. A., Gritz, Y., & Merzlyak, M. N. (2003). Relationships between leaf chlorophyll content and spectral reflectance and algorithms for non-destructive chlorophyll assessment in higher plant leaves. *Journal of plant physiology*, *160*(3), 271-282.

Gitelson, A., & Merzlyak, M. N. (1994). Spectral reflectance changes associated with autumn senescence of Aesculus hippocastanum L. and Acer platanoides L. leaves. Spectral features and relation to chlorophyll estimation. *Journal of plant physiology*, *143*(3), 286-292.

Gitelson, A., Garbuzov, G., Szilagyi, F., Mittenzwey, K. H., Karnieli, A., & Kaiser, A. (1993). Quantitative remote sensing methods for real-time monitoring of inland waters quality. *International Journal of Remote Sensing*, *14*(7), 1269-1295.

Gitelson, P. J., Dungan, J. L., & Gholz, H. L. (1990). Exploring the relationship between reflectance red edge and chlorophyll content in slash pine. *Tree physiology*, *7*(1-2-3-4), 33-48.

Grace, J. B., Michael Anderson, T., Smith, M. D., Seabloom, E., Andelman, S. J., Meche, G., ... & Willig, M. R. (2007). Does species diversity limit productivity in natural grassland communities?. *Ecology Letters*, *10*(8), 680-689.

Gutierrez, M., Reynolds, M. P., Raun, W. R., Stone, M. L., & Klatt, A. R. (2010). Spectral water indices for assessing yield in elite bread wheat genotypes under well-irrigated, water-stressed, and high-temperature conditions. *Crop Science*, *50*(1), 197-214.

Hall, K., Reitalu, T., Sykes, M. T., & Prentice, H. C. (2012). Spectral heterogeneity of QuickBird satellite data is related to fine-scale plant species spatial turnover in semi-natural grasslands. *Applied Vegetation Science*, *15*(1), 145-157.

Hansen, P. M., & Schjoerring, J. K. (2003). Reflectance measurement of canopy biomass and nitrogen status in wheat crops using normalized difference vegetation indices and partial least squares regression. *Remote sensing of environment*, *86*(4), 542-553.

Heumann, B. W., Hackett, R. A., & Monfils, A. K. (2015). Testing the spectral diversity hypothesis using spectroscopy data in a simulated wetland community. *Ecological Informatics*, *25*, 29-34.

Hoffmann, S., Schmitt, T. M., Chiarucci, A., Irl, S. D., Rocchini, D., Vetaas, O. R., ... & Beierkuhnlein, C. (2019). Remote sensing of β-diversity: Evidence from plant communities in a semi-natural system. *Applied Vegetation Science*, *22*(1), 13-26.

Homolova, L., Malenovský, Z., Clevers, J. G., García-Santos, G., & Schaepman, M. E. (2013). Review of optical-based remote sensing for plant trait mapping. *Ecological Complexity*, *15*, 1-16.

Horler, D. N. H., Dockray, M., & Barber, J. (1983). The red edge of plant leaf reflectance. *International journal of remote sensing*, *4*(2), 273-288.

Houborg, R., Soegaard, H., & Boegh, E. (2007). Combining vegetation index and model inversion methods for the extraction of key vegetation biophysical parameters using Terra and Aqua MODIS reflectance data. *Remote Sensing of Environment*, *106*(1), 39-58.

Humbert, J. Y., Dwyer, J. M., Andrey, A., & Arlettaz, R. (2016). Impacts of nitrogen addition on plant biodiversity in mountain grasslands depend on dose, application duration and climate: a systematic review. *Global change biology*, *22*(1), 110-120.

Imran, H. A., Gianelle, D., Rocchini, D., Dalponte, M., Martín, M. P., Sakowska, K., ... & Vescovo, L. (2020). VIS-NIR, red-edge and NIR-shoulder based normalized vegetation indices response to co-varying leaf and Canopy structural traits in heterogeneous grasslands. *Remote Sensing*, *12*(14), 2254.

Imran, H. A., Gianelle, D., Scotton, M., Rocchini, D., Dalponte, M., Macolino, S., Sakowska, K., et al. (2021). Potential and Limitations of Grasslands α-Diversity Prediction Using Fine-Scale Hyperspectral Imagery. *Remote Sensing*, *13*(14), 2649.

Inoue, Y., Guérif, M., Baret, F., Skidmore, A., Gitelson, A., Schlerf, M., ... & Olioso, A. (2016). *Simple and robust methods for remote sensing of canopy chlorophyll content: a*

comparative analysis of hyperspectral data for different types of vegetation (Vol. 39, No. 12, pp. 2609-2623).

Jaccard, P. (1912). The distribution of the flora in the alpine zone. 1. *New phytologist*, *11*(2), 37-50.

Jackson, R. D., & Huete, A. R. (1991). Interpreting vegetation indices. *Preventive veterinary medicine*, *11*(3-4), 185-200.

Jacquemoud, S., & Baret, F. (1990). PROSPECT: A model of leaf optical properties spectra. *Remote sensing of environment*, *34*(2), 75-91.

Kent, M., & Coker, P. (1992). Vegetation description and analysis, a practical approach–John Wiley & Sons. *New York*, 319.

Khare, S., Latifi, H., & Rossi, S. (2019). Forest beta-diversity analysis by remote sensing: How scale and sensors affect the Rao's Q index. *Ecological Indicators*, *106*, 105520.

Kira, O., Nguy-Robertson, A. L., Arkebauer, T. J., Linker, R., & Gitelson, A. A. (2017). Toward generic models for green LAI estimation in maize and soybean: Satellite observations. *Remote Sensing*, *9*(4), 318.

Knyazikhin, Y., Schull, M. A., Stenberg, P., Mõttus, M., Rautiainen, M., Yang, Y., ... & Myneni, R. B. (2013). Hyperspectral remote sensing of foliar nitrogen content. *Proceedings of the National Academy of Sciences*, *110*(3), E185-E192.

Kruse, F. A., Lefkoff, A. B., Boardman, J. W., Heidebrecht, K. B., Shapiro, A. T., Barloon, P. J., & Goetz, A. F. H. (1993). The spectral image processing system (SIPS)—interactive visualization and analysis of imaging spectrometer data. *Remote sensing of environment*, *44*(2-3), 145-163.

Kumar, L., & Mutanga, O. (2017). Remote Sensing of Above-Ground Biomass. Remote Sensing, 9(9), 935.

Kumar, L., Schmidt, K., Dury, S., & Skidmore, A. (2002). Imaging spectrometry and vegetation science. In *Imaging spectrometry* (pp. 111-155). Springer, Dordrecht.

Laliberté, E., Schweiger, A. K., & Legendre, P. (2020). Partitioning plant spectral diversity into alpha and beta components. *Ecology letters*, *23*(2), 370-380.

Latham, J., Cumani, R., Rosati, I., & Bloise, M. (2014). Global land cover share (GLC-SHARE) database beta-release version 1.0-2014. *FAO: Rome, Italy*.

Laurila-Pant, M., Lehikoinen, A., Uusitalo, L., & Venesjärvi, R. (2015). How to value biodiversity in environmental management?. *Ecological indicators*, *55*, 1-11.

Lennon, J. J., Koleff, P., Greenwood, J. J. D., & Gaston, K. J. (2001). The geographical structure of British bird distributions: diversity, spatial turnover and scale. *Journal of Animal Ecology*, *70*(6), 966-979.

Li, F., Yan, Y., Zhang, J., Zhang, Q., & Niu, J. (2021). Taxonomic, functional, and phylogenetic beta diversity in the Inner Mongolia grassland. *Global Ecology and Conservation*, *28*, e01634.

Li, X., Zhang, Y., Bao, Y., Luo, J., Jin, X., Xu, X., ... & Yang, G. (2014). Exploring the best hyperspectral features for LAI estimation using partial least squares regression. *Remote Sensing*, *6*(7), 6221-6241.

Liu, L. Y., Huang, W. J., PU, R. L., & Wang, J. H. (2014). Detection of internal leaf structure deterioration using a new spectral ratio index in the near-infrared shoulder region. *Journal of Integrative Agriculture*, *13*(4), 760-769.

Liu, Z. Z., Li, W., & Yang, M. (2015). Two general extension algorithms of Latin hypercube sampling. *Mathematical Problems in Engineering*, *2015*.

Lopatin, J., Fassnacht, F. E., Kattenborn, T., & Schmidtlein, S. (2017). Mapping plant species in mixed grassland communities using close range imaging spectroscopy. *Remote Sensing of Environment*, *201*, 12-23.

Lucas, K. L., & Carter, G. A. (2008). The use of hyperspectral remote sensing to assess vascular plant species richness on Horn Island, Mississippi. *Remote Sensing of Environment*, *112*(10), 3908-3915.

Lüth, C., Tasser, E., Niedrist, G., Dalla Via, J., & Tappeiner, U. (2011). Plant communities of mountain grasslands in a broad cross-section of the Eastern Alps. *Flora-Morphology, Distribution, Functional Ecology of Plants*, *206*(5), 433-443.

Ma, X., Migliavacca, M., Wirth, C., Bohn, F. J., Huth, A., Richter, R., & Mahecha, M. D. (2020). Monitoring plant functional diversity using the reflectance and echo from space. *Remote Sensing*, *12*(8), 1248.

Mantel, N. (1967). The detection of disease clustering and a generalized regression approach. *Cancer research*, *27*(2 Part 1), 209-220.

Markwell, J., Osterman, J. C., & Mitchell, J. L. (1995). Calibration of the Minolta SPAD-502 leaf chlorophyll meter. Photosynthesis research, 46(3), 467-472.

Martens, S. N., Ustin, S. L., & Norman, J. M. (1991). Measurement of tree canopy architecture. *International Journal of Remote Sensing*, *12*(7), 1525-1545.

Marzialetti, F., Cascone, S., Frate, L., Di Febbraro, M., Acosta, A. T. R., & Carranza, M. L. (2021). Measuring Alpha and Beta Diversity by Field and Remote-Sensing Data: A Challenge for Coastal Dunes Biodiversity Monitoring. *Remote Sensing*, *13*(10), 1928.

Matheny, A. M., Mirfenderesgi, G., & Bohrer, G. (2017). Trait-based representation of hydrological functional properties of plants in weather and ecosystem models. Plant Diversity, 39(1), 1-12.

McIntosh, R. P. (1967). An index of diversity and the relation of certain concepts to diversity. *Ecology*, *48*(3), 392-404.

Melendo-Vega, J. R., Martín, M. P., Pacheco-Labrador, J., González-Cascón, R., Moreno, G., Pérez, F., ... & Riaño, D. (2018). Improving the performance of 3-D radiative transfer model FLIGHT to simulate optical properties of a tree-grass ecosystem. *Remote Sensing*, *10*(12), 2061.

Meroni, M., Colombo, R., & Panigada, C. (2004). Inversion of a radiative transfer model with hyperspectral observations for LAI mapping in poplar plantations. *Remote sensing of environment*, *92*(2), 195-206.

Migliavacca, M., Perez-Priego, O., Rossini, M., El-Madany, T. S., Moreno, G., Van der Tol, C., ... & Reichstein, M. (2017). Plant functional traits and canopy structure control the relationship between photosynthetic CO 2 uptake and far-red sun-induced fluorescence in a Mediterranean grassland under different nutrient availability. *New Phytologist*, *214*(3), 1078-1091.

Miraglio, T., Adeline, K., Huesca, M., Ustin, S., & Briottet, X. (2020). Monitoring LAI, chlorophylls, and carotenoids content of a woodland savanna using hyperspectral imagery and 3D radiative transfer modeling. *Remote Sensing*, *12*(1), 28.

Möckel, T., Dalmayne, J., Schmid, B. C., Prentice, H. C., & Hall, K. (2016). Airborne hyperspectral data predict fine-scale plant species diversity in grazed dry grasslands. *Remote Sensing*, *8*(2), 133.

Müller-Linow, M., Pinto-Espinosa, F., Scharr, H., & Rascher, U. (2015). The leaf angle distribution of natural plant populations: assessing the canopy with a novel software tool. *Plant methods*, *11*(1), 1-16.

Naeem, S., Chazdon, R., Duffy, J. E., Prager, C., & Worm, B. (2016). Biodiversity and human well-being: an essential link for sustainable development. *Proceedings of the Royal Society B: Biological Sciences*, *283*(1844), 20162091.

Nguy-Robertson, A. L., Peng, Y., Gitelson, A. A., Arkebauer, T. J., Pimstein, A., Herrmann, I., ... & Bonfil, D. J. (2014). Estimating green LAI in four crops: Potential of determining optimal spectral bands for a universal algorithm. *Agricultural and forest meteorology*, *192*, 140-148.

Oksanen, J., Blanchet, F. G., Kindt, R., Legendre, P., Minchin, P. R., O'Hara, R. B., ... & Wagner, H. (2020). Vegan community ecology package: ordination methods, diversity analysis and other functions for community and vegetation ecologists. R package ver, 2.5-7.

Pacheco-Labrador, J., El-Madany, T. S., van der Tol, C., Martin, M. P., Gonzalez-Cascon, R., Perez-Priego, O., ... & Migliavacca, M. (2020). senSCOPE: Modeling radiative transfer and biochemical processes in mixed canopies combining green and senescent leaves with SCOPE. *bioRxiv*.

Papale, D., Migliavacca, M., Cremonese, E., Cescatti, A., Alberti, G., Balzarolo, M., ... & Valentini, R. (2014). Carbon, water and energy fluxes of terrestrial ecosystems in Italy. In *The greenhouse gas balance of Italy* (pp. 11-45). Springer, Berlin, Heidelberg.

Pasolli, L., Asam, S., Castelli, M., Bruzzone, L., Wohlfahrt, G., Zebisch, M., & Notarnicola, C. (2015). Retrieval of Leaf Area Index in mountain grasslands in the Alps from MODIS satellite imagery. *Remote Sensing of Environment*, *165*, 159-174.

Peng, Y., Fan, M., Bai, L., Sang, W., Feng, J., Zhao, Z., & Tao, Z. (2019). Identification of the best hyperspectral indices in estimating plant species richness in sandy grasslands. *Remote Sensing*, *11*(5), 588.

Peng, Y., Nguy-Robertson, A., Arkebauer, T., & Gitelson, A. A. (2017). Assessment of canopy chlorophyll content retrieval in maize and soybean: Implications of hysteresis on the development of generic algorithms. *Remote Sensing*, *9*(3), 226.

Peñuelas, J., & Inoue, Y. (1999). Reflectance indices indicative of changes in water and pigment contents of peanut and wheat leaves. Photosynthetica, 36(3), 355-360.

Peñuelas, J., Gamon, J. A., Fredeen, A. L., Merino, J., & Field, C. B. (1994). Reflectance indices associated with physiological changes in nitrogen-and water-limited sunflower leaves. *Remote sensing of Environment*, *48*(2), 135-146.

Pettai, H., Oja, V., Freiberg, A., & Laisk, A. (2005). Photosynthetic activity of far-red light in green plants. *Biochimica et Biophysica Acta (BBA)-Bioenergetics*, *1708*(3), 311-321.

Philip Robertson, G., Gross, K. L., Hamilton, S. K., Landis, D. A., Schmidt, T. M., Snapp, S. S., & Swinton, S. M. (2014). Farming for ecosystem services: An ecological approach to production agriculture. *BioScience*, *64*(5), 404-415.

Pielou, E. C. (1966). The measurement of diversity in different types of biological collections. *Journal of theoretical biology*, *13*, 131-144.

Pornaro, C.; Vescovo, L.; Dalponte, M.; Gianelle, D.; Macolino, S. (2019). A new hyperspectral based system for the estimation of weeds and botanical composition of turfgrasses. In Proceedings of the 6th European Turfgrass Society Field Days, Padova, Italy, 27–28.

Prasad, B., Carver, B. F., Stone, M. L., Babar, M. A., Raun, W. R., & Klatt, A. R. (2007). Potential use of spectral reflectance indices as a selection tool for grain yield in winter wheat under great plains conditions. *Crop science*, *47*(4), 1426-1440.

R Core Team (2019). R: A language and environment for statistical computing. R Foundation for Statistical Computing, Vienna, Austria. Available online at https://www.R-project.org/.

Record, S., Dahlin, K. M., Zarnetske, P. L., Read, Q. D., Malone, S. L., Gaddis, K. D., ... & Hestir, E. (2020). Remote Sensing of Geodiversity as a Link to Biodiversity. In *Remote Sensing of Plant Biodiversity* (pp. 225-253). Springer, Cham.

Reichstein, M., Bahn, M., Ciais, P., Frank, D., Mahecha, M. D., Seneviratne, S. I., ... & Papale, D. (2013). Climate extremes and the carbon cycle. Nature, 500(7462), 287-295.

Reinermann, S., Asam, S., & Kuenzer, C. (2020). Remote sensing of grassland production and management—A review. *Remote Sensing*, *12*(12), 1949.

Richardson, A. D., Duigan, S. P., & Berlyn, G. P. (2002). An evaluation of noninvasive methods to estimate foliar chlorophyll content. *New phytologist*, *153*(1), 185-194.

Rocchini, D. (2007). Effects of spatial and spectral resolution in estimating ecosystem α-diversity by satellite imagery. *Remote sensing of Environment*, *111*(4), 423-434.

Rocchini, D., Balkenhol, N., Carter, G. A., Foody, G. M., Gillespie, T. W., He, K. S., ... & Neteler, M. (2010). Remotely sensed spectral heterogeneity as a proxy of species diversity: recent advances and open challenges. *Ecological Informatics*, *5*(5), 318-329.

Rocchini, D., Boyd, D. S., Féret, J. B., Foody, G. M., He, K. S., Lausch, A., ... & Pettorelli, N. (2016). Satellite remote sensing to monitor species diversity: potential and pitfalls. *Remote Sensing in Ecology and Conservation*, *2*(1), 25-36.

Rocchini, D., Chiarucci, A., & Loiselle, S. A. (2004). Testing the spectral variation hypothesis by using satellite multispectral images. *Acta Oecologica*, *26*(2), 117-120.

Rocchini, D., He, K. S., & Zhang, J. (2009). Is spectral distance a proxy of beta diversity at different taxonomic ranks? A test using quantile regression. *Ecological Informatics*, *4*(4), 254-259.

Rocchini, D., Luque, S., Pettorelli, N., Bastin, L., Doktor, D., Faedi, N., ... & Nagendra, H. (2018). Measuring β-diversity by remote sensing: A challenge for biodiversity monitoring. *Methods in Ecology and Evolution*, *9*(8), 1787-1798.

Rocchini, D., Marcantonio, M., Da Re, D., Chirici, G., Galluzzi, M., Lenoir, J. et al. (2019). Time-lapsing biodiversity: An open source method for measuring diversity changes by remote sensing. *Remote Sensing of Environment*, *231*, 111192.

Roelofsen, H. D., van Bodegom, P. M., Kooistra, L., & Witte, J. P. M. (2014). Predicting leaf traits of herbaceous species from their spectral characteristics. *Ecology and evolution*, *4*(6), 706-719.

Roscher, C., Temperton, V. M., Scherer-Lorenzen, M., Schmitz, M., Schumacher, J., Schmid, B., ... & Schulze, E. D. (2005). Overyielding in experimental grassland communities–irrespective of species pool or spatial scale. *Ecology Letters*, *8*(4), 419-429.

Ross, J.K., (1981). The radiation regime and architecture of plant stands. W. Junk, The Hague, Netherlands, pp. 391.

Rossi, M., Niedrist, G., Asam, S., Tonon, G., Tomelleri, E., & Zebisch, M. (2019). A comparison of the signal from diverse optical sensors for monitoring alpine grassland dynamics. *Remote Sensing*, *11*(3), 296.

Rouse, J. W., Haas, R. H., Schell, J. A., & Deering, D. W. (1974). Monitoring vegetation systems in the Great Plains with ERTS. *NASA special publication*, *351*(1974), 309.

Sakowska, K., Gianelle, D., Zaldei, A., MacArthur, A., Carotenuto, F., Miglietta, F., ... & Vescovo, L. (2015). WhiteRef: A new tower-based hyperspectral system for continuous reflectance measurements. *Sensors*, *15*(1), 1088-1105.

Sakowska, K., Juszczak, R., & Gianelle, D. (2016). Remote sensing of grassland biophysical parameters in the context of the Sentinel-2 satellite mission. *Journal of Sensors*, *2016*.

Sakowska, K., MacArthur, A., Gianelle, D., Dalponte, M., Alberti, G., Gioli, B., ... & Vescovo, L. (2019). Assessing across-scale optical diversity and productivity relationships in grasslands of the Italian Alps. *Remote Sensing*, *11*(6), 614.

Schäfer, E., Heiskanen, J., Heikinheimo, V., & Pellikka, P. (2016). Mapping tree species diversity of a tropical montane forest by unsupervised clustering of airborne imaging spectroscopy data. *Ecological indicators*, *64*, 49-58.

Schlerf, M., & Atzberger, C. (2006). Inversion of a forest reflectance model to estimate structural canopy variables from hyperspectral remote sensing data. *Remote sensing of environment*, *100*(3), 281-294.

Schmidtlein, S., & Fassnacht, F. E. (2017). The spectral variability hypothesis does not hold across landscapes. *Remote sensing of environment*, *192*, 114-125.

Schrodt, F., de la Barreda Bautista, B., Williams, C., Boyd, D. S., Schaepman-Strub, G., & Santos, M. J. (2020). Integrating biodiversity, remote sensing, and auxiliary information for the study of ecosystem functioning and conservation at large spatial scales. In *Remote sensing of plant biodiversity* (pp. 449-484). Springer, Cham.

Schweiger, A. K. (2020). Spectral field campaigns: Planning and data collection. In *Remote Sensing of Plant Biodiversity* (pp. 385-423). Springer, Cham.

Schweiger, A. K., Cavender-Bares, J., Townsend, P. A., Hobbie, S. E., Madritch, M. D., Wang, R., ... & Gamon, J. A. (2018). Plant spectral diversity integrates functional and phylogenetic components of biodiversity and predicts ecosystem function. *Nature Ecology & Evolution*, *2*(6), 976-982.

Schweiger, A. K., Schütz, M., Risch, A. C., Kneubühler, M., Haller, R., & Schaepman, M. E. (2017). How to predict plant functional types using imaging spectroscopy: linking vegetation community traits, plant functional types and spectral response. *Methods in Ecology and Evolution*, *8*(1), 86-95.

Serbin, S. P., & Townsend, P. A. (2020). Scaling functional traits from leaves to canopies. In *Remote Sensing of Plant Biodiversity* (pp. 43-82). Springer, Cham.

Serrano, L., Gamon, J. A., & Peñuelas, J. (2000). Estimation of canopy photosynthetic and nonphotosynthetic components from spectral transmittance. *Ecology*, *81*(11), 3149-3162.

Shang, J., Liu, J., Ma, B., Zhao, T., Jiao, X., Geng, X., ... & Walters, D. (2015). Mapping spatial variability of crop growth conditions using RapidEye data in Northern Ontario, Canada. *Remote Sensing of Environment*, *168*, 113-125.

Shannon, C. E. (1948). A mathematical theory of communication. *The Bell system technical journal*, *27*(3), 379-423.

Simpson, E. H. (1949). Measurement of diversity. *nature*, *163*(4148), 688-688.

Sims, D. A., & Gamon, J. A. (2003). Estimation of vegetation water content and photosynthetic tissue area from spectral reflectance: a comparison of indices based on liquid water and chlorophyll absorption features. *Remote sensing of environment*, *84*(4), 526-537.

Sorensen, T. A. (1948). A method of establishing groups of equal amplitude in plant sociology based on similarity of species content and its application to analyses of the vegetation on Danish commons. *Biol. Skar.*, *5*, 1-34.

Stevens, C. J. (2018). Recent advances in understanding grasslands. *F1000Research*, *7*.

Torresani, M., Feilhauer, H., Rocchini, D., Féret, J. B., Zebisch, M., & Tonon, G. (2021). Which optical traits enable an estimation of tree species diversity based on the Spectral Variation Hypothesis?. *Applied Vegetation Science*, *24*(2), e12586.

Torresani, M., Rocchini, D., Sonnenschein, R., Zebisch, M., Marcantonio, M., Ricotta, C., & Tonon, G. (2019). Estimating tree species diversity from space in an alpine conifer forest: The Rao's Q diversity index meets the spectral variation hypothesis. *Ecological Informatics*, *52*, 26-34.

Ustin, S. L. (2004). Remote sensing of environment: State of the science and new directions. *Remote Sensing of Natural Resources Management and Environmental Monitoring*, 679-729.

Ustin, S. L., & Jacquemoud, S. (2020). How the optical properties of leaves modify the absorption and scattering of energy and enhance leaf functionality. In *Remote sensing of plant biodiversity* (pp. 349-384). Springer, Cham.

Verrelst, J., Rivera, J. P., van der Tol, C., Magnani, F., Mohammed, G., & Moreno, J. (2015a). Global sensitivity analysis of the SCOPE model: What drives simulated canopy-leaving sun-induced fluorescence?. *Remote Sensing of Environment*, *166*, 8-21.

Verrelst, J., Rivera, J. P., Veroustraete, F., Muñoz-Marí, J., Clevers, J. G., Camps-Valls, G., & Moreno, J. (2015b). Experimental Sentinel-2 LAI estimation using parametric, non-parametric and physical retrieval methods–A comparison. *ISPRS Journal of Photogrammetry and Remote Sensing*, *108*, 260-272.

Verrelst, J., Malenovský, Z., Van der Tol, C., Camps-Valls, G., Gastellu-Etchegorry, J. P., Lewis, P., ... & Moreno, J. (2019). Quantifying vegetation biophysical variables from imaging spectroscopy data: a review on retrieval methods. *Surveys in Geophysics*, *40*(3), 589-629.

Verrelst, J., Sabater, N., Rivera, J. P., Muñoz-Marí, J., Vicent, J., Camps-Valls, G., & Moreno, J. (2016). Emulation of leaf, canopy and atmosphere radiative transfer models for fast global sensitivity analysis. *Remote Sensing*, *8*(8), 673.

Vescovo, L., & Gianelle, D. (2008). Using the MIR bands in vegetation indices for the estimation of grassland biophysical parameters from satellite remote sensing in the Alps region of Trentino (Italy). *Advances in Space Research*, *41*(11), 1764-1772.

Vescovo, L., Wohlfahrt, G., Balzarolo, M., Pilloni, S., Sottocornola, M., Rodeghiero, M., & Gianelle, D. (2012). New spectral vegetation indices based on the near-infrared shoulder wavelengths for remote detection of grassland phytomass. *International journal of remote sensing*, *33*(7), 2178-2195.

Ollinger, S. V. (2011). Sources of variability in canopy reflectance and the convergent properties of plants. *New Phytologist*, *189*(2), 375-394.

Viña, A., & Gitelson, A. A. (2005). New developments in the remote estimation of the fraction of absorbed photosynthetically active radiation in crops. *Geophysical Research Letters*, *32*(17).

Vrieling, A., Meroni, M., Darvishzadeh, R., Skidmore, A. K., Wang, T., Zurita-Milla, R., ... & Paganini, M. (2018). Vegetation phenology from Sentinel-2 and field cameras for a Dutch barrier island. *Remote Sensing of Environment*, *215*, 517-529.

Wang, B., An, R., Jiang, T., Xing, F., & Ju, F. (2020). Image Spectral Resolution Enhancement for Mapping Native Plant Species in a Typical Area of the Three-River Headwaters Region, China. *Remote Sensing*, *12*(19), 3146.

Wang, R., & Gamon, J. A. (2019). Remote sensing of terrestrial plant biodiversity. *Remote Sensing of Environment*, *231*, 111218.

Wang, R., Gamon, J. A., Cavender-Bares, J., Townsend, P. A., & Zygielbaum, A. I. (2018a). The spatial sensitivity of the spectral diversity–biodiversity relationship: an experimental test in a prairie grassland. *Ecological Applications*, *28*(2), 541-556.

Wang, R., Gamon, J. A., Schweiger, A. K., Cavender-Bares, J., Townsend, P. A., Zygielbaum, A. I., & Kothari, S. (2018b). Influence of species richness, evenness, and composition on optical diversity: A simulation study. *Remote Sensing of Environment*, *211*, 218-228.

Wang, R., Gamon, J. A., Emmerton, C. A., Li, H., Nestola, E., Pastorello, G. Z., & Menzer, O. (2016). Integrated analysis of productivity and biodiversity in a southern Alberta prairie. *Remote Sensing*, *8*(3), 214.

Wen-long, B., Qing-wei, Y., Ya-jun, C., Lu, Z., Wei, L., Hui-min, L., & Yong-qing, Y. (2013). Effects of Drought Stress on Photosynthetic Characteristics of Kentucky Bluegrass. *Journal of Northeast Agricultural University (English Edition)*, *20*(2), 19-23.

Whittaker, R. H. (1960). Vegetation of the Siskiyou mountains, Oregon and California. *Ecological monographs*, *30*(3), 279-338.

Wickham, H. (2007). Reshaping data with the reshape package. *Journal of statistical software*, *21*(12), 1-20.

Widlowski, J. L., Pinty, B., Gobron, N., Verstraete, M. M., Diner, D. J., & Davis, A. B. (2004). Canopy structure parameters derived from multi-angular remote sensing data for terrestrial carbon studies. *Climatic Change*, *67*(2), 403-415.

Wilson, J. B. (1988). Shoot competition and root competition. *Journal of applied ecology*, 279-296.

Wilson, M. V., & Shmida, A. (1984). Measuring beta diversity with presence-absence data. *The Journal of Ecology*, 1055-1064.

Wohlfahrt, G., Hammerle, A., Haslwanter, A., Bahn, M., Tappeiner, U., & Cernusca, A. (2008). Seasonal and inter-annual variability of the net ecosystem CO2 exchange of a temperate mountain grassland: Effects of weather and management. *Journal of Geophysical Research: Atmospheres*, *113*(D8) 1–14.

Wohlfahrt, G., Sapinsky, S., Tappeiner, U., & Cernusca, A. (2001). Estimation of plant area index of grasslands from measurements of canopy radiation profiles. *Agricultural and Forest Meteorology*, *109*(1), 1-12.

Xie, Q., Dash, J., Huang, W., Peng, D., Qin, Q., Mortimer, H., ... & Ye, H. (2018). Vegetation indices combining the red and red-edge spectral information for leaf area index retrieval. *IEEE Journal of selected topics in applied earth observations and remote sensing*, *11*(5), 1482-1493.

Zarco-Tejada, P. J., Hornero, A., Hernández-Clemente, R., & Beck, P. S. A. (2018). Understanding the temporal dimension of the red-edge spectral region for forest decline detection using high-resolution hyperspectral and Sentinel-2a imagery. *ISPRS Journal of Photogrammetry and Remote Sensing*, *137*, 134-148.

Zarco-Tejada, P. J., Miller, J. R., Noland, T. L., Mohammed, G. H., & Sampson, P. H. (2001). Scaling-up and model inversion methods with narrowband optical indices for chlorophyll content estimation in closed forest canopies with hyperspectral data. *IEEE Transactions on Geoscience and Remote Sensing*, *39*(7), 1491-1507.

Zhang, X., Jiao, Z., Dong, Y., Zhang, H., Li, Y., He, D., ... & Chang, Y. (2018). Potential investigation of linking PROSAIL with the Ross-Li BRDF model for vegetation characterization. *Remote Sensing*, *10*(3), 437.

Zhao, X., Zhou, D., & Fang, J. (2012). Satellite-based Studies on Large-Scale Vegetation Changes in China F. *Journal of integrative plant biology*, *54*(10), 713-728.

Zhao, Y., Sun, Y., Chen, W., Zhao, Y., Liu, X., & Bai, Y. (2021). The Potential of Mapping Grassland Plant Diversity with the Links among Spectral Diversity, Functional Trait Diversity, and Species Diversity. *Remote Sensing*, *13*(15), 3034.

Zhao, Y., Zeng, Y., Zhao, D., Wu, B., & Zhao, Q. (2016). The optimal leaf biochemical selection for mapping species diversity based on imaging spectroscopy. *Remote Sensing*, *8*(3), 216.

Zhen, S., & van Iersel, M. W. (2017). Photochemical acclimation of three contrasting species to different light levels: Implications for optimizing supplemental lighting. *Journal of the American Society for Horticultural Science*, *142*(5), 346-354.

Zou, X., & Mõttus, M. (2017). Sensitivity of common vegetation indices to the canopy structure of field crops. *Remote Sensing*, *9*(10), 994.